Design of a Cross-over Diffuser for a Mixed Flow Compressor Impeller

by

Macaera Preston Kock

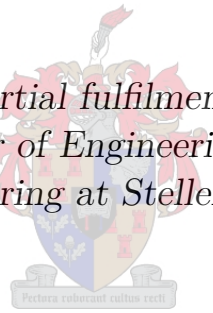

Thesis presented in partial fulfilment of the requirements for the degree of Master of Engineering (Mechanical) in the Faculty of Engineering at Stellenbosch University

Supervisor: Prof. S J. van der Spuy
Co-supervisor: Prof. T W. Von Backström

March 2017

Declaration

By submitting this thesis electronically, I declare that the entirety of the work contained therein is my own, original work, that I am the sole author thereof (save to the extent explicitly otherwise stated), that reproduction and publication thereof by Stellenbosch University will not infringe any third party rights and that I have not previously in its entirety or in part submitted it for obtaining any qualification.

Date: March 2017

Abstract

Design of a Cross-over Diffuser for a Mixed Flow Compressor Impeller

M.P. Kock

Department of Mechanical and Mechatronic Engineering,
University of Stellenbosch,
Private Bag X1, Matieland 7602, South Africa.

Thesis: MEng (Mech)

March 2017

This research project focused on the design of a cross-over diffuser for a mixed flow compressor employed in a 600 N thrust micro gas turbine (MGT). Due to the exit of a mixed flow impeller having a meridional discharge angle $\alpha_{2a} < 90°$, the use of a conventional radial diffuser is inappropriate. The cross over diffuser is a single row diffuser that replaces the conventional two row radial to de-swirler diffuser. The cross-over diffuser is suitable for a mixed flow impeller due to its ability to capture the flow from the impeller without inducing flow separation on the meridional passage walls. The initial cross-over diffuser used in this research was designed using a mean line code. A multi-point optimisation of the mean line design was performed using NUMECA Design3D$^{\text{TM}}$, by means of an Artificial Neural Network incorporated into a Genetic Algorithm. The optimised design showed an increase of 8.75% for the compressor stage total-to-total isentropic efficiency, and a 7.7% increase in total-to-total pressure ratio. The optimised diffuser yielded a large increase in static pressure recovery coefficient of 28.33%. The optimised diffuser static-to-static pressure ratio was increased by 21.5%. The overall operating range remained constant, but the choke mass flow rate increased. The stall mass flow rate also increased, thus shifting the operating range up to a higher mass flow rate. An investigation was also done to evaluate the feasibility of vaneless diffusers by using the same passage of the optimised diffuser in a vaneless format. De-swirlers were also added to the vaneless diffuser. The optimised vaned diffuser outperforms the vaneless diffuser but lacks in operating range.

Uittreksel

Ontwerp van 'n Oorgangsdiffusor vir 'n Gemengde Vloei Kompressor Rotor

("Design of a Cross-over Diffuser for a Mixed Flow Compressor Impeller")

M.P. Kock

Departement Meganiese en Megatroniese Ingenieurswese,
Universiteit van Stellenbosch,
Privaatsak X1, Matieland 7602, Suid Afrika.

Tesis: MIng (Meg)

Maart 2017

Hierdie navorsingsprojek fokus op die ontwerp van 'n oorgangsdiffusor vir 'n gemengde vloei kompressor wat toegepas gaan word in 'n 600 N stukrag mikro gas turbine (MGT). Die gemengde-vloei kompressor het 'n nie-radiale meridionale uitlaat vloeihoek $\alpha_{2a} < 90°$, en as gevolg hiervan is die gebruik van konvensionele radiale diffusors nie 'n toepaslike keuse nie. Die oorgangsdiffusor is 'n enkelry diffusor wat die konvensionele twee-ry radiaal-na-aksiale vloeirigter diffusor vervang. Die oorgangsdiffusor is toepaslik vir 'n gemengde vloei kompressor omdat dit die vermoë het om vloei te rig sonder om wegbreking in die meridionale vloei kanaal te veroorsaak. Die aanvanlike oorgangsdiffusor is ontwerp met 'n een-dimensionele kode. 'n Multi-punt optimering is op die een-dimensionele ontwerp toegepas. Die optimerings proses was gedoen met NUMECA Design3D$^{\text{TM}}$ sagteware. 'n Kunsmatige neurale netwerk, wat 'n Genetiese algoritme inkorporeer is gebruik om die optimering te voltooi. Die geoptimeerde ontwerp toon 'n toename van 8.75% vir die kompressor totale-tot-totale insentropiese benuttingsgraad en 'n 7.7% toename in totale-tot-totale drukverhouding. Die geoptimeerde diffusorontwerp het 'n groot verbetering in statiese drukherwinnings koëffisiënt toename van 28.33% voorspel. Die geoptimeerde ontwerp se staties-tot-statiese drukverhouding het ook met 21.5% toegeneem. Die algehele werks bestek van die kompressor het konstant gebly, maar die smoor en staak massavloeitempo het toegeneem, wat beteken dat die bestek opgeskuif het na 'n hoër massavloei. 'n Studie is gedoen om die lewensvatbaarheid van lemlose diffusors te ondersoek deur gebruik te maak van die geomptimeerde diffusor kanaal in 'n lemlose formaat. Aksiale vloeirigters is

ook toegevoeg by die lemlose diffusor en gesimuleer. Die geoptimeerde ontwerp toon beter prestasie as die lemlose diffusor , maar met 'n kleiner bestek.

Acknowledgements

Firstly I would like to thank my supervisor Prof. van der Spuy for his support and guidance. I would also like to thank him for making it possible to obtain funding for this research.

I would also like to thank my co-supervisor Prof. von Backtröm for his guidance and insightful comments.

I give thanks to the NUMECA support staff for the continued support during the process. I would also like to thank Charl Möller for assisting me with software issues that was beyond what he was supposed to do.

Thank you to the CSIR and ARMSCOR for making funding available to complete this project.

Lastly I would like to thank my friends and family for their continued support and love.

Contents

Declaration i

Abstract ii

Uittreksel iii

Acknowledgements v

Contents vi

List of Figures x

List of Tables xiii

Nomenclature xv

1 Introduction 1
- 1.1 Background and motivation . . . 1
- 1.2 Project objectives and methodology . . . 3
- 1.3 Outline . . . 4

2 Literature study 5
- 2.1 Introduction . . . 5
- 2.2 Conventional compressors for MGTs . . . 5
  - 2.2.1 Centrifugal compressors . . . 6
  - 2.2.2 Mixed flow compressor . . . 7
  - 2.2.3 Compressor instabilities . . . 7
- 2.3 Compressor theory . . . 10
  - 2.3.1 Impeller theory . . . 10
  - 2.3.2 Diffuser theory . . . 13
  - 2.3.3 Pressure ratio and efficiency . . . 14
- 2.4 Diffuser geometric parameters . . . 15
  - 2.4.1 Vaneless diffuser . . . 15
  - 2.4.2 Vaned radial diffuser theory . . . 18
  - 2.4.3 De-swirlers . . . 22

2.4.4 Continuous diffuser vanes . . . 23
2.4.5 Diffuser impeller interaction . . . 23

3 Diffuser mean line design 26
3.1 Introduction . . . 26
3.2 Mean line code . . . 26
3.2.1 Input . . . 27
3.2.2 Main code . . . 27
3.2.3 Output . . . 30
3.3 Vaned crossover diffuser design . . . 30
3.3.1 Performance and size specifications . . . 31
3.3.2 Vaneless crossover diffuser . . . 31
3.3.3 Vaned diffuser design . . . 33
3.4 Closing remarks . . . 37

4 Numerical analysis 38
4.1 Introduction . . . 38
4.2 Meshing strategy-AutoGrid5™ . . . 38
4.2.1 Meridional mesh setup . . . 39
4.2.2 Blade-to-blade mesh setup . . . 40
4.2.3 3-D mesh setup . . . 42
4.2.4 Mesh quality and mesh independence . . . 43
4.3 Fine™/Turbo simulation setup . . . 45
4.3.1 Fluid flow model . . . 45
4.3.2 Boundary conditions . . . 48
4.3.3 Computational setup . . . 50
4.3.4 Closing remarks . . . 51

5 Optimisation 52
5.1 Introduction . . . 52
5.2 Parametric model . . . 53
5.2.1 Meridional contours 'End walls' . . . 53
5.2.2 Stream surfaces . . . 54
5.2.3 Stacking laws . . . 54
5.2.4 Main blade . . . 55
5.2.5 Fitting control . . . 55
5.3 Parameter bounds . . . 56
5.4 Database generation . . . 58
5.4.1 Parametric model and mesh generation . . . 58
5.4.2 Numerical model . . . 59
5.4.3 Post processing . . . 59
5.5 Optimisation . . . 60
5.5.1 Artificial neural network . . . 60
5.5.2 Genetic algorithm . . . 61

5.5.3 Objective function 62
5.6 Optimised design 63
5.7 Closing remark 67

6 Results discussion **68**
6.1 Introduction 68
6.2 Mean line results 68
6.3 Optimised design 70
6.4 Vaneless diffuser performance 71
6.4.1 Vaneless diffuser 72
6.4.2 Vaneless diffuser with de-swirlers 73
6.5 Diffuser results summary 75
6.6 Manufacturing 76
6.7 Closing remarks 76

7 Conclusion and recommendation **78**
7.1 Design summary 78
7.2 Conclusion 80
7.3 Recommendations 80

Appendices **81**

A Mean line blade surface construction **82**

B *.geomTurbo* file format **84**

C 1-D performance calculations scheme **88**
C.1 Vaneless performance 88
C.2 Vaned performance 89
C.2.1 Inlet losses 89
C.2.2 Passage and blade losses 90

D Impeller passage **93**

E Additional mesh details **94**
E.1 Mesh independence 94
E.1.1 Fine mesh 94
E.1.2 Coarse mesh 95
E.2 Optimised design mesh 96
E.3 Blade inlet/outlet type topology 97

F Parametrisation **98**

G Possible database geometries **101**

H Performance maps **102**

H.1 Vaneless mean line performance 102
H.2 Optimised design first leading edge 103

I Final compressor performance map **105**

J Vaneless diffuser with de-swirler vanes geometry **106**

K Manufactured parts **107**

List of References **108**

List of Figures

1.1 BMT 120 KS micro gas turbine layout (van der Merwe, 2012) . . 2

2.1 Centrifugal compressor r-z plane (Krige, 2012) 6
2.2 Mixed flow impeller meridional view (Kano *et al.*, 1984) 7
2.3 Blade stall (dynamic stall) (Dixon, 1978) 9
2.4 Compressor characteristic curve (van der Merwe, 2012) 10
2.5 Impeller velocity triangles adapted from van der Merwe (2012) . . 11
2.6 Mollier chart for centrifugal compressor 12
2.7 Diffuser velocity components 14
2.8 2-D Diffuser 16
2.9 Flow regime in channel diffuser (Japikse and Baines, 1997) 17
2.10 Vaned radial diffuser Krige (2012) 18
2.11 Vaneless gap (Gaetani *et al.*, 2012) 25

3.1 Mean line code overview (Burger, 2016) 27
3.2 Bezier curve (Burger, 2016) 28
3.3 Meridional a) Blade angle and b) Camberline-angle definitions (Burger, 2016) 29
3.4 Mean line design process 30
3.5 a) Impeller total-to-total pressure ratio b) Impeller total-to-total isentropic efficiency 32
3.6 Vector plot and mid meridional contour 35
3.7 Meridional Streamlines 35
3.8 a) Compressor total-to-total pressure ratio b) Compressor total-to-total isentropic efficiency 36
3.9 a) Diffuser static-to-static pressure ratio b) Diffuser static pressure recovery coefficient 36

4.1 Meridional mesh view (flow path) 39
4.2 Impeller blade-to-blade grid points 40
4.3 Blade-to-blade matching (NUMECA International, 2014a) 41
4.4 Diffuser blade-to-blade grid points 41
4.5 Blade-to-blade clustering diffuser 42
4.6 Compressor 3-D Mesh 43

4.7 3-D y^+ values for MLDD a) Refined mesh b) Original unrefined mesh 44
4.8 a) Compressor total-to-total pressure ratio b) Compressor total-to-total isentropic efficiency 44
4.9 a) Compressor total-to-total pressure ratio b) Compressor total-to-total isentropic efficiency 45
4.10 a) Compressor total-to-total pressure ratio b) Compressor total-to-total isentropic efficiency 48
4.11 Computational domain 49
4.12 Mass flow convergence 51

5.1 Optimisation process 52
5.2 Three point optimisation 53
5.3 Meridional view parametrisation 54
5.4 Diffuser vane parametrisation 55
5.5 Unacceptable geometries 56
5.6 Optimisation convergence 63
5.7 Meridional geometry with vane leading and trailing edges 64
5.8 a) Hub vane profile b) Shroud vane profile 64
5.9 a) Mean line design b) LE normal to flow c) LE parallel to impeller TE 65
5.10 a) Mean line design b) Optimised design 65
5.11 a) Compressor total-to-total pressure ratio b) Compressor total-to-total isentropic efficiency 66
5.12 a) Diffuser static-to-static pressure ratio b) Diffuser static pressure recovery coefficient 66

6.1 a) Diffuser static-to-static pressure ratio b) Diffuser static pressure recovery coefficient 69
6.2 Static pressure propagation 70
6.3 a) Diffuser static-to-static pressure ratio b) Diffuser static pressure recovery coefficient 70
6.4 a) Compressor static pressure contour with MLDD b) Compressor static pressure contour with ODD 71
6.5 a) Compressor total-to-total pressure ratio b) Compressor total-to-total isentropic efficiency 72
6.6 a) Diffuser static-to-static pressure ratio b) Diffuser static pressure recovery coefficient 72
6.7 a) Compressor total-to-total pressure ratio b) Compressor total-to-total isentropic efficiency 73
6.8 a) Diffuser static-to-static pressure ratio b) Diffuser static pressure recovery coefficient 74
6.9 Recirculation bubble 74
6.10 a) Compressor total-to-total pressure ratio b) Compressor total-to-total isentropic efficiency 75

6.11 a) Diffuser static-to-static pressure ratio b) Diffuser static pressure recovery coefficient 75
6.12 3-D Compressor drawing 76

D.1 Meridional flow channel (Diener, 2016) 93

E.1 Diffuser blade-to-blade grid size 94
E.2 Impeller blade-to-blade grid size 94
E.3 Diffuser blade-to-blade grid size 95
E.4 Impeller blade-to-blade grid size 95
E.5 diffuser blade-to-blade grid size 96
E.6 Impeller blade-to-blade grid size 96
E.7 Blade inlet and outlet topology types NUMECA International (2014a) 97

G.1 Sample possible blade geometries 101
G.2 Sample possible meridional geometries 101

H.1 a) Compressor total-to-total pressure ratio b) Compressor total-to-total isentropic efficiency 102
H.2 a) Diffuser static-to-static pressure ratio b) Diffuser static pressure recovery coefficient 103
H.3 a) Compressor total-to-total pressure ratio b) Compressor total-to-total isentropic efficiency 103
H.4 a) Diffuser static-to-static pressure ratio b) Diffuser static pressure recovery coefficient 104

I.1 Compressor map total-to-total pressure ratio 105
I.2 Compressor map total-total isentropic efficiency 105

J.1 Compressor with de-swirler geometry 106

K.1 Diffuser test model 107
K.2 Diffuser test rig 107

List of Tables

2.1 Design specifications 20

3.1 Specification summary 31
3.2 Input flow conditions 32
3.3 New inlet flow conditions 33
3.4 Constant design parameters 33
3.5 Final design parameters 34
3.6 Parameters at design point 37

4.1 Mesh quality final of MLDD 43
4.2 Fluid model type at design point 46
4.3 Fluid properties 46
4.4 Inlet conditions for SST turbulence model 47
4.5 Inlet conditions for $k - \epsilon$ turbulence model 48
4.6 Inlet boundary conditions 49
4.7 Impeller hub boundary conditions 50
4.8 Solid boundary conditions 50

5.1 Free parameter list 57
5.2 Dependant parameter list 58
5.3 Mesh quality database 59
5.4 ANN parameter settings 61
5.5 GA parameter settings 62
5.6 Imposed quantities for the objective function 63
5.7 Optimised design point with two different leading edges 65
5.8 Design point results 67

6.1 Parameters at design point 68
6.2 Design point results 71
6.3 Results summary at design point 76

C.1 Inlet flow conditions 89

E.1 Mesh quality final design 95
E.2 Mesh quality final design 96

E.3 Mesh quality optimised design 97

F.1 Frozen parameter impeller passage 99
F.2 Frozen parameter list 100

Nomenclature

Constants

g = $9.81\,\mathrm{m/s^2}$

Variables

A	Passage area	$[\mathrm{m^2}]$
b	Hub-to-shroud passage width	$[\mathrm{m}]$
C	Absolute velocity	$[\mathrm{m/s^2}]$
cp	Specific heat	$[\mathrm{J/kg{\cdot}K}]$
C_P	Static pressure recovery coeficient	$[-]$
h	Enthalpy	$[\mathrm{kJ/kg}]$
i	Incidence angle	$[\,^{\mathrm{o}}]$
K	Blade curvature parameter	$[-]$
L	Blade loading parameter	$[-]$
L	Blade length	$[\mathrm{m}]$
$\dot{m}$	Mass flow rate	$[\mathrm{kg/s}]$
m	Meridional co-ordinate	$[\mathrm{m}]$
Ma	Mach number	$[-]$
p	Pressure	$[\mathrm{Pa}]$
PR	Pressure ratio	$[-]$
R	Radius ratio (r_4/r_3)	$[-]$
r	Radius	$[\mathrm{m}]$
s	Entropy	$[\mathrm{J/kg{\cdot}K}]$
S_N	Swirl	$[-]$
T	Temperature	$[\mathrm{K}]$
t	Vane thickness	$[\mathrm{m}]$
t_{max}	Maximum vane thickness	$[\mathrm{m}]$
W	Relative velocity	$[\mathrm{m}]$
$\dot{W}$	Work done	$[\mathrm{W}]$
Z	Number of vanes	$[-]$

Z	Number of vanes	$[-]$
z	Axial component	$[\mathrm{m}]$
θ	Divergence angle	$[\ ^{\mathrm{o}}]$
U	Blade velocity	$[\mathrm{m/s^2}]$
α_a	Meridional passage flow angle	$[\ ^{\mathrm{o}}]$
α_c	Flow angle	$[\ ^{\mathrm{o}}]$
β	Blade angle	$[\ ^{\mathrm{o}}]$
γ	Specific heat ratio	$[-]$
η	Efficiency	$[-]$
ω	Rotional speed	$[\mathrm{rpm}]$
τ	Torque	$[\mathrm{N{\cdot}m}]$
ρ	Density	$[\mathrm{kg/m^3}]$

Subscripts

B	Blade conditions
0	Total thermodynamic condition
comp	Compressor imposed value
t	Total thermodynamic condition
o	Static thermodynamic condition
r	Radial component
VD	Vaned diffuser conditions
θ	Tangential component
th	Diffuser throat
0	Compressor inlet
1	Impeller inlet
2	Impeller outlet
3	Diffuser inlet
4	Diffuser outlet

Acronyms

1-D	One dimensional
2-D	Two dimensional
3-D	Three dimensional
ANN	Artificial neural network
ARMSCOR	Armaments Corporation of South Africa
BMT120KS	Baird Micro Turbine 120 Kero Start
CAD	Computer aided design

CD Cross-over diffuser
CNC Computer numerical control
CFD Computational Fluid Dynamics
CSIR Council for Scientific and industrial Research
DG Diener geometry
GA Genetic algorithm
LE Leading edge
MGT Micro gas turbine
MLC Mean line code
MLDD Mean line diffuser design
NACA National Advisory Committee for Aeronautics
ODD Optimised diffuser design
SM Stall margin
TE Trailing edge
UAV Unmanned aerial vehicle
VLD Vaneless diffuser
VLDD Vaneless diffuser with de-swirler vanes

Chapter 1

Introduction

1.1 Background and motivation

There is currently a strong focus on the local development of micro gas turbine (MGT) propulsion systems for use in unmanned aerial vehicles (UAVs) in South Africa. UAVs have various purposes, that include aerial combat, national security, crime fighting, disaster management, election monitoring and search-and-rescue operations (de Villiers, 2014). The two most common types of propulsion systems used by UAVs are propellers, and the aforementioned MGT engines. Although MGTs can generate high speeds they are more complex than conventional propeller systems. However MGT propulsion systems are preferred for use in UAVs because of their compactness and high thrust-to-weight ratio. The Skua target drone is currently being distributed by Denel Dynamics and uses MGT propulsion. Turbojet engines were initially developed for energy generating purposes utilizing the shaft output power (turbo-shaft) to generate electricity. Attention progressed to the development of a turbojet engine aircraft propulsion (Krige, 2012).

This research forms part of the CONVERGE II program which is an initiative that was established by the South African Air Force through ARMSCOR and the Centre for Scientific and Industrial Research (CSIR). The main purpose of the CONVERGE II project is to further the level of knowledge on the design and development of propulsive turbomachinery in South Africa. Stellenbosch University has completed a number of research projects for this initiative, all revolving around the development of MGTs. Figure 1.1 shows a layout of such a MGT, where all the major components are shown. The majority of the projects focused on a 200 N upgrade of the existing BMT 120KS engine. Recently the focus has however shifted towards the development of a 600 N engine.

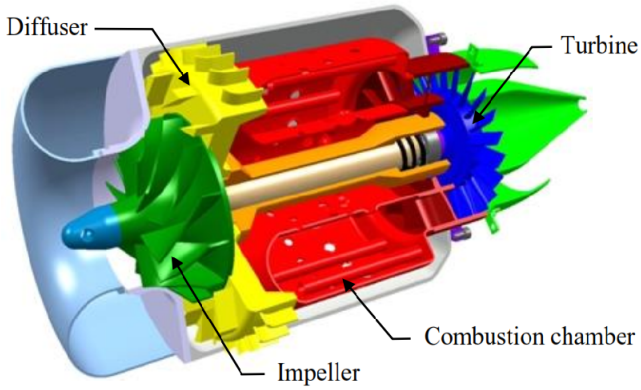

Figure 1.1: BMT 120 KS micro gas turbine layout (van der Merwe, 2012)

The scope of this project is based on the 600 N thrust MGT engine proposed by the CSIR. The new engine will be approximately twice the length and diameter of the BMT 120 KS engine. The compressor will consist of a mixed flow impeller developed by Diener (2016). The primary role of this thesis is to design the diffuser for the compressor stage that would match the mixed flow impeller previously developed by Diener (2016). The design method used will be similar to that used by Burger (2016). A summary of the research projects that have been completed and are still being pursued for both the 200 N and 600 N engines is as follows:

Development of a centrifugal compressor impeller

Van der Merwe (2012) developed an impeller for the 200 N engine with the use of a 1-D mean line code developed by de Wet (2012). The impeller geometry was optimized using Computational Fluid Dynamics (CFD) optimization with the help of Numeca Fine/Turbo^{TM}, AutoGrid5^{TM} and Design3D^{TM}. Van der Merwe's objectives were to design an impeller that a has PR_{t-t} of 4.72, and a η_{t-t} of 79.8%, operating at 121 000 rpm and a flow rate of 0.325 kg/s.

Development of centrifugal compressor diffuser

Krige (2012) redesigned the diffuser of the BMT 120 KS engine. This was done to obtain better efficiencies and static pressure recovery across the compressor stage at a high mass flow rate. Krige used CompAero^{TM} and NUMECA Fine/Turbo^{TM} software to design the vaned diffuser.

Development of a centrifugal diffuser and impeller

De Villiers (2014) designed a complete compressor stage for the 200 N thrust engine. This includes the impeller and the radial diffuser. De Villiers (2014) used the MLC developed by van der Merwe (2012) to design the impeller and

used NUMECA Design3D™ to optimise the impeller and diffuser simultaneously. The initial diffuser design was done with an adapted 1-D code based on the work of Aungier (2000).

Development of a cross-over diffuser

The aim of Burger's (2016) project was to develop a single vane diffuser for the 200 N thrust engine. The diffuser replaced the conventional radial diffuser and axial de-swirlers with one continuous vane (called a cross-over diffuser). The primary motivation for this design was to eliminate the vaneless bend and minimise recirculation that exist in the vaneless bend. Burger used and adapted the 1-D code developed by van der Merwe (2012) to perform the initial design of the cross-over diffuser. The cross-over design was then optimised with CFD optimisation software NUMECA Design3D™.

Development of a mixed flow impeller

The primary objective of Diener's (2016) research was to develop a mixed flow impeller for a 600 N thrust MGT engine. Diener (2016) used an adapted 1-D code based on the work of Aungier (2000), and CFTurbo™ software to design the initial Geometry and used NUMECA's coupled fluid-structure optimization code to optimise the design.

1.2 Project objectives and methodology

The primary objective of this research project is to design a diffuser for a mixed flow compressor impeller. The research will investigate the diffuser-impeller interaction and the vaneless space between the diffuser and impeller. The diffuser design will be done with the use of a 1-D MLC developed and adapted by Burger (2016). The 1-D MLC will be used to generate the geometry that is required for the 3-D CFD simulation and optimization. NUMECA Fine™/Turbo, AutoGrid5™ and Design3D™ will be used to optimize and simulate the 1-D mean line design.

The main objective of a diffuser is to achieve a static pressure recovery that will aid the combustion process in the combustion chamber. However, based on Diener (2016) the compressor stage must still attain a $PR_{t-t(0-4)}$ of greater or equal to 3.83 at a $\eta_{t-t(0-4)}$ of not less than 85%.

The methodology followed in this project is as follows:

- Adapt the 1-D MLC developed by Burger (2016) to generate the mean lined cross-over diffuser design.

- Simulate the design using NUMECA Fine/Turbo™, and generate the characteristics of the mean line diffuser.
- Optimise the design with the use of AutoGrid5™ and Design3D™.
- Explore vaneless, and de-swirler diffuser designs.
- Manufacture the optimised design for the diffuser in addition to the impeller designed by Diener (2016) with the use of 5 axis milling machine.
- The results will then be evaluated and a conclusions will be made.

1.3 Outline

The thesis outline is as follows; first a literature study on the radial and cross-over will be detailed in Chapter 2. This literature study will include the theory of the diffuser and the impeller but will focus primarily on the diffuser. The third chapter will discuss the mean line design and the code that was used. The fourth chapter will describe the CFD that was performed to simulate the compressor stage. The fifth chapter will document the optimization procedure that was followed to obtain the optimum diffuser design. The sixth chapter will discuss results and other geometry types that can be fitted to the compressor. The seventh and final chapter will conclude and provide recommendations on further research that can be done to take this research further.

Chapter 2

Literature study

2.1 Introduction

The literature that forms the background for this study focusses on the compressor section of the Micro Gas Turbine (MGT). Compressor types commonly associated with MGTs are mixed flow and centrifugal compressors. These compressors typically consist of two components namely, the impeller and the diffuser. This chapter will cover the operating principles of the compressor stage components.

2.2 Conventional compressors for MGTs

Centrifugal and mixed flow compressors are the two conventional types of compressors employed in MGTs. The principal reason for using these types of compressors rather than axial compressors is that the centrifugal and mixed flow compressors are more suitable for small volume flow rates, due to their shorter axial size. It is also less susceptible to performance losses due to fouling that can occur on the impeller blades (Saravanamuttoo *et al.*, 2001). Centrifugal and mixed flow compressors are geometrically very similar, however with significant differences in performance. Both types consist of a diffuser and an impeller, with the diffuser being either vaned or vaneless. The differences between mixed flow and centrifugal compressors are that mixed flow compressors have significantly larger mass flow rates, and is able to operate over wider ranges of mass flow rates at a specific rotational speed (Saravanamuttoo *et al.*, 2001).

The primary function of the compressor in a MGT is to supply compressed air to the combustion chamber.

2.2.1 Centrifugal compressors

The centrifugal compressor makes use of a centrifugal impeller and a radial diffuser. Figure 2.1 shows a MGT with its various components, and the position of the centrifugal compressor. The centrifugal impeller works as follows. First the air enters the impeller axially, gets transferred into the impeller blade passage and discharges radially. The impeller does work on the air, increasing its angular momentum, which increases the total pressure and which also leads to an increase in temperature.

The function of the radial diffuser is to convert most of the dynamic pressure(kinetic) energy, that exits the centrifugal impeller, into static pressure energy (Dixon, 1978). The diffuser can either be a radial vaned or radial vaneless. The use of the particular type of diffuser(vaned or vaneless) will depend on the operation and size constraints of the engine. Saravanamuttoo *et al.* (2001) states that the process of designing a combustion chamber is simplified when the velocity of the air entering the combustion chamber is as low as possible with high static pressure.

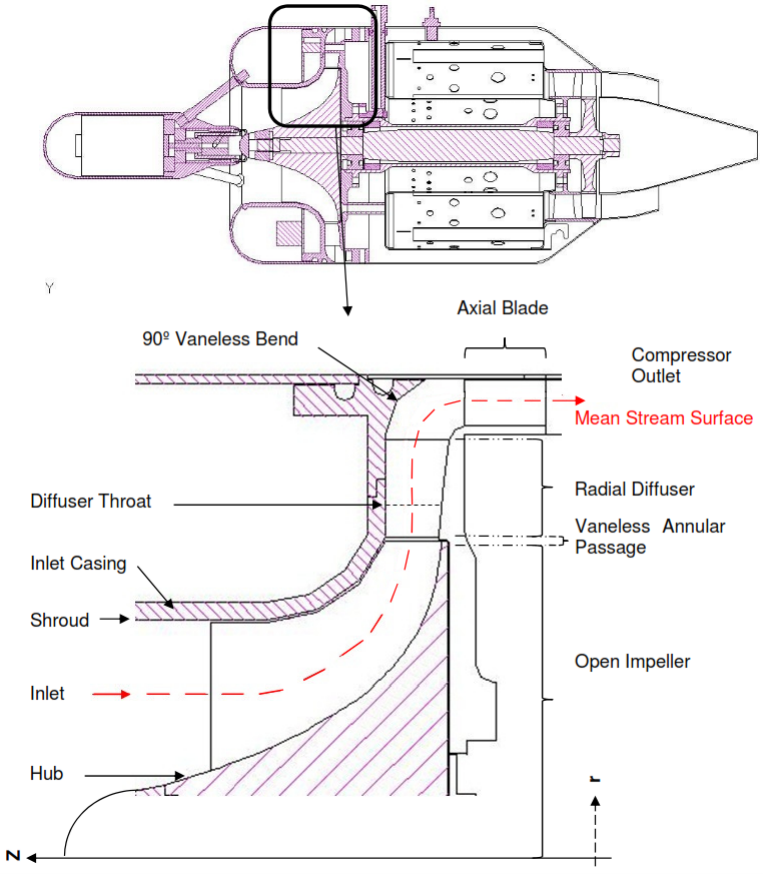

Figure 2.1: Centrifugal compressor r-z plane (Krige, 2012)

2.2.2 Mixed flow compressor

Mixed flow compressors are essentially centrifugal compressors that have a meridional impeller exit flow angle (α) between 0°and 90°, as illustrated in Figure 2.2. Japikse and Baines (1997) describe the mixed flow compressor as being a combination of a centrifugal and axial compressor, containing features of both. The axial component allows the mixed flow compressor to handle higher mass flow rates with a relatively small frontal area, while obtaining high pressure ratios in a single stage (Cevik, 2009).

According to Goldstein (1948), centrifugal compressors have the advantage of achieving higher pressure ratios in a single stage but it is handicapped by relatively low efficiencies and mass flow rates per unit frontal area. Mixed flow compressors, on the other hand are capable of handling much higher mass flow rates per stage. A higher mass flow rate can evidently lead to higher thrust output. Goldstein (1948) further states that the frontal area of the engine is important when considering its resultant drag. He adds that because axial compressors have the ability to attain large efficiencies and mass flow rates per unit frontal but are complex and expensive to manufacture, and relatively heavy, constructing a combination of the axial and centrifugal compressor types of engines would be simple, compact, light, and would accomplish high work output with a reduced frontal area.

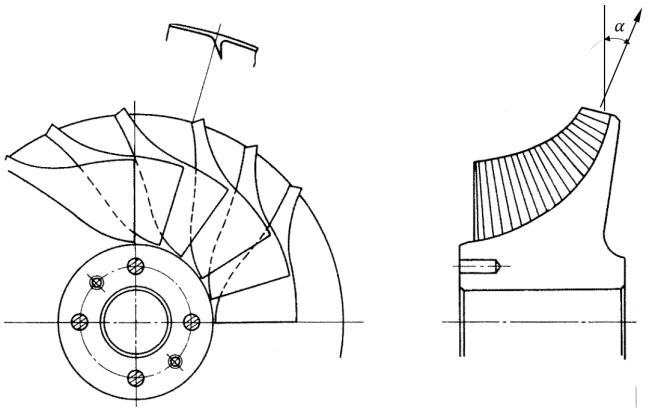

Figure 2.2: Mixed flow impeller meridional view (Kano *et al.*, 1984)

2.2.3 Compressor instabilities

There are a number factors that may cause a decrease in compressor performance and may cause compressor instability. The three most common instabilities in compressors are stall, system surge and choke. There are essentially two types of stall that occur in mixed flow and centrifugal compressors, namely static stall and dynamic stall. Static stall occurs where the conditions are stationary in nature and therefore can be associated with fixed locations in the

compressor (Japikse and Baines, 1997). This type of stall can be found in the stationary walls of the compressor such as stators and shroud walls. Static stall can simply be described as fluid separating from stationary walls that causes flow blockage in the adjacent passages. By contrast dynamic stall is related to the moving or rotating sections in the compressor. Dynamic stall can exist in components such as rotors, inducers and diffusers, and can be described as the imbalance between vector quantities. These vector quantities include impeller rotational speed and inlet velocity as well as a pressure ratio that is incompatible with the speed of the engine (Krige, 2012). Dixon (1978) describes dynamic stall as a two dimensional type of stall that occurs on the blade of the machine where a large wake exits the suction side of the blade, as can be seen in Figure 2.3.

Japikse and Baines (1997) defines a criterion for stall using the expressions in Equation 2.1 describing the slope of the pressure ratio and mass flow rate between the operating and stall point. The first criterion indicates metastable operation of the compressor, where the pressure ratio, mass flow rate characteristic slope is equal to zero. The second criterion is when the slope is negative, indicating stable operation of the compressor. The third criterion is when the slope positive, which indicates instability in the compressor stage.

$$\frac{\partial Pr}{\partial m} = 0$$

$$\frac{\partial Pr}{\partial m} < 0 \tag{2.1}$$

$$\frac{\partial Pr}{\partial m} > 0$$

The position of stall can then be quantified with a non-dimensional term referred to as the stall margin(SM). The stall margin is described by Equation 2.2:

$$SM = \frac{\dot{m}_o - \dot{m}_s}{\dot{m}_o} \tag{2.2}$$

where $\dot{m}_o$ and $\dot{m}_s$ describe the mass flow rates at operating point and stall point respectively. The stall margin is a quantity that allows designers to view how far the compressor design point is from stall. The aim is to achieve a relatively large stall margin. This will allow the compressor to operate over a wider range of mass flow rates.

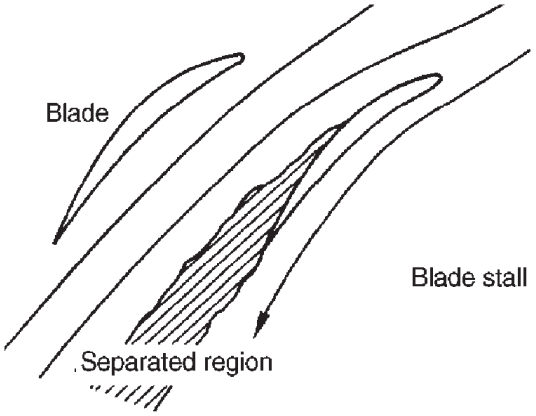

Figure 2.3: Blade stall (dynamic stall) (Dixon, 1978)

The component within the compressor that is most susceptible to stall is the diffuser. If the incidence angle of the air onto the diffuser blade is excessive, perhaps due to factors such as blockage or uneven flow, the vanes in the diffuser may stall (Dixon, 1978).

A second factor that influences compressor stability is system surge. Surge is the condition where the flow in the machine breaks down periodically. Ferguson (1963) states that surge is caused by the compressor characteristics. Consider Figure 2.4 with a compressor operating at point 3. A drop in mass flow rate due to a temporary blockage will cause an increase in delivery pressure (P_{03}). This occurrence will tend to return the mass flow rate back to point 3. Sayers (1990) identifies this point to be a point of stable operation. If the flow point drops to point 6 the pressure (P_{03}) will continue to decrease. This will cause a further drop in mass flow rate and pressure. This will happen until point 1 is reached. Once the pressure has reduced enough due to the drop in mass flow rate, the mass flow rate will increase until it reaches a limiting mass flow rate. It is at this point where the pressure will reduce again. This fluctuation in pressure and mass flow rate in such an unstable manner is called surge. Surge is especially disadvantageous because excessive surge can cause destruction of a compressor in a very short time (Arant, 1976).

Choke is the condition where no additional airflow can pass through the compressor. Choke can occur within the diffuser or the impeller throat. It can be observed when the total-to-total pressure ratio at a constant impeller rotational speed drops rapidly with a small change in mass flow rate (Krige, 2012). Figure 2.4 shows the theoretical centrifugal compressor characteristic curve. If the mass flow rate is increased it can be seen that the slope of the curve becomes negative. At point 5 there can be no further increase in mass flow rate. This indicates that sonic conditions have been reached (Sayers, 1990). It is at this point where choke occurs.

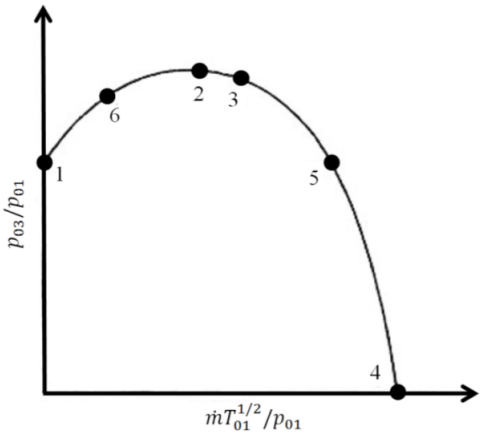

Figure 2.4: Compressor characteristic curve (van der Merwe, 2012)

2.3 Compressor theory

The centrifugal compressor consists of a rotor (impeller) and stator (diffuser). The impeller transfers a high velocity component to the air, and the diffuser decelerate the flow that in turn causes a static pressure rise. This section will discuss the theory behind the functioning of the compressor, by assessing the role of the impeller and the diffuser respectively.

2.3.1 Impeller theory

As the impeller rotates it transfers high velocity momentum to the air. The velocity components are illustrated using velocity triangles as shown in Figure 2.5, with the velocity triangle for the impeller inlet shown on the right and the impeller outlet shown on the left.

The air enters the flow channel until it reaches the inducer section with an absolute velocity C_1. C_1 is equal to the axial velocity (C_{a1}) in the impeller. if there is no inlet swirl ($C_{\theta 1} = 0$). A pre-whirl velocity component ($C_{\theta 1}$) can be added to adjust the operational mass flow rate with negligible variation in shaft speed or pressure ratio (van der Merwe, 2012). This pre-whirl can be achieved by adding guide vanes to the inlet of the channel.

The air is then translated into the impeller blade passages. This causes the kinetic energy of the air to increase. Because dynamic pressure is kinetic energy per unit volume flow, the increase in kinetic energy leads to an increase in dynamic pressure, which leads to an increase in total pressure and temperature. Japikse (1996) states that regardless of the state of the air, the air will receive a fundamental pressure rise that strongly varies with the $r^2\omega^2$ term. The air flows in the blade channels until it reaches the impeller tip at r_2. The blade

channel effectively acts as a rotating diffuser channel (Japikse, 1996). The centripetal acceleration in the channel is obtained by a pressure head, so that the static pressure of the air increases (Saravanamuttoo *et al.*, 2001). The air exits the impeller with a radial velocity C_{r2}, tangential velocity, $C_{\theta 2}$, and axial velocity C_{z2}, if it is a mixed flow impeller. The tangential component, $C_{\theta 2}$ at the exit would ideally be equal to the tip speed of the impeller U_2, however due to slip the tangential component at impeller tip is determined from the difference between U_2 and $\triangle C_\theta$. For mixed flow impellers the slip is reduced due to a reduction in the Coriolis forces (Diener, 2016). The energy imparted to the air by the impeller can be written as in Equation 2.3.

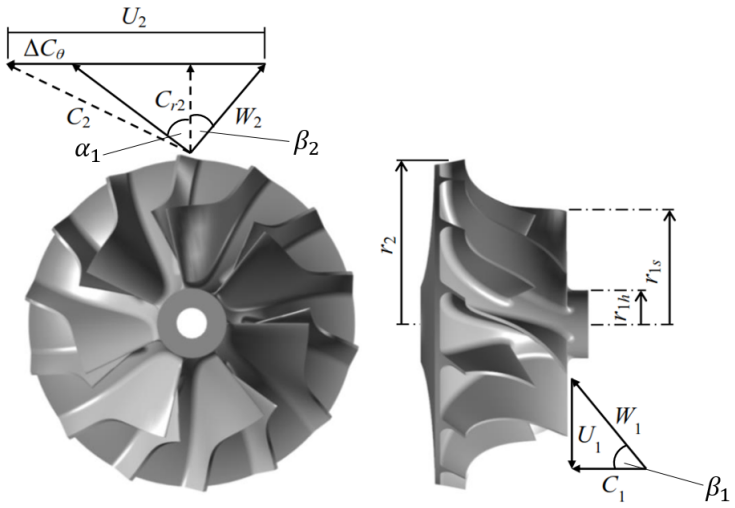

Figure 2.5: Impeller velocity triangles adapted from van der Merwe (2012)

$$W = \tau\omega \tag{2.3}$$

The torque (angular moment) that is conserved around an arbitrary axis that is determined from the inlet and exit conditions of the impeller, is depicted by Equation 2.4:

$$\sum \tau = \dot{m}(r_2 C_{\theta 2} - r_1 C_{\theta 1}) \tag{2.4}$$

The mass flow rate is determined from Equation 2.5:

$$\dot{m} = \rho_1 C_1 A_1 = \rho_2 C_2 A_2 \tag{2.5}$$

By substituting Equations 2.4 and Equations 2.5 into Equation 2.3 the energy transferred is represented by Equation 2.6, also known as the Euler turbo-machinery equation. Assuming the air exits the impeller at the same angle as the blade angle β_2, means that a slip factor (σ_s) of 1 will be assumed. In

reality the angle at which the air leaves the blade will not be the same as the blade angle β_2 and the slip factor will be less than 1.

$$W = \tau\omega = \sigma_s \dot{m}(U_2 C_{\theta 2} - U_1 C_{\theta 1}) \tag{2.6}$$

The blade speeds are calculated as $U = \omega r$ at any radius.

The flow through the compressor can be illustrated by means of a Mollier diagram, as seen in Figure 2.6, where the impeller operates between condition 1 and 2. The red line indicates the changes in static enthalpy states of the air. The work done by the impeller can be written in terms of the stagnation enthalpy change determined along a stream line, whereby the stagnation enthalpy through the impeller at any point is determined by Equation 2.7, where n is any position (point) in the compressor.

$$h_{0n} = h_n + \frac{C_n^2}{2} \tag{2.7}$$

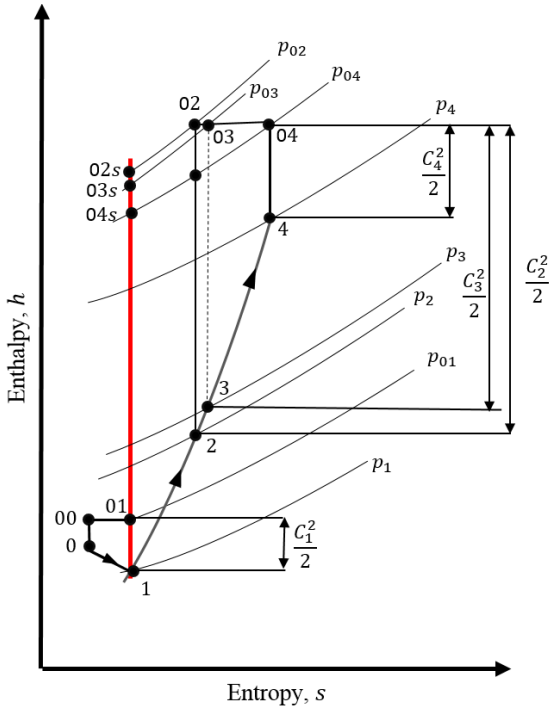

Figure 2.6: Mollier chart for centrifugal compressor

The energy imparted to the fluid can now be written in terms of the stagnation enthalpy calculated from inlet to outlet with Equation 2.8.

$$W = \dot{m}(h_{02s} - h_{01}) \tag{2.8}$$

Another parameter that can be useful is the rothalpy, I, depicted by Equation 2.9:

$$I = h_1 + C_1^2/2 - U_1 C_{\theta 1} = h_2 + C_2^2/2 - U_2 C_{\theta 2} \tag{2.9}$$

Dixon (1978) states that rothalpy is a fluid mechanical property that is important in the study of relative flows of rotational systems. From Equation 2.9 it shows that the value of the rothalpy is conserved. This makes it an important parameter for design purposes. The static enthalpy change of the air in the impeller can be written as in Equation 2.10.

$$h_2 - h_1 = \frac{(C_1^2 - C_2^2)}{2} + U_2 C_{\theta 2} - U_1 C_{\theta 1} = \frac{(U_2^2 - U_1^2)}{2} + \frac{(W_1^2 - W_2^2)}{2} \tag{2.10}$$

For constant specific heat and the air behaving as an ideal gas the static enthalpy change of the air can also be written as:

$$h_2 - h_1 = cp(T_2 - T_1) \tag{2.11}$$

where $c_p = \gamma R/(\gamma - 1)$ and γ is the ratio of specific heats. Using the ideal gas law ($Pv = RT$), the stagnation temperature can be written as in Equation 2.12.

$$\begin{aligned} T_0 &= T + \frac{C^2}{2c_p} \\ \frac{T_0}{T} &= 1 + \frac{(\gamma - 1)C^2}{2\gamma RT} \end{aligned} \tag{2.12}$$

To convert enthalpy to pressure and temperature the Gibbs equation can be used.

$$Tds = dh + \frac{1}{\rho} dp \tag{2.13}$$

This translates to the isentropic relationship in Equation 2.14 indicated by the red-line in the Mollier diagram in Figure 2.6.

$$\frac{p_{02}}{p_{01}} = \left(\frac{T_{02s}}{T_{01}} \right)^{\frac{\gamma}{\gamma - 1}} \tag{2.14}$$

Equation 2.14 is used if the pressure ratio is known and the temperature needs to be determined. It is specifically used in the 1-D design process of compressors and turbines.

2.3.2 Diffuser theory

The primary function of a diffuser in a centrifugal compressor is to decelerate the flow that exits the impeller and convert the high dynamic pressure into

static pressure. This is achieved by increasing the flow area ratio from inlet to outlet. The diffuser can be vaned or vaneless depending on the size constraints. Vaned diffusers will in most cases be used in small compact engines where size needs to be constrained. This section will focus on the theory and operation of a radial vaned diffuser. The velocity components at the inlet and outlet of the vaned diffuser is illustrated in Figure 2.7.

The air exits the impeller and enters a vaneless space before reaching the diffuser vanes. The air has a radial velocity, C_{r3} and tangential velocity, $C_{\theta 3}$ component when entering the diffuser. The air then diffuses through the diffuser and exits with a radial velocity, C_{r4} and tangential velocity, $C_{\theta 4}$. The increase in radius automatically causes the area to increase. This will in turn cause the velocity to decrease. The decrease in velocity will lead to a rise in static pressure.

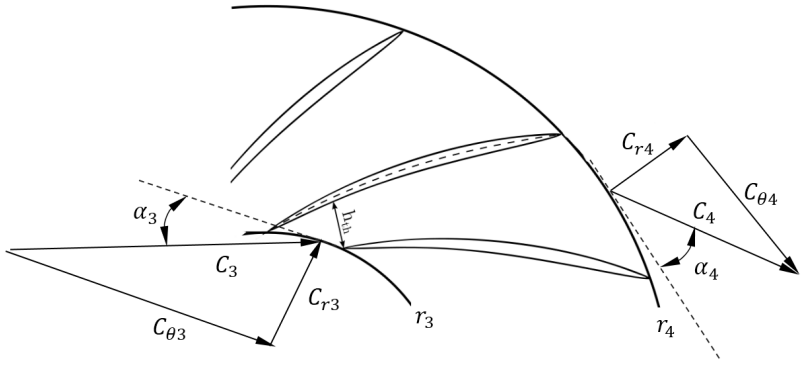

Figure 2.7: Diffuser velocity components

The energy imparted to the fluid through the diffuser is zero, this is due to no shaft work taking place in the diffuser. The process of the fluid passing through the diffuser is illustrated in the Mollier diagram in Figure 2.6 from point 2 to 4. Since there is no energy imparted to the air, this will lead to zero stagnation enthalpy change across the diffuser (Equation 2.15).

$$h_{04} = h_{03} \tag{2.15}$$

2.3.3 Pressure ratio and efficiency

The total-to-total pressure ratio, PR_{t-t}, is determined from the total pressure at the inlet and outlet of the compressor. For diffusers the static-to-static pressure ratio, PR_{s-s} is used since the goal of diffusers is to gain maximum static pressure recovery. For centrifugal compressors, the $PR_{t-t(0-4)}$ is affected by both the diffusion of the relative velocity and the change in radius in the

impeller. This is why a higher pressure ratio can be achieved per centrifugal stage than with axial flow compressors (van der Merwe, 2012).

$$PR_{t-t} = \frac{p_{04}}{p_{00}} \tag{2.16}$$

Another important performance indicator is the isentropic efficiency, which is the ratio of the work supplied to the compressor and the energy imparted to the fluid (Dixon, 1978). The efficiency is an important performance indicator. An improved efficiency can result in a reduction in the required power to drive the compressor for any given operating point (Orth *et al.*, 2001).

The isentropic efficiency is written as a function of the total temperatures and pressures at the inlet and outlet of the compressor as seen in Equation 2.17.

$$\eta_{t-t} = \frac{(h_{04s} - h_{00})}{(h_{04} - h_{00})} = \frac{\left(\frac{p_{04}}{p_{00}}\right)^{\frac{\gamma-1}{\gamma}} - 1}{\left(\frac{T_{04}}{T_{00}}\right) - 1} \tag{2.17}$$

The isentropic efficiency can also be calculated from total-to-static conditions, using total and static pressures and temperatures where required.

2.4 Diffuser geometric parameters

The primary function of a diffuser is to decelerate flow and convert the dynamic pressure into static pressure. This is achieved by an increase in area and thus a reduction in the velocity of the fluid. There are essentially two main types of diffusers that are used in centrifugal and mixed flow compressors, namely vaneless and vaned diffusers.

2.4.1 Vaneless diffuser

Vaneless channel diffusers serve as basis for the design of vaned radial diffusers in centrifugal compressors. These diffusers function by using the increase in area associated with an increase in radius to decelerate the flow to recover static pressure. This section aims to investigate the parameters that governs the design of diffusers by first considering annular passage diffusers, after which it will investigate vaneless radial diffusers and design parameters.

a) Annular passage diffuser

When designing annular diffusers there are three main aspects that need to be considered. The first aspect is the divergence angle denoted as 2θ. It indicates the angle between the walls of the channel. Aungier (2000) defines

the optimum divergence angle to be between 10° and 11° ($10 \leq 2\theta_c \leq 11$). Dixon (1978) and Runstadler (1969) found the best possible divergence angle to be between 8° and 10° ($8 \leq 2\theta_c \leq 10$). Alternatively Ashjaee and Johnston (1979) determines the optimum divergence angle to be equal to 9°, and Reneau *et al.* (1967) states this angle to fall in the range of 7° to 12° ($7 \leq 2\theta_c \leq 12$).

The second aspect to be considered is the non-dimensional length, L/W_3, where L is the length and W_3 is the inlet width of the diffuser (seen in Figure 2.8). Runstadler (1969) suggests the optimum non dimensional length (L/W_3) to be equal to 17. Reneau *et al.* (1967) achieved a peak static pressure recovery of 65% with a non-dimensional length of 9 and a divergence angle of 8°. To achieve the same static pressure recovery Reneau *et al.* (1967) used a non-dimensional length of 6.5 with a divergence angle of 12°.

Reneau *et al.* (1967) mapped the flow regimes of channel diffusers into a single plot and summed up the flow regimes. This is illustrated in Figure 2.9. The plot illustrates the area ratio, non-dimensional length and the divergence angle. The first stall condition is reached at line a-a. If the area ratio/divergence angle is increased further, the line of appreciable stall is reached. Japikse and Baines (1997) states that in the region surrounding the line of appreciable stall 50 % of transitionary stall can be allowed, but only on one wall or in one corner of the diffuser. With these conditions the diffuser would still be acceptable and can still deliver high static pressure recovery. Increasing the area ratio further, line b-b will be reached. Here the stall is fully developed and pressure recovery decreases significantly, as the area ratio is increased. A further increase in area ratio will cause line c-c to be reached, at this condition separation can occur on both sides of the diffuser wall. Increasing the area ratio even further will result in jet flow through the centre of the diffuser. Thus from Figure 2.9 one can deduce that peak performance can be obtained from the region marked "Large transitory stall" (Japikse and Baines, 1997).

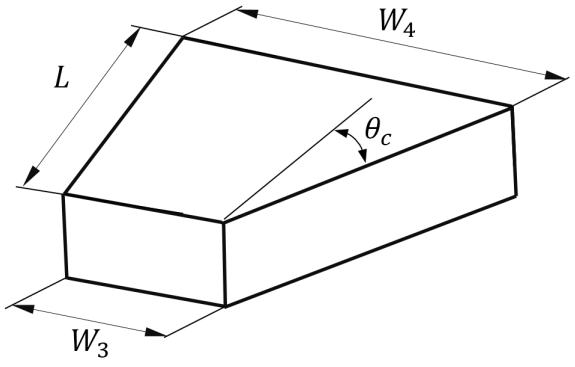

Figure 2.8: 2-D Diffuser

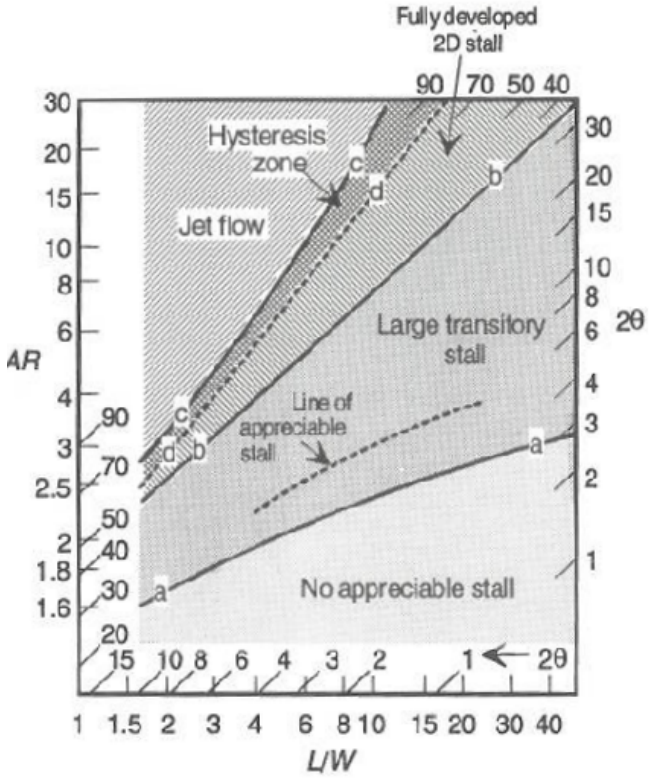

Figure 2.9: Flow regime in channel diffuser (Japikse and Baines, 1997)

b) Radial vaneless diffuser

In MGTs the vaneless diffuser is radial in nature if the compressor is centrifugal. The flow exits the impeller and enters the vaneless diffuser space where the fluid diffuses in the radial direction. The fluid is then directed axially with a vaneless bend from radial to axial. This is the simplest form of radial diffusers.

Vaneless diffusers have a much wider operating range than vaned diffusers. Although vaned diffusers can obtain a higher peak efficiency than vaneless diffusers at a given speed, their operating range is considerably narrower due to possible stall of the diffuser vanes (Ferguson, 1963).

With radial diffusers the design parameters mentioned in section 2.4.1b are less. The radial vaneless diffuser increases the static pressure by increasing the area with an increase in radius. There can however be flow separation at the channel walls if the channel walls are angled. Most radial channels however have a constant channel height. The primary factor that governs the design of radial vaned diffusers are friction losses.

2.4.2 Vaned radial diffuser theory

Vaned radial diffusers are used in MGTs due to the size constraints often imposed on MGTs. The vanes in the diffuser allow the diffuser to recover static pressure over a shorter radial length compared to a vaneless diffuser with the same radial length, making these type of diffusers advantageous for use in small gas turbines where size is a major limitation. The classic wedge type vaned diffuser is the simplest form of the vaned diffuser. Alternatively vaned diffusers can make use of airfoil shaped vanes, Figure 2.10 illustrates such a diffuser. Aungier (1988) used experimental data from 18 different vaned diffuser designs to develop a systematic design procedure for an airfoil vaned diffuser. The work done for this research primarily focuses on airfoil vaned diffusers. This section will outline the design method employed by Aungier (1988) for a radial diffuser.

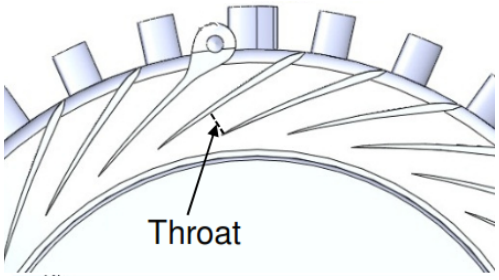

Figure 2.10: Vaned radial diffuser Krige (2012)

a) Vane diffuser performance

Before the design can commence the designer has to understand the constraints and parameters that govern the performance of the vaned diffuser. Aungier (2000) claims that conventional vaned diffusers are dependent on two basic diffusion mechanisms to achieve static pressure recovery. The first mechanism is the effective passage area, as it increases from inlet to discharge. The second mechanism is the blade loading, L, or the fluid turning effect. Aungier (2000) further states that an effective diffuser will make use of both mechanisms to achieve maximum static pressure recovery. The effective passage area increase is commonly known as the area ratio, $AR = A_4/A_3$. This is the ratio of the inlet and outlet area of the diffuser. The blade loading parameter is defined as:

$$L = \frac{\overline{\triangle C}}{C_3 - C_4} \tag{2.18}$$

where the numerator term in Equation 2.18 is defined as the average blade to blade velocity determined as follows:

$$\overline{\triangle C} = \frac{C_3 W_3 (cot\beta_3 - \frac{RC_{r4} cot\beta_4}{C_{r3}})}{L_B} \tag{2.19}$$

where, $R = r_3/r_2$, is the diffuser vaneless gap radius ratio, and L_B is the blade passage length. As a result of the static pressure rise through the diffuser, a useful performance parameter associated with diffusers is the static pressure recovery coefficient, C_P.

$$C_P = \frac{p_4 - p_3}{p_{03} - p_3} \tag{2.20}$$

The static pressure recovery coefficient indicates the percentage of inlet energy converted to static pressure through the diffuser (Krain, 1981). The C_P is calculated as the static pressure rise divided by the inlet dynamic head (Japikse and Baines, 1998), as written in Equation 2.20. Typical values for diffuser static pressure recovery coefficients are between 0.3 an 0.5, but can peak up to 0.8 and 0.9. Such peak values are however unlikely since it requires inlet flow that is highly uniform (Japikse and Baines, 1997). When the diffuser is considered to be ideal the pressure recovery is depicted by Equation 2.21:

$$C_{Pideal} = 1 - \frac{1}{AR^2} \tag{2.21}$$

Japikse and Baines (1997) claims that Equation 2.21 is useful and can deduce relationships such as the diffuser effectiveness, $\eta_D = C_{Pideal}/C_P$, and total pressure loss coefficient, $K = C_{Pideal} - C_P$.

b) Vaned diffuser design

The first step in the design process of the vaned diffuser proposed by Aungier (2000), is the vane inlet design. Firstly the inlet location of the vane, r_3, and the inlet blade angle, β_3, has to be determined. Aungier (2000) states that diffusers with a small vane inlet angle and a small number of vanes have a wider stable operating range. The inlet vane angle design range for most successful diffusers was found to be $16° \leq \beta_3 \leq 22°$ (Aungier, 2000). The primary objective of the diffuser inlet design is to match the flow of the impeller tip to the vane inlet. The location of the inlet will depend on the radius ratio, R, of the vaneless gap (see section 2.4.5).

The second step in the design process is sizing of the vaned diffuser. The sizing includes determining the number of vanes, the blade loading, the vane length and the divergence angle. The blade loading limits proposed by Aungier (2000) are:

$$0.3 \leq L \leq 0.333 \tag{2.22}$$

with the blade loading parameter defined by Equation 2.18. The number of vanes determined by Aungier (2000) is calculated using Equation 2.23:

$$Z = \frac{2\pi(r_4 \sin\beta_4 - r_3 \sin\beta_3)}{(t_4 b_4 + b_3[\tan\theta_c L_B - t_3])} \tag{2.23}$$

where L_B represents the vane length and is determined by Equation 2.24:

$$L_B = \frac{2r_3(R-1)}{\sin\beta_3 + \sin\beta_4} \tag{2.24}$$

The number of diffuser vanes required for a stable operating range should always be minimised. Aungier (2000) proposes a preferred number of vanes as the number of impeller blades plus-minus one ($Z = Z_I \pm 1$). The range of the number of vanes that is beneficial for avoiding stall incidence is between 10 and 20 , ($10 \leq Z \leq 20$). Aungier (2000) states that if the number of vanes does not fall in this range then $\mid Z - Z_I \mid \geq 8$ is required. Orth *et al.* (2001) additionally states that the incorrect number of diffuser vanes can cause rotor blade resonance upstream of the diffuser. Another constraint that is important in diffuser sizing is the divergence angle. The vane divergence angle proposed by Aungier (2000) is:

$$10^\circ \leq 2\theta_c \leq 11^\circ \tag{2.25}$$

These values are obtained from the upper and lower limits of the blade loading parameter constraints using Equation 2.26 (Aungier, 2000).

$$\theta_c = \tan^{-1}\left[\frac{\pi(r_4\sin\beta_4 - r_3\sin\beta_3)}{ZL_B}\right] \tag{2.26}$$

The sizing for diffuser design is a process that will require the designer to establish which parameters are more important and significant to the design. Aungier (2000) provided alternative design specification combinations to aid in the design process. These combinations are tabulated in Table 2.1.

Table 2.1: Design specifications

Combination	**Select**	**Compute**
1	R, AR, Z	$2\theta_c, L$
2	$R, AR, 2\theta_c$	$Z, L, revise A_R or 2\theta_c$
3	$R, 2\theta_c, Z$	A_R, L
4	R, β_4, Z	$A_R, 2\theta_c, L$
5	$R, \beta_4, 2\theta_c$	Z, L, A_R

The third step in the design process, is the vane design itself. The vanes are designed by imposing thickness to a camberline. The camberline proposed by Aungier (1988) is defined in Equation 2.27 with respect to the η parameter.

$$\theta(\eta) = A\ln(\eta) + B(\eta - 1) + C(\eta^2 - 1) + D(\eta^3 - 1) \tag{2.27}$$

where $\eta = r/r_3$, r is the radius at any point through the diffuser and r_3 is the vane inlet radius. To compute the constants A, B, C, and D, four boundary

conditions are needed. The first two are computed with the inlet and outlet (leading and trailing edge) blade angles differentiating Equation 2.27 to obtain Equation 2.28.

$$\cot\beta = \eta\frac{d\theta}{d\eta} = A + B(\eta) + 2C(\eta^2) + 3D(\eta^3) \tag{2.28}$$

The other two boundary conditions are selected to control the form of the blade loading distribution. This is done by defining the blade curvature parameter K at the leading and trailing edge, where the parameter K is determined as;

$$K = \frac{R-1}{\cot\beta_4 - \cot\beta_3}\frac{d\cot\beta}{d\eta} \tag{2.29}$$

The resulting constants from the aforementioned process yield:

$$D = \frac{(\cot\beta_4 - \cot\beta_3)(K_3 + K_4 - 2)}{3(R-1)^3} \tag{2.30}$$

$$C = \frac{(\cot\beta_4 - \cot\beta_3)(K_4 - K_3)}{4(R-1)^2} - \frac{-9D(R+1)}{4} \tag{2.31}$$

$$B = \frac{K_3(\cot\beta_4 - \cot\beta_3)}{R-1} - 4C - 9D \tag{2.32}$$

$$A = \cot(\beta_3) - B - 2C - 3D \tag{2.33}$$

To complete the vane design the vane thickness needs to be defined. Aungier (2000) used the NACA 66-006 airfoil shape for the diffuser vane design. The analytical approximation of the vane thickness is described by the expressions in Equation 2.34:

$$\begin{aligned} t_b/t_{bmax} &= t_0 + (1-t_0)(2x/c)^n; && for x/c \leq 0.5 \\ t_b/t_{bmax} &= t_0 + (1-t_0)((2-2x)/c)^n; && for x/c > 0.5 \\ t_0 &= ([t_b3 + (t_b4 - t_b3)x/c])/t_{bmax} \end{aligned} \tag{2.34}$$

where t_0 is described as the influence of the leading and trailing edge radii, x is the distance along the chord, c is the chord length and the maximum thickness and t_{bmax} is defined by the designer. The exponent n in Equation 2.34 is defined by the conditional function in Equation 2.35 for a given blade length and camber ratio (x/c).

$$\begin{aligned} n &= 0.755(0.57 - x/c); && for x/c \leq 0.539 \\ n &= 1.225(x/c - 0.52); && for x/c > 0.539 \end{aligned} \tag{2.35}$$

2.4.3 De-swirlers

As the air exits the radial diffuser it enters a vaneless bend that directs the flow axially. The position of the de-swirler is depicted by "axial blade" in Figure 2.1. The function of the axial de-swirlers is to remove as much of the swirl component as possible before it enters the combustion chamber. Beér and Chigier (1972) gives a definition for swirl (S_N) as the relationship of the axial flux of angular momentum (G_t) and the axial thrust (G_z) in Equation 2.36.

$$S_N = \frac{2G_t}{D_N G_z} \tag{2.36}$$

where swirl is considered weak for $S_N < 0.4$, strong for $S_N > 0.6$, and moderate for a value of S_N between 0.4 and 0.6.

In cases where multi-stage centrifugal compressors are used, it is imperative to remove the swirl component before it enters the eye of the consecutive impeller. The fluid leaving the de-swirl vanes may be mixed and additional guide vanes may be required to establish a desired flow angle in the consecutive impeller (Japikse and Baines, 1997).

To fully understand the importance of de-swirlers in centrifugal compressors one has to look at the influence of swirl on the performance of the combustion chamber. The majority of MGT engines make use of annular type combustion chambers. Annular type combustion chambers are widely used due to their low pressure loss and are considered ideal for small gas turbine engines. A negative characteristic of annular combustion chambers is that a slight change in the inlet velocity profile can lead to a significant variation in outlet temperature distribution that can influence the performance of the combustion chamber (Lefebvre, 1983).

There is limited literature available that considers the effect of swirl on annular combustion chambers. Basson (2016) investigated the effect that inlet swirl has on the mass flow distribution and flow structures in the combustion chamber of a BMT120-KS MGT, by performing experimental and numerical fluid dynamics analysis. She discovered that inlet swirl has no influence on the mass flow distribution in the BMT120-KS engines, combustion chamber, but found that inlet swirl has a significant influence on the flow structures. Basson (2016) did not consider the effect of inlet swirl on combustion chamber performance.

Since one of the main reasons for using annular combustion chambers is to obtain the minimum total pressure loss, it is advised that strong swirl be removed to effectively shorten the flow path through the combustion chamber.

2.4.4 Continuous diffuser vanes

The continuous vane design replaces the conventional vaned radial diffuser with axial de-swirlers with a continuous blade design to reduce flow separation that occurs at the vaneless bend between the de-swirlers and the radial diffuser section.

Jie and Guoping (2010) designed a continuous vaned diffuser for a MGT with a maximum diameter of 110 mm. The diffuser was developed to replace the old conventional wedge type radial diffuser and axial de-swirlers. The resultant geometry had a 11% thrust improvement and a 9% decrease in fuel consumption and static pressure recovery coefficients of over 0.65.

Ling *et al.* (2007) investigated the difference between using the conventional wedge type diffusers versus the new continuous vane type diffusers. They used the KJ66 engine that makes use of a wedge type radial diffuser with axial de-swirlers in a centrifugal compressor. The compressor had a major diameter of 108 mm and a 71 mm diameter centrifugal impeller. The reason for the investigation was to improve operating range, attempting to obtain a higher choke mass flow rate value. Although the new design had considerably higher PR_{t-t} and η_{t-t} the choke mass flow rate was lower.

Wilkosz *et al.* (2014) designed a new type of de-swirler. The study was done on tandem de-swirlers and replaced it with a single continuous vane. The study found that the tandem vanes had a smaller stable boundary layer compared to the single vanes. The single vane was given more vanes to increase its solidity and compensate for the large boundary layer that forms. The static pressure recovery coefficient of the resultant design improved by to up to 5%.

2.4.5 Diffuser impeller interaction

It is imperative for the design of diffusers to quantify the effects of impeller-diffuser interaction. This section briefly discusses the impeller-diffuser interaction by looking at the impeller discharge flow, and the vaneless space downstream of the impeller exit.

a) Impeller discharge flow

The state of flow exiting the impeller is the most important factor to consider when designing a diffuser. The impact of vaned diffusers on the performance of the compressor stage depends on parameters such as inlet flow angle, turbulence, impeller exit flow non-uniformities and Mach number (Filipenco *et al.*, 1998). The flow exiting the impeller is highly mixed and unsteady. This unsteady mixed flow is caused by the shroud tip gap leakage vortex (Kirtley and

Beach, 1992). Casey and Rusch (2014) and Eckardt (1975) describes the flow exiting the impeller as unsteady with strong spanwise and circumferential distortions.

Filipenco *et al.* (1998) and Deniz *et al.* (2000) investigated the effect of the inlet flow field on diffuser static pressure recovery. It was found that pressure recovery was independent of the diffuser's inlet flow conditions. Although some literature claim that the distorted flow at the impeller exit has an influence on the performance of the diffuser, Filipenco *et al.* (1998) ascribes this to the inappropriate quantification of the dynamic pressure at the diffuser inlet.

The flow exiting the impeller has a high tangential velocity component due to the high impeller tip velocity. The high tangential velocity causes a high flow angle (α_c). This flow angle is an important factor to consider because it determines the diffuser inlet vane angle ($\beta_3 = i + \alpha_c$). To avoid premature flow separation from the diffuser vane walls, a suitable incidence angle (i) has to be selected.

b) Vaneless gap

The vaneless gap is a gap between the impeller blade trailing edge and the diffuser vane leading edge. Figure 2.11 illustrates the vaneless gap. An increase in the length of the vaneless space between the impeller and diffuser leads to a decrease in Mach number at the diffuser vane leading edge (Ziegler *et al.*, 2002). The presence of high Mach numbers can lead to premature choke in the diffuser throat. Alternatively Dallenbach and Van Le (1960) proposed a diffuser vane leading edge that is swept back, that will mitigating shock waves thus increasing choke mass flow rate. The vaneless space also aids with the distorted flow wake exiting the impeller by adjusting the flow profile before it enters the vanes (Aungier, 1988). The highly distorted unsteady flow exiting the impeller also influences the pressure recovery expected by the diffuser (Krain, 1981). The size of the vaneless space is usually between 5% and 15% of the impeller tip radius (Casey and Rusch, 2014). This value is however not fixed and numerous other references have different criterion's for the size of the vaneless space.

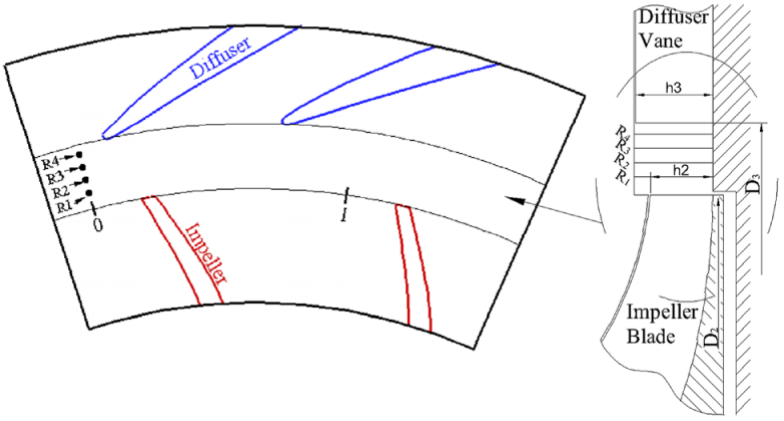

Figure 2.11: Vaneless gap (Gaetani *et al.*, 2012)

The vaneless gap is quantified in most literature as the radius ratio (r_3/r_2) between the impeller exit radius and the diffuser vane leading edge radius. Aungier (2000) recommends a radius ratio of between 1.06 and 1.12 ($1.06 \leq r_3/r_2 \leq 1.12$) where the upper value limits the vaneless space to minimise the friction losses, with a longer vaneless space resulting in larger friction losses. Aungier states that the lower limit provides space for the distorted impeller flow profiles to smooth out and the blade wakes to decay before entering the diffuser vanes.

Ziegler *et al.* (2002) investigated the experimental flow interactions between an impeller and diffuser. They varied the diffuser exit velocity with a radius ratio between 1.04 and 1.14 ($1.04 \leq r_3/r_2 \leq 1.14$). It was found that there was a significant reduction in the impeller wake with an increase in radius ratio. They also discovered that there is a reduction in diffuser vane loading with a reduction in vaneless gap due to the presence of impeller wake. Ziegler *et al.* (2002) found that smaller vaneless gaps produced a higher diffuser vane inlet total pressure.

Shum *et al.* (2000) investigated the effect that a change in the vaneless gap has on the performance of the impeller and the compressor. Shum *et al.* looked at three different diffuser gaps with radius ratios, 1.054, 1.092 and a vaneless diffuser ($r_3/r_2 = \infty$) the diffusers were virtually identical. The investigation concluded that impeller diffuser interaction has a significant effect on the performance of the compressor stage.

Chapter 3

Diffuser mean line design

3.1 Introduction

This chapter discusses the 1-D mean line design process of the cross-over diffuser (CD) for a mixed flow compressor. The mixed flow impeller was developed by Diener (2016). The mean line diffuser design (MLDD) was done with the use of a mean line code (MLC). The MLC is adapted from the code developed by Burger (2016) and is based on theory presented by Aungier (2000) as discussed in section 2.4.2.

MLDD was performed by first designing a vaneless cross-over passage, adapting its curvature and then evaluating its performance. Once the performance of the vaneless passage was considered satisfactory the vanes were added to the passage. The vane's characteristics were then adapted to find the best possible performance. This was then taken as the final MLDD.

3.2 Mean line code

This section discusses the MLC and adaptations that were performed. The MLC was written using MATLAB®, and it's developed by Burger (2016) to design a CD for a 200 N thrust prototype engine. The code is divided into three main sections, the input parameters, the main code, and the output, as illustrated with a flow chart in Figure 3.1.

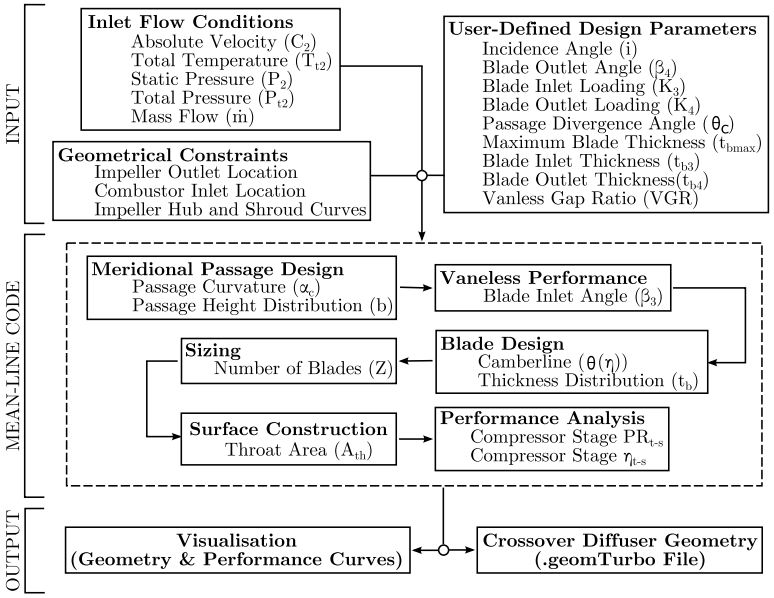

Figure 3.1: Mean line code overview (Burger, 2016)

3.2.1 Input

The input parameters are divided into three sub parts, namely inlet flow conditions, user defined parameters and geometrical constraints.

a) Inlet flow conditions

The inlet flow conditions are obtained from CFD simulations, determined at the exit of the impeller. The values are obtained from an evaluation plane that is situated at the tip of the impeller.

b) User defined parameter

The user defined parameters are the most important part of the MLC because it forms the basis of the MLDD. These parameters can be varied to satisfy the design specifications. The list of parameters can be seen in Figure 3.1.

c) Geometrical constraints

The geometrical constraints are important due to the MGT's limited size. The user must input the diffuser outlet locations (radial and axial), the impeller hub and shroud curves, and the impeller main and splitter blade geometries.

3.2.2 Main code

The main part of the code is used to perform the geometry construction of the diffuser. The steps for creating the geometry are provided below:

a) Meridional passage design

The code first generates the hub and shroud meridional contours with the use of Bezier curves. An illustration of the Bezier curve is shown in Figure 3.2. The end reference points are determined from the geometric centre of the user defined outlet locations of the impeller and the diffuser respectively. The limiting point is determined from the diffuser inlet and outlet meridional passage angles (α_a), where the CD axial outlet line intersects with a line that has a meridional passage angle of α_{2a}. The diffuser outlet passage flow angle is axial ($\alpha_{4a} = 0°$) and the inlet diffuser passage flow angle is given by Diener (2016) as $\alpha_{3a} = 74.5°$. The shroud and hub meridional contours are constructed from Quasi-normals perpendicular to the Bezier curve. The curvature of the meridional curves could be altered by adjusting the reference points.

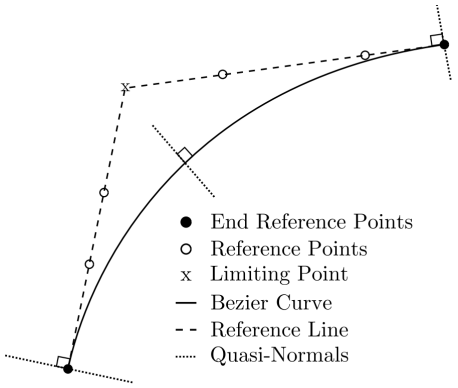

Figure 3.2: Bezier curve (Burger, 2016)

b) Vaneless gap performance

After the meridional passage has been created, the code determines the diffuser inlet vane flow conditions (state 3), which are the vaneless gap exit flow conditions. This is done to determine the diffuser inlet flow angle (α_{3c}) and subsequently the vane inlet angle (β_3). The diffuser outlet vane angle (β_4) is set in the user defined parameter section of the mean line code. The vaneless space was assumed to have a small total pressure loss of 0.1% (Aungier, 2000). The total pressure at the CD vane inlet is calculated as in Equation 3.1:

$$P_{03} = P_{02} - (P_{02} - P_2)0.001 \tag{3.1}$$

Appendix C provides a sample calculation for the 1-D analysis.

c) Blade design

The diffuser vanes were subsequently constructed by using Equations 2.27 to 2.35, where $\eta = r/r_3$. The MLC uses $\eta = m/m_3$, to account for both the radial

and axial change, where m is the meridional passage length ($m = \sqrt{z^2 + r^2}$). Figure 3.3 illustrates the meridional blade angle and camber angle definitions that are used in Equations 2.27 to 2.35.

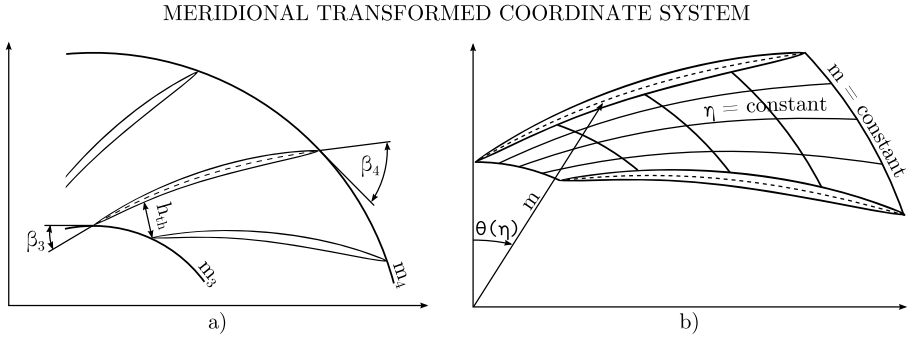

Figure 3.3: Meridional a) Blade angle and b) Camberline-angle definitions (Burger, 2016)

d) Sizing and blade surface construction

The next step was to calculate the number of vanes with the use of Equation 2.23, followed by the construction of the vane surfaces by using the contours of the hub and shroud. The primary vane surface coordinates are given in Equation 3.2.

$$\begin{aligned} x &= \bar{x} \pm \frac{1}{2} t_b T_x \\ y &= \bar{y} \pm \frac{1}{2} t_b T_y \\ z &= \bar{z} \pm \frac{1}{2} t_b T_z \end{aligned} \tag{3.2}$$

where the vector, $\vec{T}$, is determined from Equation 3.3, and $\bar{x}$, $\bar{y}$ and $\bar{z}$ are the Cartesian coordinated of the blade at the hub and shroud (meridional passage coordinates of blade)

$$\vec{T} = \vec{S} \times \vec{B} = T_x \vec{i} + T_y \vec{j} + T_z \vec{k} \tag{3.3}$$

The vector $\vec{S}$ is a defined unit vector tangent to the vane mean line in the stream surface, $\vec{B}$, and $\vec{T}$ is a vectors that is normal to the vane mean surface. The vectors, $\vec{S}$ and $\vec{B}$ is further discussed in Appendix A.

e) Performance analysis

The final step of the code is to perform 1-D performance calculations of the MLDD. A sample of the 1-D performance calculation is provided in Appendix C.

3.2.3 Output

The geometry output obtained from the MLC was in the form of a *.geomTurbo* file. The *.geomTurbo* file is the geometry file required by the numerical analysis software code, NUMECA in order to create the grid that will be used in the numerical solver. The *.geomTurbo* file format is discussed in Appendix B.

3.3 Vaned crossover diffuser design

This section discusses the design procedure of the CD with the use of the MLC. The CD design was performed systematically to achieve the best possible compressor performance, with the mean line designed diffuser. Figure 3.4 provides a flow chart to illustrate the CD design process. The passage curvature was varied manually to find the best vaneless CD design. If the vaneless CD could not be improved further manually, vanes were incorporated into the vaneless passage and simulated numerically. The vane parameters were varied manually to find a satisfactory vaned CD design. The resultant geometry of this process was taken as the final MLDD.

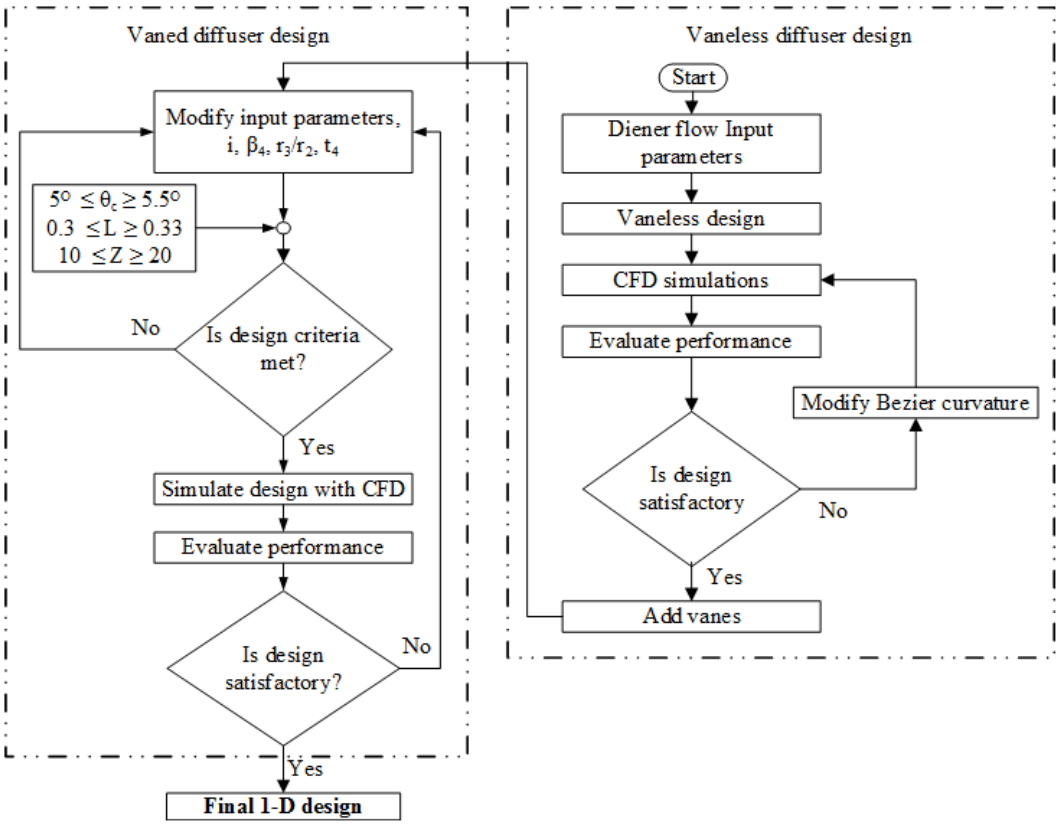

Figure 3.4: Mean line design process

3.3.1 Performance and size specifications

The performance and size specifications of the compressor were obtained from the CSIR. The CSIR used GasTurb12 (Martinjako, 2014) to perform cycle calculations of the engine to determine the required performance specifications. The combustion chamber exit temperature was set to 1150 K. This yielded a compressor stage total-to-total isentropic efficiency ($\eta_{t-t(0-4)}$) requirement of 85% and a compressor stage total-to-total pressure ratio ($PR_{t-t(0-4)}$) of 3.83. The mass flow rate was determined to be 0.85 kg/s at an impeller rotational speed of 95000 rpm. The thrust obtained was 520 N that fell below the thrust target of 600 N. The thrust can however be improved by increasing the combustor exit temperature or increasing the compressor outlet total pressure. However, the increase in temperature at the combustor exit would require the use of high temperature resistant materials such as ceramics or high performance alloys.

No specific diffuser performance specifications and size constraints were specified. However most diffusers in micro gas turbines (MGTs) are required to have an exit flow angle (α_{4c} measured from the tangent) that is axial as possible, $\alpha_{4c} > 0°$, but $\alpha_{4c} \not> 90°$. The reason for this angle as literature indicates is to minimise the effective flow length in combustion chamber to reduce the total pressure losses. The CD's main function is to increase the static pressure at the compressor outlet without lowering the $PR_{t-t(0-4)}$ below the required value of 3.83. A summary of the compressor specifications at design point ($\dot{m} = 0.85\ kg/s$) is given in Table 3.1.

Table 3.1: Specification summary

Quantity	$PR_{(t-t)}$	$\eta_{(t-t)}$	Diffuser exit flow angle (α_{4c})
Specification	>3.83	>85%	0°

The impeller blades and meridional geometries were imported into the MLC. The locations for the diffuser outlet were set in the user input parameters section of the MLC. The meridional passage used in the CFD analysis was given a pinched outlet to ensure that there is no back flow at the outlet. The size constraints for the entire MGT engine are 400 mm in the axial direction and a maximum diameter of 180 mm. The mixed flow impeller has an axial length of 80 mm (from inlet to impeller blade exit) and axial blade length of 30 mm. The maximum impeller diameter is 55.5 mm.

3.3.2 Vaneless crossover diffuser

Constructing the vaneless CD passage was the first step in designing the vaned CD. The initial inlet flow conditions used for the vaneless crossover passage

design were obtained from CFD results attained from Diener (2016). The simulation geometry used by Diener is provided in Appendix D. The resultant characteristic curves for the passage are shown in Figure 3.5. As seen from the characteristic curves there are clear differences between the results obtained by Diener for the total-to-total pressure ratio and total-to-total isentropic efficiency at design point. The difference are assumed to be primarily due to the difference in mesh count (3.6 million for Diener (2016) and 4 for the current study) of the simulations. It was also discovered that were inconsistencies in the results when the evaluation plane was situated in the vaneless gap. This was largely due to the recirculation bubble that was formed at the trailing edge of the impeller. The input flow conditions are determined from a evaluation plane that is situated at the impeller exit at a radius of 58 mm to keep consistent with Diener's evaluation plane location. The input flow conditions obtained from the evaluation plane are given in Table 3.2.

Table 3.2: Input flow conditions

Quantity	Unit	Value
Absolute velocity (C_2)	m/s	462.669
Total temperature (T_{02})	K	501.908
Static pressure (P_2)	Pa	229578
Total pressure (P_{02})	Pa	539078
Mass flow rate ($\dot{m}$)	kg/s	0.8572

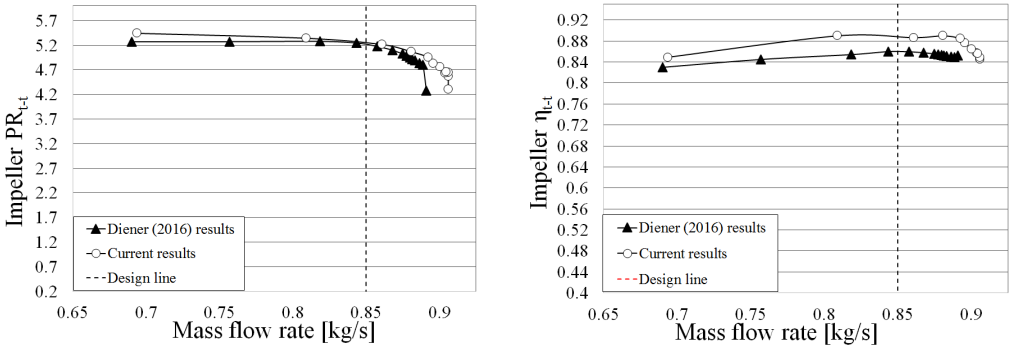

(a) (b)

Figure 3.5: a) Impeller total-to-total pressure ratio b) Impeller total-to-total isentropic efficiency

The meridional passage curvature was discretely varied to obtain the best possible 1-D vaneless performance. This was done by varying the rate of passage turn of the meridional passage Bezier curves. The primary objective of the vaneless passage design was to obtain the best possible vaneless passage to

which vanes could be added. The vaneless passage is required to have the highest possible $PR_{t-t(0-4)}$ and $\eta_{t-t(0-4)}$. A maximised C_P across the diffuser was also a required output. The passage curvature parameters were varied such that choke would not occur below the design point mass flow rate of 0.85 kg/s.The resultant meridional passage geometry is illustrated in Figure 3.7. The compressor with the best vaneless CD design was then numerically simulated at the design conditions. The impeller outlet conditions were again measured and the results were used as the new inlet flow conditions for the use in the vaned design process.The results are shown in Table 3.3. The resultant performance curves for the final vaneless channel is shown in Appendix H.1.

Table 3.3: New inlet flow conditions

Quantity	**Unit**	**Value**
Absolute velocity (C_2)	m/s	480.43
Total temperature (T_{02})	K	510.53
Static pressure (P_2)	Pa	239727
Total pressure (P_{02})	Pa	585881
Mass flow rate ($\dot{m}$)	kg/s	0.8499

3.3.3 Vaned diffuser design

After the vaneless channel in section 3.3.2 had been designed vanes were added to the channel. Several of the vane user defined design parameters were varied to obtain the best possible vaned diffuser design without changing the meridional passage geometry. However some of the design parameters were kept constant to minimise the number of varying parameters. The values for the parameters that were not varied were obtained from Burger (2016). The parameters used from Burger (2016) were the maximum blade thickness (t_{bmax}), the inlet and outlet blade curvature parameter (K_3, K_4), and the divergence angle (θ_c). The constant parameters and their values are listed in Table 3.4.

Table 3.4: Constant design parameters

Parameter	t_{bmax}	K_3	K_4	θ_c
Value	$2mm$	2	2	5.5°

Increasing the maximum vane thickness will induce a lower compressor choke mass flow rate, thus reducing the operating range. A smaller vane thickness (1 mm) is not feasible from a manufacturing perspective. Burger (2016) analysed the effect of increasing the vane thickness of the diffuser. He found that an increase in vane thickness decreased the operating range and the performance of the diffuser.

The inlet and outlet blade curvature parameters was kept constant as literature indicated that a moderate vane curvature parameter of 2 is preferred. The vane curvature parameter describes the vane curvature where, a low vane curvature parameter at the diffuser vane LE induces a sharp vane curvature that in turn causes the compressor to choke at a lower mass flow rate. At a high diffuser inlet vane curvature parameter, the vane curvature induces a high choke mass flow rate but a high stall mass flow rate, significantly lowering the operating range of the compressor. Increasing the inlet vane curvature parameter for the diffuser decreases stall mass flow rate. However, a low inlet vane curvature parameter allows a large operating range but will limit the blade curvature and consequently the ability to remove outlet swirl. The divergence angle was set at the upper limit of the range ($5 \leq \theta_c \leq 5.5$) required by Aungier (2000).

The remaining parameters ($\beta_4, r_3/r_2, t_{b4}, i$) were discretely varied to obtain the best MLDD. These parameters were varied in such a way as to adhere to the design criteria set by Aungier (2000) i.e; a blade loading parameter(L) not greater than 0.3, the number of vanes(Z) must be between 10 and 20 and the divergence angle(θ) must be between 5° and 5.5° and as can be seen from table 3.4 the divergence angle criteria is already adhered to. The best MLDD was selected when the $\eta_{t-t(0-4)}$ and the $PR_{t-t(0-4)}$ values could not be improved further by the discrete varying of parameters. A better MLDD could be obtained if a optimisation algorithm is employed into the MLC, however this was outside the scope of the research. The MLDD was however further optimised in Chapter 5. The vane loading parameter is calculated in the mean line code with Equation 2.21 and the number of vanes are calculated with Equation 2.23. The parameters that provided the best MLDD are tabulated in Table 3.5.

Table 3.5: Final design parameters

Parameter	t_4	r_3/r_2	Z_{VD}	β_4	i	L
Value	$1mm$	1.18	20	67°	2.8°	0.2893

The inlet flow angle was also inspected visually to ensure low incidence between blade and fluid flow. This was done to ensure that no premature flow separation occurred on the vane wall, and the diffuser incidence losses are minimised. A vector plot illustrating the flow alignment with the vane inlet is provided in Figure 3.6.

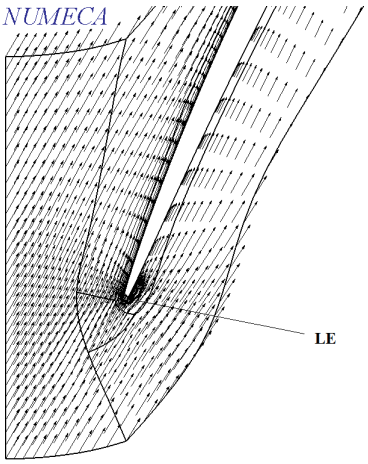

Figure 3.6: Vector plot and mid meridional contour

It is important to note that the vaneless gap radius ratio (r_3/r_2) was set to 1.18. Although this was outside the radius ratio ($1.06 \leq r_3/r_2 \leq 1.12$) proposed by Aungier (2000) it was set to compensate for the unsteady recirculating flow that exits the impeller and reduce the Mach number. The recirculating flow can be seen in Figure 3.7.

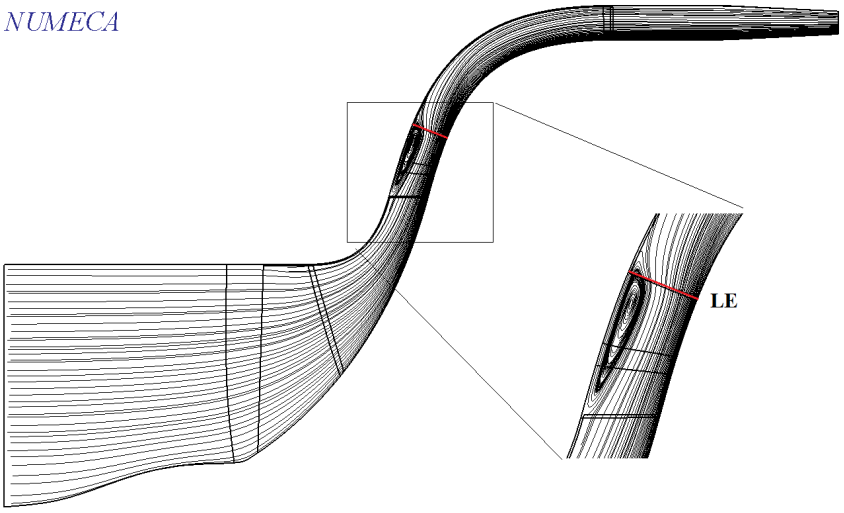

Figure 3.7: Meridional Streamlines

A gap size smaller than 1.18 resulted in choke being predicted by the MLC. The radius ratio of 1.18 was accepted because a large vaneless gap would assist with flow mixing in the unsteady wake region of the impeller outlet (Aungier, 2000). A larger vaneless gap essentially allows the flow enough distance to mitigate the flow distortions . The outlet blade thickness(t_4) was set to 1 mm to allow the optimisation process to use the outlet thickness as a variable parameter. A 1 mm outlet vane thickness also allowed the number of vanes

to decrease without decreasing vane solidity. The blade outlet angle was set to 63°, which was adapted by the MLC to 67°. The blade loading parameter was found to be less than 0.3. This is acceptable according to the criterion ($L < 1/3$) provided by Aungier (2000). The resultant geometry was then simulated numerically (the numerical analysis will be discussed in chapter 4).

The 1-D MLC performance results for the MLDD were compared to the CFD performance results by means of characteristic curves. Figure 3.8 compares the compressor performance and Figure 3.9 compares the diffuser performance. The compressor $PR_{t-t(0-4)}$ and $\eta_{t-t(0-4)}$ are compared in Figure 3.8a and 3.8b respectively . The diffuser performance results are compared in Figure 3.9 where Figure 3.9a and 3.9b show the C_P and $PR_{s-s(2-4)}$ values respectively.

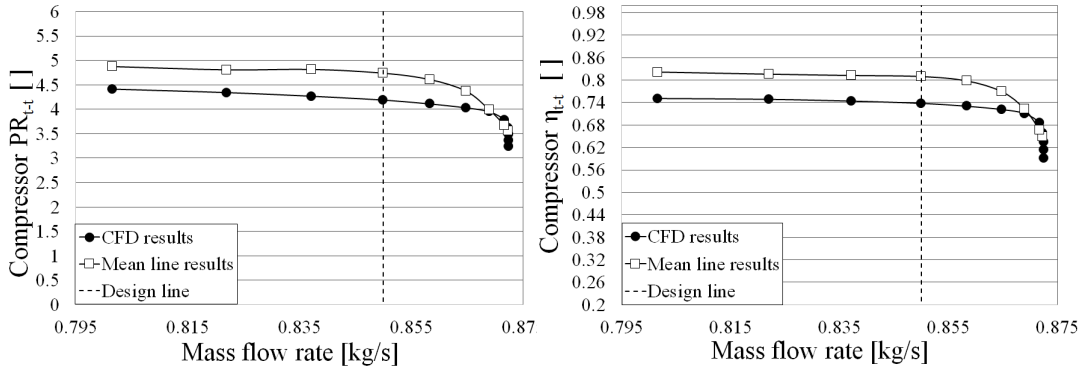

(a) (b)

Figure 3.8: a) Compressor total-to-total pressure ratio b) Compressor total-to-total isentropic efficiency

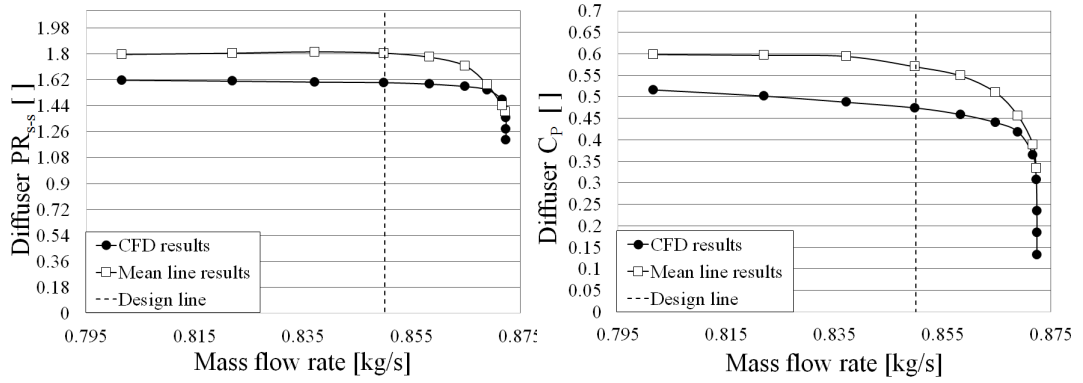

(a) (b)

Figure 3.9: a) Diffuser static-to-static pressure ratio b) Diffuser static pressure recovery coefficient

3.4 Closing remarks

The characteristic curves shown in Figures 3.8 and 3.9 show a clear deviation between the mean line results and the CFD results. The deviation is assumed to be due to the MLC not taking into account the 3-D effects that are present in the vaneless gap. A summary of the results at the design point are shown in Table 3.6. The largest difference can be seen to be for the C_P with a 23.8%. The other performance parameters have deviation under 10%. The MLDD obtained was selected as the final mean line design as it could not be further improved. However the the design was optimized later using CFD. The outlet flow angle (α_{4c}) was determined to be equal to 60°. The MLDD has a choke and stall mass flow rate of 0.872 kg/s 0.747 kg/s respectively.

Table 3.6: Parameters at design point

	$\eta_{t-t(0-4)}$	$PR_{t-t(0-4)}$	Diffuser C_P	$PR_{s-s(2-4)}$
MLC	81%	4.5	0.565	1.76
CFD	73%	4.18	0.43	1.626
Deviation	**9.8%**	**7.1%**	**23.8%**	**7.6%**

Chapter 4

Numerical analysis

4.1 Introduction

The numerical analysis of the compressor with the 1-D mean line diffuser design (MLDD) was performed with the use of the NUMECA Fine^{TM}/Turbo, AutoGrid5^{TM} and CFView^{TM} software packages. The mean line code produced a *.geomTurbo* geometry file that was imported to the AutoGrid5^{TM} automatic meshing tool which generated a mesh file (*.igg*). The meshed geometry file was imported into NUMECA Fine^{TM}/Turbo . This chapter focuses on the numerical setup of the compressor with the MLDD. The numerical setup for other cross-over diffuser (CD) geometries in this project is similar. The post processing was done with the use NUMECA CFView^{TM}.

4.2 Meshing strategy-AutoGrid5^{TM}

NUMECA AutoGrid5^{TM} is an automatic meshing tool that is used to generate meshes for various turbomachinery components. AutoGrid5^{TM} generates a main *.trb* file and a *.igg* file that is incorporated into Fine^{TM}/Turbo for the CFD simulations. Although AutoGrid5^{TM} is an automatic meshing tool it requires a significant amount of user input to generate a high quality mesh. The AutoGrid5^{TM} manual, (NUMECA International, 2014a), was used to aid in the mesh setup procedure. The meshing strategy can essentially be divided into three main sections; meridional mesh, blade-to-blade mesh, and the 3-D mesh setup. The meshing tool uses the *'Row Wizard'* function that has default blade and channel meshes for various turbo machinery. These mesh setups give the user a good base to start from. The *'Centrifugal Impeller'*, and *'Centrifugal Diffuser'* were selected for the mixed flow impeller and CD respectively.

4.2.1 Meridional mesh setup

The meridional mesh setup of the entire flow path made use of control lines to control the number of grid points upstream and downstream of the blades. The control lines are shown in Figure 4.1. The control lines are set as linear lines with *'Streamwise Number of Points'* set between 9 and 17. The control lines determine the coarseness of the grid at the inlet and outlet. The number of flow paths of both the diffuser and impeller rows are set in the *'Row Wizard'* respectively, where the *'Spanwise Grid Point Number'* (flow paths) was set to 73 and 57 for the impeller and diffuser respectively. These values indicate the numbers of meridional blade layers as illustrated by the red lines in Figure 4.1. Figure 4.1 shows that the cells close to the wall (shroud and hub) are denser, to capture the effects of the boundary layer and satisfy the y^+ condition for the flow solver.

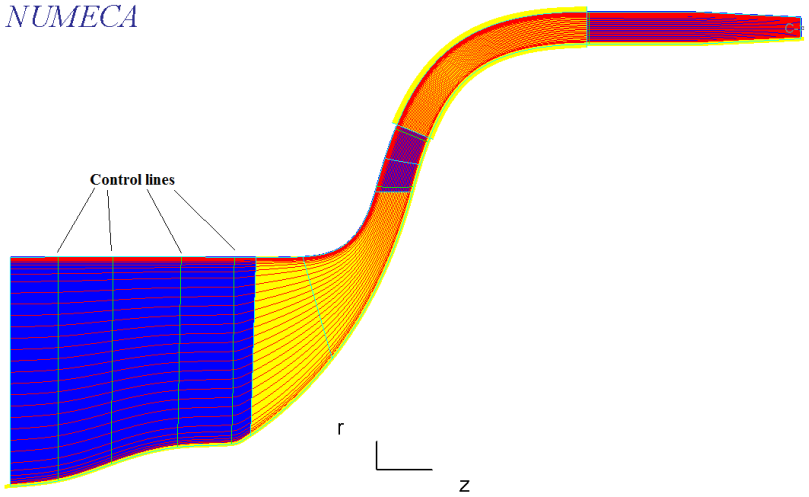

Figure 4.1: Meridional mesh view (flow path)

The *'Row Wizard'* gives the option of including a tip gap between the shroud and blades of the impeller and diffuser . The impeller shroud tip gap at the blade LE and TE was set to 0.2 mm. No fillets were enabled for the impeller or the diffuser vanes, because adding fillets would complicate the mesh and increased the computational time of the simulations (Burger, 2016).

The first cell height of both the impeller and diffuser passage walls was set to 0.0008 mm. This value was selected to ensure that the y^+ values of the cells close to the meridional passage wall falls in the range of 1-10 as required by the Spalart Allmaras Turbulence model that was used in these simulations (NUMECA International, 2014b). A y^+ value between 1 and 10 is important when solving the viscous sub-layer that is dominated by viscous effects (Versteeg and Malalasekera, 2007). A predicted y^+ value of 6 was obtained for

a wall cell height of 0.0008 mm at an average speed of 500 $m.s^{-1}$ by using Equation 4.1.

$$y^+ = \frac{y_{wall}}{6\left(\frac{V_{av}}{v}\right)^{\frac{-7}{8}}\left(\frac{L_{av}}{2}\right)^{\frac{1}{8}}} \tag{4.1}$$

4.2.2 Blade-to-blade mesh setup

Impeller

The *'H&I'* topology was enabled for the impeller main and splitter blade-to-blade mesh. *'H-Topology'* was enabled for both the main and splitter blade outlet. The main blade outlet and inlet topology type was set to *'Normal Angle'* and *'High Angle'* respectively, this simply indicates the the angle type at the outlet and inlet of the blade, an illustration can be seen in Appendix E.3. The splitter blade outlet and inlet topology type were set to *'Normal Angle '* and *'Normal Angle'* respectively. The *'Grid Skin Block'* and *'High Staggered Blade Optimisation'* for the main and splitter blades was enabled, to ensure that mesh close to the blades are small enough so that the boundary layer effect at the blade wall is fully captured, with the first cell height at the blades is set to 0.0008 mm. The *'Free Inlet'* and *'Free Outlet'* angle were enabled for the *'Clustering relaxation'* to control the span-wise angular deviation. The span-wise deviation angle is the measure of the angular variation between two adjacent cells in a 3-D mesh. The grid block for the impeller main and splitter blades are shown in Figure 4.2.

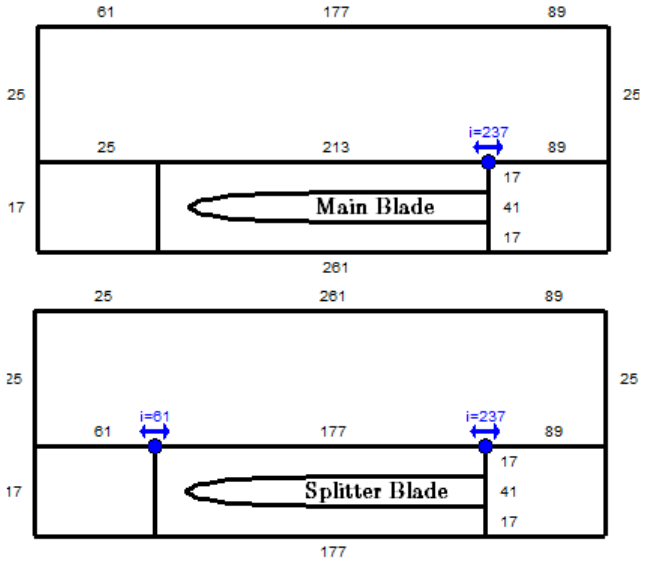

Figure 4.2: Impeller blade-to-blade grid points

Diffuser

The *'Default'* topology was enabled for the diffuser blade-to-blade mesh.*'* *Matching Periodicity'* was also enabled, to allow the diffuser blade-to-blade mesh between each period of the grid blocks to match (Figure 4.3). The *'High Staggered Blade Optimisation'* was enabled to ensure cell inflation close the wall of the diffuser vanes.

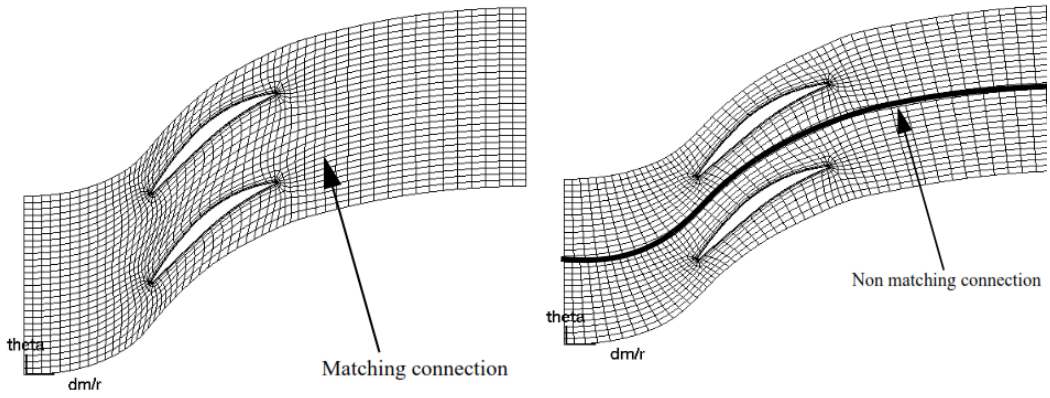

Figure 4.3: Blade-to-blade matching (NUMECA International, 2014a)

The diffuser vane outlet and inlet topology types were set to*'High Angle'* and *'Low Angle'* respectively. The cell width at the vane wall was set to 0.0008 mm to accommodate the y^+ requirement for the Spalart Allmaras turbulence model. Similar to the impeller, the *'Free Inlet Angle'* and *'Free Outlet Angle'* was enabled. The blade-to-blade mesh grid for the diffuser is illustrated in Figure 4.4.

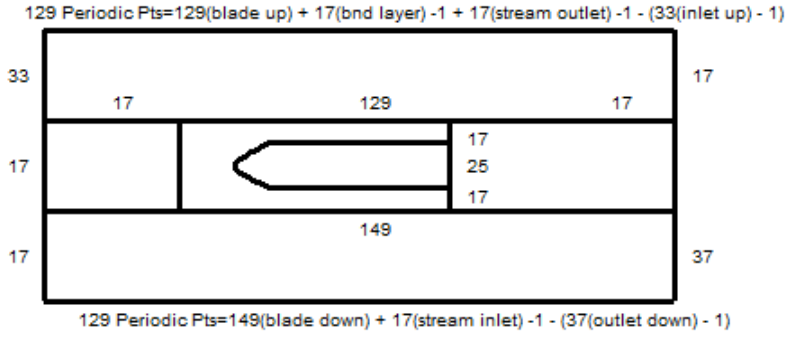

Figure 4.4: Diffuser blade-to-blade grid points

To avoid any clustering at the diffuser vane wall the *'Inlet' and 'Outlet Projection Relaxation factor'* was set to 15 and 15 respectively. A lower relaxation factor produced a clustered mesh as seen on the left of Figure 4.5 (blue circle).

An increase in the relaxation factor resulted in minimising the clustering as can be seen on the right side of Figure 4.5.

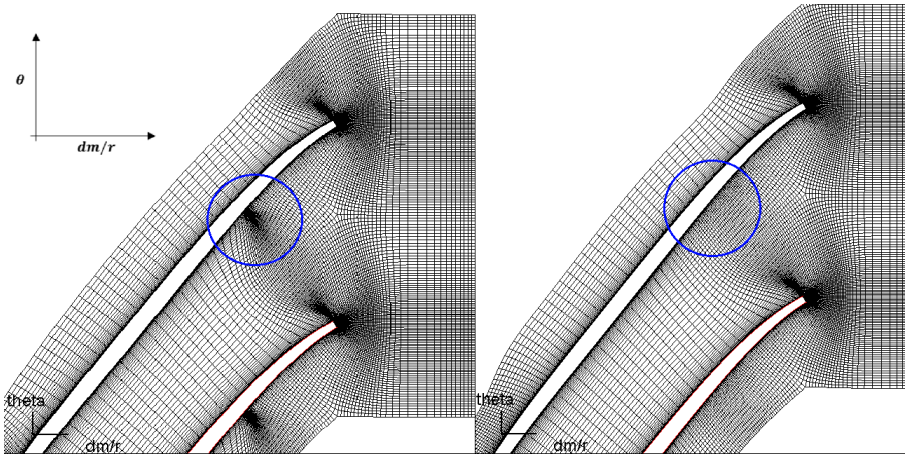

Figure 4.5: Blade-to-blade clustering diffuser

4.2.3 3-D mesh setup

The *'Optimisation Steps'* on the *'Fine Grid'* and *'Gap'* for the impeller and diffuser row were set to 600 and 500 respectively. The *'Expert'* optimisation option was enabled for both the diffuser and the impeller rows. This allows the designer to perform skewness control on the mesh. The mesh skewness was set to *'Medium'*, and the skewness control in tip gaps set to *'Full'* for the impeller row. This option allowed the mesh to be as orthogonal as possible. The *'Multigrid Acceleration'* was enable this allow a smoother 3-D mesh convergence and help minimise the expansion ratios. The *'Multisplitter Control'* was enabled for the impeller because the impeller contains splitter blades. Only *'Multigrid Acceleration'* was enabled for the diffuser row. The resulting 3-D mesh is illustrated in Figure 4.6, where the right side, Figure 4.6b, shows the periodic geometry, and the left side, Figure 4.6a, shows the mesh on the blade and hub surfaces. The impeller and diffuser have a 3-D periodicity of 9 and 20 respectively. The resulting mesh has 5.73 million grid points where 4.105 million grid points are attributed to the impeller row and 1.62 million grid points to the diffuser row.

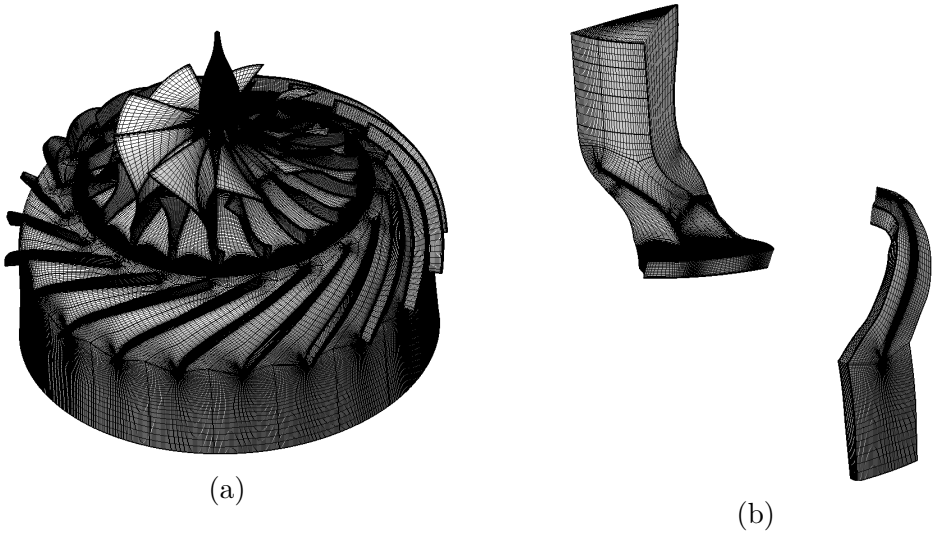

(a) (b)

Figure 4.6: Compressor 3-D Mesh

4.2.4 Mesh quality and mesh independence

To evaluate the performance of the mesh this section discusses the mesh quality and a mesh independence study of the mesh obtained from the MLDD.

Mesh quality

The mesh quality checks that were evaluated are the orthogonality, expansion ratio, aspect ratio and span-wise angular deviation angle. The mesh quality for the total mesh is summarised in Table 4.1. The mesh requirement criteria is specified by the NUMECA manual (NUMECA International, 2014b). As can be seen from Table 4.1 there are some cells that fall outside the mesh quality requirement criteria. These cells were 0.007% of the impeller nodes and 0.02% of the diffuser nodes. All low quality cells occurred due to high expansion ratio values. This however had no influence on the convergence of the simulations due to the small contribution that the low quality cells make to the entire mesh.

Table 4.1: Mesh quality final of MLDD

Quality	**Impeller**	**Diffuser**	**Mesh requirement**
Minimum orthogonality	21.934°	36.952°	>18°
Maximum expansion ratio	3.07	3.3	<2.5
Maximum aspect ratio	7874.0	1556.3	>10000
Maximum angle deviation	32.06°	18.92°	<40°
Low quality	0.0071%	0.02%	-

The y^+ values obtained for the MLDD numerical simulations at its design point are shown in Figure 4.7, where Figure 4.7b shows the refined mesh and Figure 4.7a shows the original unrefined mesh. Figure 4.7a shows y^+ values ranging from 1 to 10 while the unrefined mesh has values ranging from 1 to 22. Most of these large y^+ value cells were situated close to the TE of the impeller blades. The mesh was refined by decreasing the first cell height at the impeller main and splitter height from 0.0008 mm to 0.00062 mm.

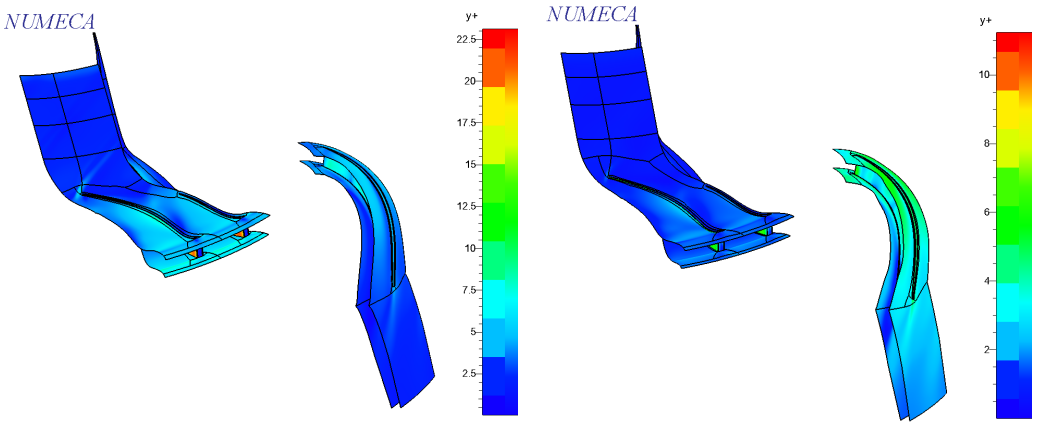

(a) (b)

Figure 4.7: 3-D y^+ values for MLDD a) Refined mesh b) Original unrefined mesh

The refined mesh showed no significant influence on the results (compressor stage total-to-total pressure ratio and total-total isentropic efficiency) obtained from the simulations, as shown in Figure 4.8a and Figure 4.8b. The refined mesh yield a 0.3% higher choke mass flow rate.

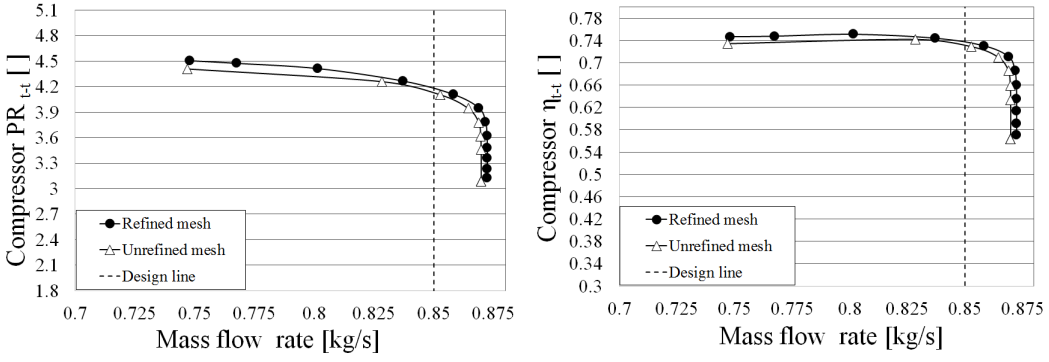

(a) (b)

Figure 4.8: a) Compressor total-to-total pressure ratio b) Compressor total-to-total isentropic efficiency

Mesh independence

A mesh independence study was performed on the MLDD simulation. The study was performed for three different grid levels, namely coarse, fine and medium. The mesh quality and grid size for the coarse and fine grid is shown in Appendix E.1.1. The compressor stage total-to-total pressure ratio, $PR_{t-t(0-4)}$ and total-to-total isentropic efficiency, $\eta_{t-t(0-4)}$ performance values for the different grid levels are compared in Figure 4.9a and Figure 4.9b. As can be seen there is no clear difference between the values obtained from different grid levels for $PR_{t-t(0-4)}$. However, the $\eta_{t-t(0-4)}$ performance curve show that the coarse grid yielded values 2.3% larger than the fine and medium grid. There are also small differences in the choke mass flow rates for the three grid levels with the coarse grid, medium grid and fine grid having choke mass flows of 0.8691 kg/s, 0.8724 kg/s, 0.8725 kg/s respectively. Due the small difference between medium and fine mesh a conclusion can be made that refining the mesh further would yield no significant change in the values, thus making the mesh used for this study appropriate.

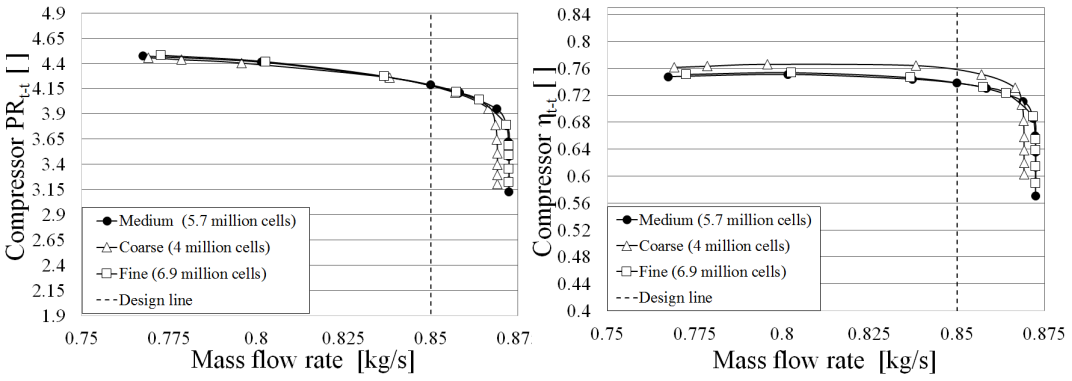

(a) (b)

Figure 4.9: a) Compressor total-to-total pressure ratio b) Compressor total-to-total isentropic efficiency

4.3 Fine^{TM}/Turbo simulation setup

NUMECA Fine^{TM}/Turbo was used For the numerical simulations. This section discusses the numerical setup of the MLDD simulations. The fluid flow model, the boundary conditions and the computational model is discussed.

4.3.1 Fluid flow model

Air was selected as the working fluid. The air was set as a perfect gas. Selecting air as a real gas increases computational time by 25% (NUMECA International, 2014b). To validate this, a study was conducted to evaluate the difference in

the results obtained from using air as a real gas versus using it as a perfect gas, these results at design point are tabulated in Table 4.2. As can be seen from Table 4.2 there the differences in the performance results obtained from the two gas types are very small (0.9%). However the time to complete one simulation increased from 1.5 hours to 2 hours by using air as a real gas. Although using air as a real gas according to literature would give more accurate results the accuracy level does not justify the 25% increase in computational time, especially during the optimisation process where large quantity of simulation will be performed.

Table 4.2: Fluid model type at design point

Gas type	$\eta_{t-t(0-4)}$	$PR_{t-t(0-4)}$	C_P	$PR_{s-s(0-2)}$
Perfect gas	73.8%	4.18	0.43	1.626
Real gas	74.5%	4.19	0.429	1.626
Deviation	**0.939%**	**0.238%**	**0.23%**	**0%**

The properties of the perfect gas are provided in Table 4.3, where the dynamic viscosity of the air changes with temperature (Sutherland's law).

Table 4.3: Fluid properties

Properties	**Definition**
Specific heat (C_p)	1006 $J/kg \cdot K$
Heat capacity ratio (γ)	1.4
Prandtl number	0.708
Dynamic viscosity (at 293.11 K)	1.716×10^{-5} $Pa \cdot s$
Sutherland Temperature	$110.555K$

The time configurations were set as steady state using the Spalart Allmaras turbulence model. The Spalart Allmaras turbulence model is very robust and is able to solve complex flow problems. This model is considered economical for computations in boundary layers for external flows (Versteeg and Malalasekera, 2007).

To validate the feasibility Spalart Allmaras turbulence model, a turbulence model independence study was performed. Two additional turbulence models were evaluated, The first is the Shear Stress Transport (SST($k-\omega$)) turbulence model (with extended wall functions) and the second is the k-epsilon turbulence model (with extended wall functions). The $k-\epsilon$ turbulence model was used because its the most widely used and validated turbulence model (Versteeg and Malalasekera, 2007). Additionally to this, the reason the $k-\epsilon$ turbulence model was used was due the flow performing well for confined flows.

However the model does have some disadvantages due to its poor performance for rotating and swirling flows. The $k-\epsilon$ also has unsatisfactory performance for boundary layers with adverse pressure gradient (Menter, 1992). The SST model was used due to its ability to perform well in the boundary layer region (near-wall). The SST turbulence model is a hybrid model that uses both the $k-\epsilon$ and $k-\omega$ model where the $k-\epsilon$ is used in the fully turbulent region far from the wall and the near wall region uses the $k-\omega$ turbulence model (Menter, 1992).

The inlet k an ϵ values at the inlet boundary for both the SST and $k-\epsilon$ turbulence model was kept as default ($k = 5\ m^2/s^2$, $\epsilon = 3000\ m^2/s^3$). However a study was performed to evaluate the sensitivity of the solutions by varying these inlet conditions. The equations to calculate k and ϵ was obtained from Versteeg and Malalasekera (2007), and is determined from Equations 4.2, 4.3 and 4.4.

$$k = \frac{2(U_{ref}T_i)}{3} \tag{4.2}$$

$$\epsilon = {C_\mu}^{3/4}\frac{k^{3/2}}{l} \tag{4.3}$$

$$l = 0.07L \tag{4.4}$$

The study was done for both the SST and the $k-\epsilon$ turbulence models. The turbulence intensity, T_i was set to 2.5%, 5% and 7.5%. The reference velocity, U_{ref} was set as 129 m/s, obtained from the inlet 10 kPa dynamic pressure head evaluated from a Spalart Allmaras model simulation. The results for the SST simulations are tabulated in Table 4.4. The results in Table 4.4 show that the initial k and ϵ values are appropriate and that the solution is not sensitive to the change in turbulence intensity. The results for the $k-\epsilon$ turbulence model are shown in Figure 4.5. Similar to the results obtained from the SST turbulence model, the results for the $k-\epsilon$ turbulence model show there is no significant effect on the results with a change in turbulence intensity.

Table 4.4: Inlet conditions for SST turbulence model

T_i	$k\ [m^2/s^2]$	$\epsilon\ [m^2/s^3]$	$\dot{m}\ [kg/s]$	PR_{t-t}	η_{t-t}
-	**5**	**30000**	**0.8567**	**4.110**	**0.751**
0.025	6.934	772.22	0.8564	4.1098	0.751
0.05	27.735	6177.79	0.8544	4.112	0.750
0.075	62.404	20850	0.8554	4.111	0.750

Table 4.5: Inlet conditions for $k - \epsilon$ turbulence model

T_i	$k\ [m^2/s^2]$	$\epsilon\ [m^2/s^3]$	$\dot{m}\ [kg/s]$	PR_{t-t}	η_{t-t}
-	**5**	**30000**	**0.865**	**4.089**	**0.733**
0.025	6.934	772.22	0.864	4.088	0.733
0.05	27.735	6177.79	0.862	4.086	0.731
0.075	62.404	20850	0.860	4.085	0.730

The $PR_{t-t(0-4)}$ and $\eta_{t-t(0-4)}$ characteristic curves for the different turbulence models are shown in Figure 4.10a and Figure 4.10b respectively.

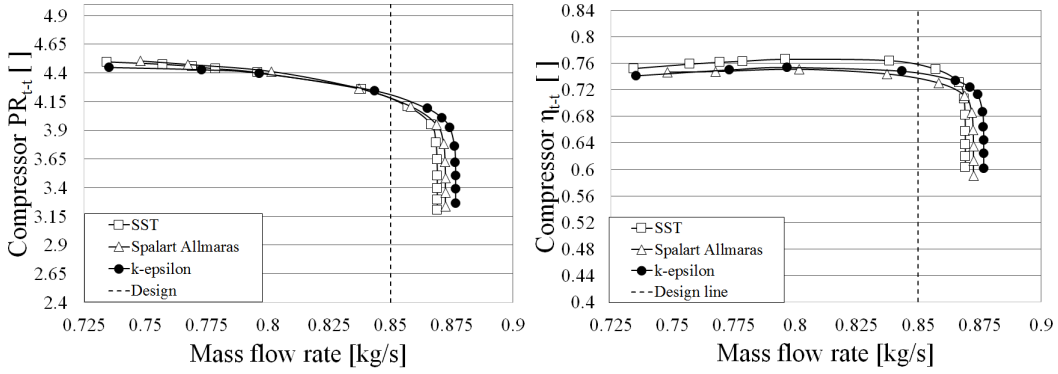

(a) (b)

Figure 4.10: a) Compressor total-to-total pressure ratio b) Compressor total-to-total isentropic efficiency

As can be seen from Figure 4.10 the three turbulence models correlate well with each other. Therefore the Spalart Allmaras turbulent model is considered an appropriate model for the simulation. The reasons for selecting the Spalart Allmaras Turbulence model was due to its ability to run simulations that have good performance compared to the SST turbulence model with a much smaller computational memory requirement. It is also a good turbulence model due to its suitability for airfoil applications and for this reason that it has become a popular type of turbulence model for turbo machinery (Versteeg and Malalasekera, 2007).

4.3.2 Boundary conditions

This section discusses the compressor boundary conditions of the computational setup . These include inlet, outlet, solid and rotor stator interface boundary conditions. Figure 4.11 shows the computational domain, showing the boundary flow patches. The characteristic length and velocity was set as 55.5 mm and 552 m/s corresponding to the impeller outside diameter and blade tip velocity (U_2) at the impeller design speed of 95000 rpm.

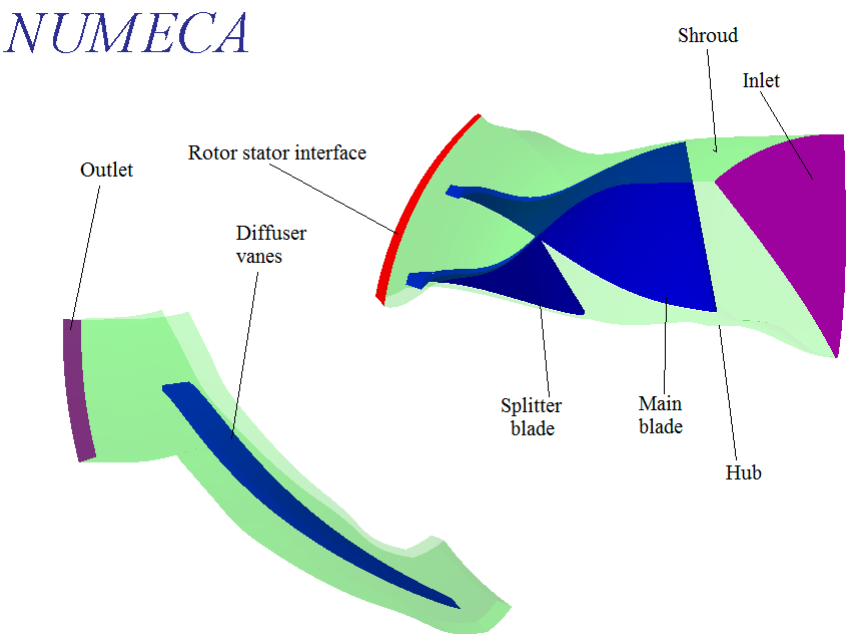

Figure 4.11: Computational domain

Inlet

The inlet boundary conditions for the computational domain is tabulated in Table 4.6. The inlet boundary is specified as a *'Total Quantities Imposed'* boundary, with *'Velocity direction (V extrapolated)'* enabled. As can be seen from Table 4.6 there is no inlet whirl or radial component meaning the inlet flow is axial.

Table 4.6: Inlet boundary conditions

$V_r/\|V\|$	0
$V_t/\|V\|$	0
$V_z/\|V\|$	1
Absolute total pressure (P_{01})	100000 Pa
Absolute total temperature (T_{01})	293 K
Turbulent viscosity (ν_t)	0.0001 m^2s^{-1}

Outlet

The outlet boundary conditions were set as a *'Averaged Static Pressure'* imposed boundary. The outlet static pressure was varied from 140 kPa (choke point) to 440 kPa (stall point) resulting in different mass flow rates. The stall point was obtained by checking at which outlet static pressure the CFD solver breaks down and gives unstable results.

Solid

The solid boundary conditions for the impeller were set separately, where the impeller hub was set as *'Area Defined Rotational Speed'*. The hub settings are tabulated in Table 4.7.

Table 4.7: Impeller hub boundary conditions

Rotational speed 1	0 rpm
Rotational speed 2	95000 rpm
Lower radius limit	0 mm
Higher radius limit	55.5 mm
Lower axial limit	-40 mm
Higher axial limit	40 mm

The remaining solid walls were set to constant rotation with the settings tabulated in Table 4.8.

Table 4.8: Solid boundary conditions

Row	**Group**	**Rotational Speed**
Impeller	Blade	95000 rpm
Impeller	Shroud	0 rpm
Diffuser	Blade	0 rpm
Diffuser	Shroud	0 rpm
Diffuser	Hub	0 rpm

Rotor stator interface

The rotor stator interface serves as a linking mechanism to connect the impeller and diffuser grid rows. The position of the rotor stator interface can be seen in Figure 4.11. The rotor stator interface was set as a *'Conservative Coupling by Pithcwise Row'* this type of coupling is recommended due to its potential to maintain exact conservation of mass flow, momentum and energy through the interface (NUMECA International, 2014b).

4.3.3 Computational setup

The *'Initial solution settings'* were performed by setting the *'Estimated static pressure'* at the inlet boundary to 90 kPa and the *'Estimated static pressure'* at the rotor stator interface was set to 200 kPa. The number of iterations was

set to 4000 with the output files saved after every 200 iterations. The solver was set to single precision. The required memory was calculated to be 370.08 MB. The resultant solution converged after 1000 iterations. The mass-flow convergence graph generated is shown in Figure 4.12.

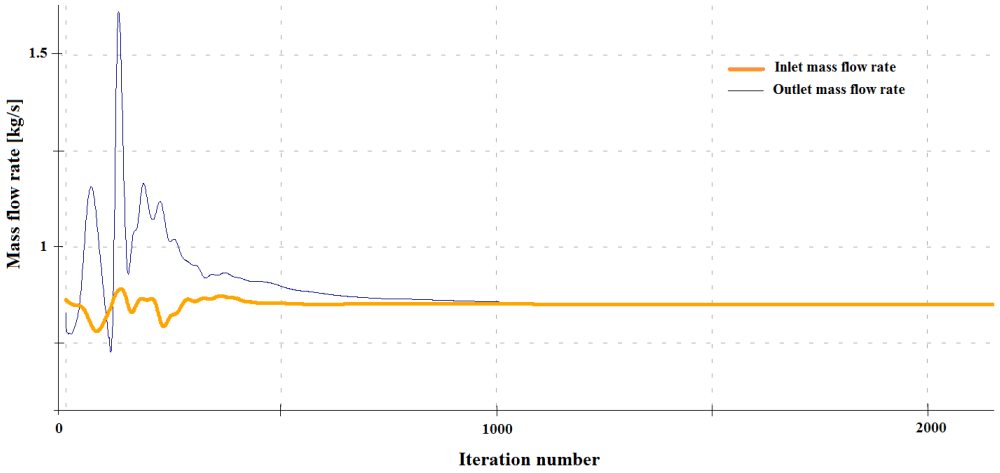

Figure 4.12: Mass flow convergence

4.3.4 Closing remarks

The numerical analysis for the MLDD was done to ensure that there is correlation between the mean line results and the CFD results for the MLDD. The numerical analysis for other geometries performed for this research project followed the same process.

Chapter 5

Optimisation

5.1 Introduction

The final step in the design process was to do a numerical optimisation with the use of NUMECA Design3D^{TM} software. Figure 5.1 shows an illustration of the flow chart for the optimisation process. The first optimisation step was to create a parametric model of the mean line diffuser design (MLDD) designed in Chapter 3. The second step was to do a database generation for use in the optimisation. The final step is to do the actual optimisation. The mesh template used in this chapter is the same as the mesh template generated in Chapter 4.

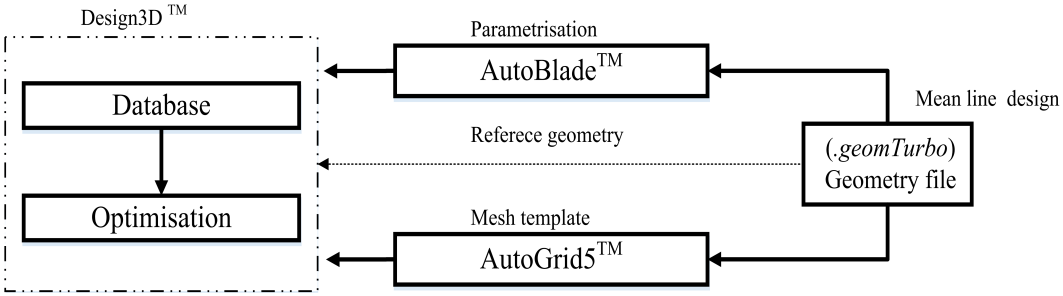

Figure 5.1: Optimisation process

A multi-point optimisation was performed at three different points, namely the stall, design, and choke mass flow rate. Figure 5.2 illustrates a characteristic curve depicting the three optimisation points. The stall point was found to be at an exit static pressure of 440 kPa, the design point at an outlet static pressure of 360 kPa and the outlet static pressure at the choke point was 140 kPa. These static pressure points are set in the outlet boundary conditions as discussed in section 4.3.2. However it is important to note that the stall, and choke points used are not the actual stall and choke points, it is only the points the numerical simulation predicts.

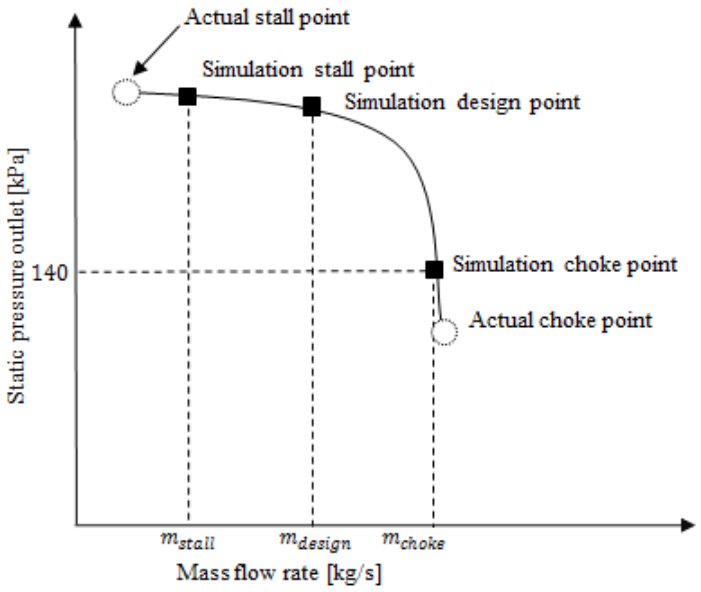

Figure 5.2: Three point optimisation

5.2 Parametric model

The MLDD was parametrised using the NUMECA AutoBlade^{TM} software package. The parametric model provides an approximate geometry of the MLDD. This approximate model defines the geometry by means of parameters that can be used at a later stage in the database generation and the optimisation phase. Although optimisation would only be performed on the diffuser vanes the entire compressor meridional passage was parameterised.

5.2.1 Meridional contours 'End walls'

The meridional passage describes the hub and shroud contours. Composite curves were selected for the hub and the shroud. This option allows the meridional passage curves to be described with various curve types.

Three C-splines were used to parametrise the impeller hub meridional passage curve where the three C-splines curves were given five, nine and nine control points respectively. The diffuser hub meridional passage curve was set as a Bezier curve type to parametrise it. The Bezier curve was given 4 control points as can be seen from Figure 5.3 (HUB_25 to HUB_28). The reason for using a Bezier curve type to parametrise the diffuser hub meridional passage curve is because Bezier points can easily be varied to change the curve of a geometry. The hub meridional passage outlet was given two straight lines, one for the straight section and one for the pinched outlet section.

The impeller shroud meridional passage curve was given a straight line, and a C-spline to parametrise it where the C-spline was given 10 control points. The diffuser shroud meridional passage curve was set as a Bezier curve with 4 control points (SHROUD_11 to SHROUD_14) to parametrise it. The outlet meridional passage section, at the diffuser discharge, was given two straight lines i.e one for the axial flow channel and the other for the pinched outlet.

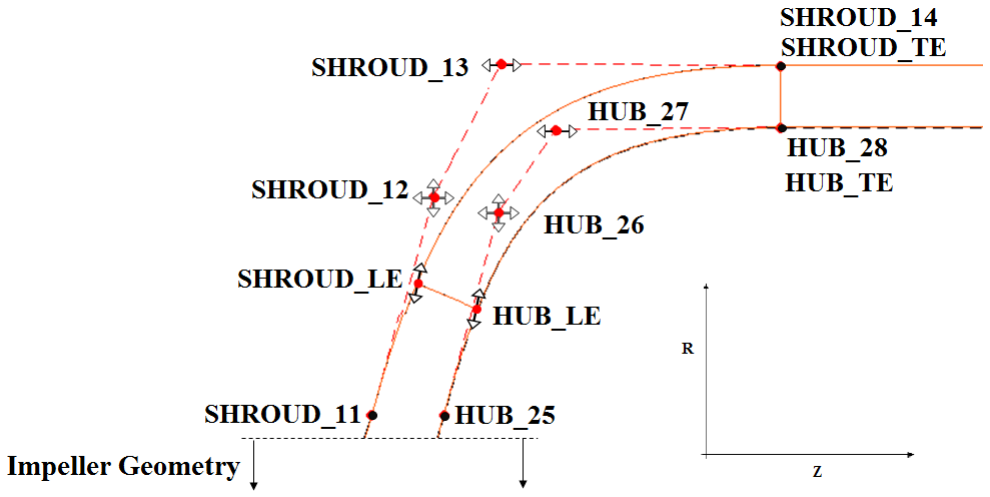

Figure 5.3: Meridional view parametrisation

5.2.2 Stream surfaces

The stream surfaces describe the meridional traces. For the *'Surface setup'* the *'Hub to shroud direction interpolation'* was selected as the stream surface type. This allows the stream surfaces to follow the profile of the hub and the shroud meridional passage curves. *'Rulings'* are activated to ensure that the diffuser geometry are constructed by ruled surfaces. Ruled surfaces are surfaces that can be generated entirely by the use of straight lines. This is beneficial for manufacturing the geometry with 5 axis milling. The primary stream surfaces are selected at the hub with a span-wise location of -1.05% and the shroud with a span-wise location of 101.05%.

5.2.3 Stacking laws

The stacking laws describes the blade positioning and the stacking of the blade to form the 3-D blade geometry. The *'Stacking point'* describes the reference point of the blade from which stacking will take place and it was set as the leading edge (LE) of the diffuser vane. The *'Meridional location law'* option describes the variation of the LE of the blade from hub to shroud. The variation was set to linear and this ensured a straight line LE spanning from hub to shroud. The *'Meridional location law'* also allowed the designer to

select which coordinate (R or Z) should describe the LE and trailing edge (TE) points on the hub and shroud, the coordinates for the TE and LE were both set to the radius, R for both the hub and shroud. The tangential variation of the LE was set to linear, defining the LE and TE as a straight lines spanning from hub to shroud.

5.2.4 Main blade

This section allows the designer to parametrise the diffuser vane geometry. The main vane construction plane was set as $dm/r, \theta$. The blade camber was given a Bezier curve type with the number of control points set to 5, as shown Figure 5.4, for both the hub and the shroud section. The distribution of the camber curve was set to uniform. The *'Side curves'* represent the thickness distribution on the camber curve. The thickness addition was set to symmetric. The pressure and suction side curves for the vanes were set to Bezier curves with 6 control points. This was done for the hub and shroud section. The TE and LE of the blade was set to blunt and rounded respectively.

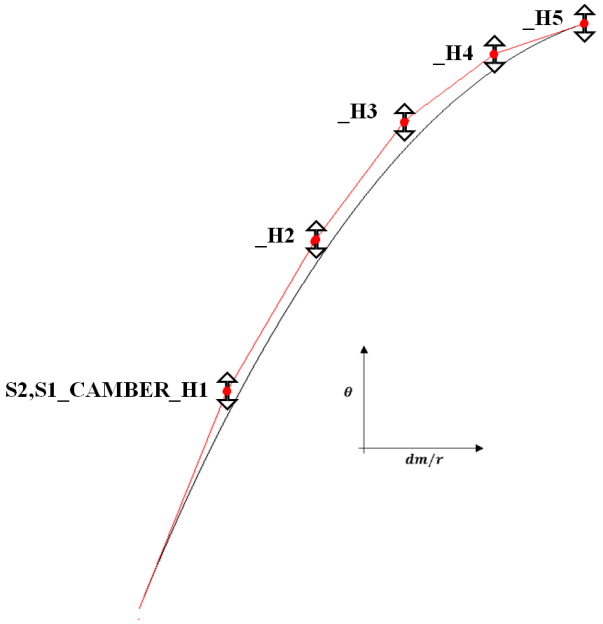

Figure 5.4: Diffuser vane parametrisation

5.2.5 Fitting control

The fitting control assists in obtaining a parametric model that is close to the target MLDD geometry. The first step in fitting control is adapting the parametric model to be as close to the mean line design target. The adapting step gives the designer the opportunity to visually inspect the model to investigate

whether the model curve types are suitable for the target geometry. The designer can change the number of control point that describe the curves if the current number of control points are insufficient. This adaptation is however not a very good final model calculator.

After the model had been adapted to the target geometry, the user can freeze some control points, such as the control points at the channel outlet where the position of the control points are known. The model was fitted with the optimisation accuracy set as Fine, fitting all the features such as, hub and shroud curves, blade thickness, camber curve and leading and trailing edges.

5.3 Parameter bounds

The final fitted model was used to set the bounds of the parametric model. These bounds were used in the database generation and optimisation steps. The parameters that were frozen were the impeller hub and shroud curves (see Appendix F). For the diffuser geometry the first Bezier control point of the hub (HUB_Z25, HUB_R25) and the shroud (SHROUD_Z11, SHROUD_R11) was frozen to ensure that the hub and shroud meridional curve of the impeller does not change. The *'Slope continuity'* was enabled to ensure no slope discontinuity between the impeller and diffuser meridional hub and shroud curves. The radius components of hub and shroud points, HUB_R27 and SHROUD_R13, as can be seen from Figure 5.3, were frozen to ensure that the meridional passage outlet remained axial. The Bezier control points that describes the camber thickness were frozen except for the point that defines the camber thickness at the TE of the vane. The free parameters are listed in Table 5.1.

The bounds for the free parameters were set after numerous adjustments were made to ensure no impractical geometries can be obtained. Examples of unacceptable geometries are shown in Figure 5.5.

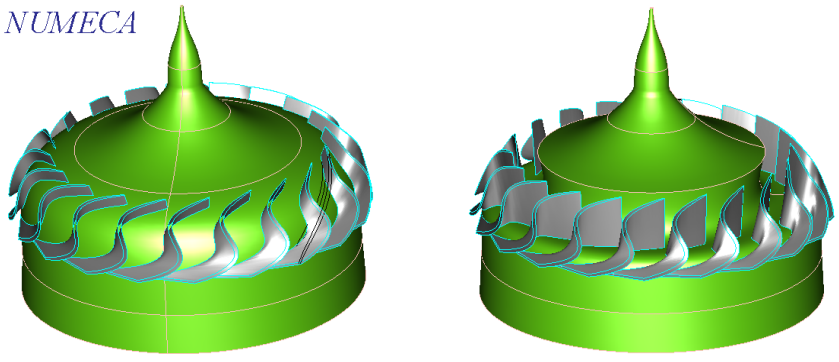

Figure 5.5: Unacceptable geometries

The geometry bounds for the upper and lower limits are listed in Table 5.1

Table 5.1: Free parameter list

Name	Lower bound	Value	Upper bound
HUB_Z26	39.885	42.516	44.886
HUB_R26	73.332	73.332	83.000
HUB_Z27	45.520	46.113	65.521
S1_CAMBER_H1	0.160	0.255	0.400
S1_CAMBER_H2	0.320	0.430	0.430
S1_CAMBER_H3	0.470	0.621	0.720
S1_CAMBER_H4	0.620	0.725	0.780
S1_CAMBER_H5	0.700	0.777	0.785
S1_HALF_THICKNESS_P5	1E-009	0.559	0.559
S2_CAMBER_H1	0.160	0.269	0.350
S2_CAMBER_H2	0.320	0.429	0.550
S2_CAMBER_H3	0.470	0.567	0.600
S2_CAMBER_H4	0.630	0.726	0.780
S2_CAMBER_H5	0.740	0.776	0.790
R_LE_HUB	58.000	65.5560	65.556
DETE	0.000	2.467	2.467

Minimising the number of free parameters will reduce computational time. A method that can be used to minimise the parameters is to find relationships between these free parameters. The first relationship was to ensure that the channel height remained constant, thus relating the shroud and hub Bezier control points to each other. This is shown in Table 5.2 (see SHROUD_Z12, SHROUD_R12 and SHROUD_Z13). The vane TE thickness at the shroud was set equal to the vane TE thickness at the hub to ensure uniform thickness throughout the TE during the database generation and optimisation. The diffuser LE radius at the shroud was set equal to the sum of the LE radius at the hub and the parameter DETE, which is a user defined parameter given in Table 5.1. This ensures that the LE varies from an angle normal to the passage curvature to an angle that is parallel to the impeller TE. This is explained further in section 5.6. These dependant parameters are listed in Table 5.2.

Table 5.2: Dependant parameter list

Name	Expression	Value
SHROUD_Z12	HUB_Z26 - (40.886-34.443)	36.073
SHROUD_R12	(76.471-73.960)+ HUB_R26	75.842
SHROUD_Z13	HUB_Z27-(46.113-41.149)	41.149
S2_HALF_THICKNESS_P5	S1_HALF_THICKNESS_P5	0.559
R_LE_SHROUD	R_LE_HUB+DETE	68.023

A sample of the possible meridional and CD vane geometries that can be obtained are shown in Appendix G.

5.4 Database generation

The most important step for optimisation is the database generation as it serves as the initial point for the optimisation process. The database generation reduces the computational time needed for the optimisation process (NUMECA International, 2014c). The database is incorporated into an Artificial Neural Network (ANN), which is discussed in section 5.5.1.

5.4.1 Parametric model and mesh generation

The first database that was created was set to generate 55 samples at the design, choke and stall point. The parametric model discussed in section 5.3 was incorporated into the database generator. The parameters given in Table 5.1 and 5.2 were used to generate the 55 random geometry samples. The initial mesh setup template file (*.trb* file), was used to generate the meshes for the 55 random geometries. The reference *.geomTurbo* file which contains the impeller geometry was imported into Design3D™.

The mesh qualities that were obtained from the samples were expected to adhere to the criteria proposed by Diener (2016) allowing the solution of each sample to be considered accurate . The criteria are as follows; the skewness was required to be greater than 18° and the expansion ratio was proposed to be less than 4. The aspect ratio was also evaluated, to be less than 10000. The final quality criterion was the angle deviation that needed to be kept lower than 40°. The quality of the database obtained yielded mesh qualities that had an orthogonality that is lower than 18° for 21 of the 55 samples. The other criteria were all satisfied with all the samples falling in the required range. The low quality orthogonality necessitated the author to create a new mesh template. The template was altered by setting the diffuser topology *'Outlet Type'* from *'High'* to *'Normal'*. The new mesh template was then incorporated into the database. The number of samples were also increased to allow the

designer to delete bad mesh quality samples without decreasing the total number of samples significantly. The resultant mesh qualities from the databases are shown in Table 5.3. As can be seen from the table the second database proved to have a much higher percentage of good mesh quality cells with only 4% having low orthogonality cells.

Table 5.3: Mesh quality database

	Database1	**Database2**
Number of samples	55	75
with orthogonality<18°	21(38%)	3(4%)
with expansion ratio>4	0%	0%
with aspect ratio>10000	0%	0%
with angle deviation>40°	0%	0%

5.4.2 Numerical model

Each geometry sample would be run for three different computations, namely stall, design and choke. The numerical setup for the three points are set in section 4.3. The three optimisation points were determined to be at three different outlet static pressure as mentioned in section 5.1. These three points were however determined for the MLDD. Although a different geometry may have different stall and choke mass flow rates these points were kept the same throughout the database generation.

5.4.3 Post processing

Post processing is an important part of the database generation as it is responsible for determining the flow conditions and performance parameters that will be used in the optimisation step. The important compressor design quantities are the compressor, total-to-total isentropic efficiency, $\eta_{t-t(0-4)}$ and, total-to-total pressure ratio, $PR_{t-t(0-4)}$, determined from Equations 5.1, 5.2 respectively.

$$\eta_{t-t(0-4)} = \frac{T_{01}((\frac{P_{04}}{P_{01}})^{\frac{\gamma-1}{\gamma}} - 1)}{T_{04} - T_{01}} \tag{5.1}$$

$$PR_{t-t(0-4)} = \frac{P_04}{P_{01}} \tag{5.2}$$

The important quantity for measuring diffuser performance is the static pressure recovery coefficient, C_P value and it is determined from Equation 5.3. The compressor total-to-static pressure ratio, $PR_{t-s(0-4)}$, can also be used as a performance indicator to show the increase in static pressure across the

compressor, as depicted by Equation 5.4.

$$C_P = \frac{P_4 - P_2}{P_{02} - P_2} \tag{5.3}$$

$$PR_{t-s(0-4)} = \frac{P_4}{P_{01}} \tag{5.4}$$

The flow angle calculated with Equation 5.5 can also be used as a performance indicator.

$$\alpha_{4c} = tan^{-1}\left(\frac{C_{04}}{C_{m4}}\right) \tag{5.5}$$

St was used to indicate the operational stability of the compressor, as shown by Equation 2.1:

$$St = \frac{PR_{t-t(stall)} - PR_{t-t(design)}}{\dot{m}_{stall} - \dot{m}_{design}} \tag{5.6}$$

DC is used to measure the difference in $\eta_{t-t(0-4)}$ at the design and choke point. This is given by Equation 5.7.

$$DC = \eta_{t-t(design)} - \eta_{t-t(choke)} \tag{5.7}$$

5.5 Optimisation

After the database has been created the next step in the optimisations process was to perform the actual optimisation with the use of NUMECA Design3D^{TM}. The single objective optimisation was selected with the Genetic Algorithm (GA) selected as the method of optimisation. 70 design iterations was enabled. The GA makes use of a ANN to approximate a surrogate function.

5.5.1 Artificial neural network

To perform CFD computations for every possible geometry when optimising would be very computationally expensive. It is for this reason that a function is approximated in terms of the CFD results and the geometric parameters. These geometrical parameters and CFD results are obtained from the database generation process discussed in section 5.4. The approximated function is generated with an ANN, where the input of the ANN is the free geometric parameters discussed in section 5.3. The ANN outputs are the computational quantities that were selected by the user. This includes the derived quantities discussed in section 5.4.3. The Neural Network Learning parameters that are used in the NUMECA optimiser are provided in Table 5.4.

Table 5.4: ANN parameter settings

Parameter	value
Number of iterations	10000
Learning rate coefficient	0.5
Momentum coefficient	0.8
Decay factor	0.0
Convergence level	0.01

5.5.2 Genetic algorithm

The GA is a single objective selection optimisation algorithm that is inspired by biological evolution operators such as mutations and natural selection. GAs are basically divided into five steps/phases. The algorithm starts off with an initial population and a set of randomly selected states. For this research the initial population is a set of random geometries and the states are the geometric parameters. The algorithm then uses a fitness function that is a set of objective functions to select the best possible population and delete the other geometries with bad fitness ("survival of the fittest"). The next phase is to randomly start crossing over states of populations with one another and evaluating the fitnesses. It might be possible to have one population crossing over with multiple other populations. The last phase in the algorithm is then to perform mutation on the population by changing each state in a population and evaluating the fitness of the objective function.

The evolution settings in NUMECA Design3D^{TM} are shown in Table 5.5. The population size refers to the number of children per cycle during the process. The truncated rate determines the size of samples that is allowed to reproduce. The extrapolation range determines the modification amplitude between children and parent: If it is set to 1 it means that the parameter values between parent and child will not be random and will be close to the best parent values but not the same . The precision coefficient controls the mutation amplitude, where the coefficient is given by $2^{-k\alpha}$ with k being the precision coefficient. The reproduction cycle size refers to the number of times the population would reproduce. The elitism parameter determines the number of parents that are directly transmitted (without cross over) to the next generation. The search interval determines the amplitude range of the mutation.

Table 5.5: GA parameter settings

Parameter	value
Population size	50
Truncation rate	20
Extrapolation range	1
Precision coefficient	16
Reproduction cycle size	50
Elitism	1
Search Interval	0

5.5.3 Objective function

The objective function is used to measure the quality (fitness) of the optimised solution. A penalty is computed for the CFD results and geometrical quantities. The penalty is a scaled difference from the desired results (NUMECA International, 2014c). Due to the GA being a single objective optimisation process, the objective function is just a summation of the penalty terms. The penalties are calculated using Equation 5.8

$$P = W\left(\frac{Q_{imp} - Q}{Q_{ref}}\right)^k \tag{5.8}$$

W is the weighted factor which allows the designer to scale the penalty term up or down. Q_{imp}, Q, and Q_{ref} is the imposed quantity, computed quantity and the reference quantity respectively, used to non-dimensionalise the penalty term. k is the exponent of the penalty term, this value is usually 2.

The objective function is established by setting the imposed quantity (Q_{imp}) values. These imposed values are listed in Table 5.6. At the design point it was required that the $\eta_{t-t(0-4)}$ be as close to unity as possible. It was also required that the $\eta_{t-t(0-4)}$ of the design point must be greater than that of the choke point. After inspecting the database it was found that the maximum design point $PR_{t-t(0-4)}$ was 4.5. The design point $PR_{t-t(0-4)}$ was therefore required to be greater than 4.5. For stability the difference between the stall and design point $PR_{t-t(0-4)}$ was required to be less than 0, indicating a negative slope that represents stable compressor operation (Japikse and Baines, 1997). The design mass flow rate was required to be as close to 0.85 kg/s as possible. The choke mass flow rate was required to be greater than 0.85 kg/s so that the compressor won't operate at choke mass flow rate. There was however no reason to maximise the choke mass flow rate as the impeller already limits this quantity. For good measure the design point $PR_{t-s(0-4)}$ was required to be greater than 4 (largest value in database). To maximise the axial flow angle at the diffuser exit (α_{4c}), α_{4c} was required to be greater than 60°(obtained from

the MLDD) but less than 90°. The final and the most important quantity is the diffuser $C_{P(2-4)}$, which was required to be as close to unity as possible.

Table 5.6: Imposed quantities for the objective function

	Imposed values				
Quantity	Stall(S)	Design(D)	Choke(C)	D-C	S-D
$\eta_{t-t(0-4)}$	-	=1	-	-	<0
$PR_{t-t(0-4)}$	-	>4.5	-	<0	-
$PR_{t-s(0-4)}$	-	>4	-	-	-
$\dot{m}$ $[kg/s]$		=0.85	<0.85	-	-
$\alpha_{4c}[°]$	-	>60	-	-	-
$C_{P(2-4)}$	-	=1	-	-	-

5.6 Optimised design

The optimisation process converged after 25 iterations. The Stellenbosch university High Performance Computer (HPC) was used to generate the data base using 33 CPU cores. The time to complete the data base was approximately 4 days (75 samples) compared to using a 4 core core CPU that took 21 days to generate. The optimisation converged after 4 days (30 design iterations), however the time remained constant whether the HPC was used or the 4 core CPU. Figure 5.6 show an illustration of the convergence. The optimisation solution was assumed to be converged when the ANN solution was close to the CFD solution of the current design.

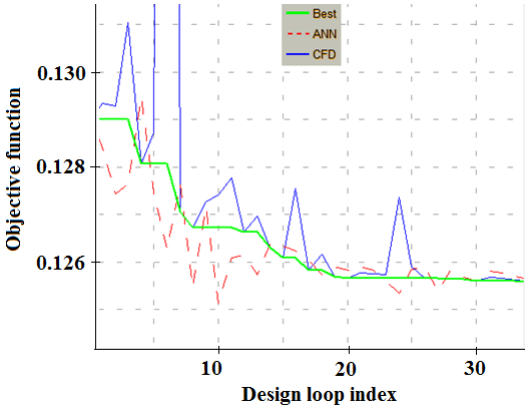

Figure 5.6: Optimisation convergence

The resultant optimised geometry compared to the mean line geometry is shown in Figures 5.7 and 5.8. As can be seen from Figure 5.7 the meridional passage shows a sharp turn with the LE of the diffuser vane significantly closer

to the TE of the impeller. However there is no slope discontinuity between the impeller and diffuser meridional curve as it was set in section 5.3.

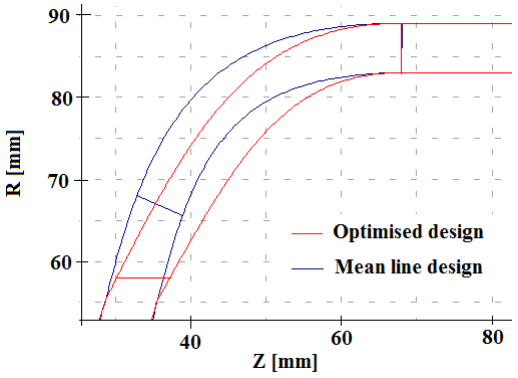

Figure 5.7: Meridional geometry with vane leading and trailing edges

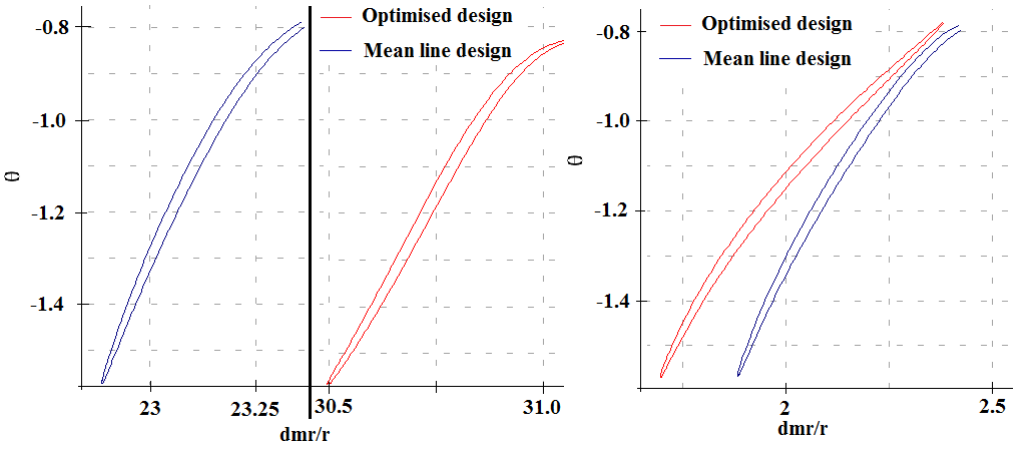

(a) (b)

Figure 5.8: a) Hub vane profile b) Shroud vane profile

It was discovered that for the same vaneless gap radius radius (r_3/r_2) the diffuser with a LE normal to the meridional passage curvature, had a much larger recirculation bubble compared to a diffuser with a LE that is parallel with the impeller TE. Figure 5.9 shows the MLDD, optimised diffuser design (ODD) with LE (LE1) perpendicular to meridional passage flow and the ODD with LE (LE2) parallel to impeller TE . Figure 5.9 clearly shows a decrease in recirculation bubble size from LE1 to LE2.

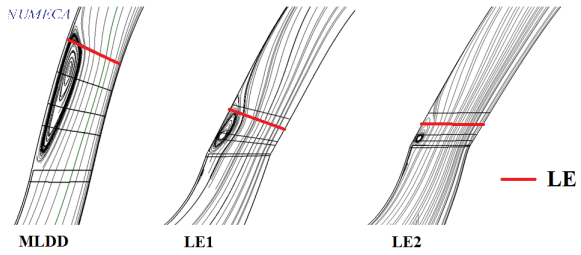

Figure 5.9: a) Mean line design b) LE normal to flow c) LE parallel to impeller TE

The performance results obtained when changing the LE from LE1 to LE2 show there is improvement in the CP and $PR_{s-s(2-4)}$ values however a small reduction in $PR_{t-t(0-4)}$. The performance curves are provided in Appendix H.2. The summary at the design point for the two Leading edges is provided in Table 5.7. The ODD with LE2 was then selected as the final ODD.

Table 5.7: Optimised design point with two different leading edges

Design	$\eta_{t-t(0-4)}$	$PR_{t-t(0-4)}$	C_P	$PR_{s-s(2-4)}$
LE1	79.5	4.48	0.53	1.89
LE2	80%	4.44	0.6	2.04
Improvement	0.62%	-0.89%	11.7 %	5.5%

This decrease in vaneless gap significantly decreased the recirculation bubble as can be seen from the stream lines in Figure 5.10.

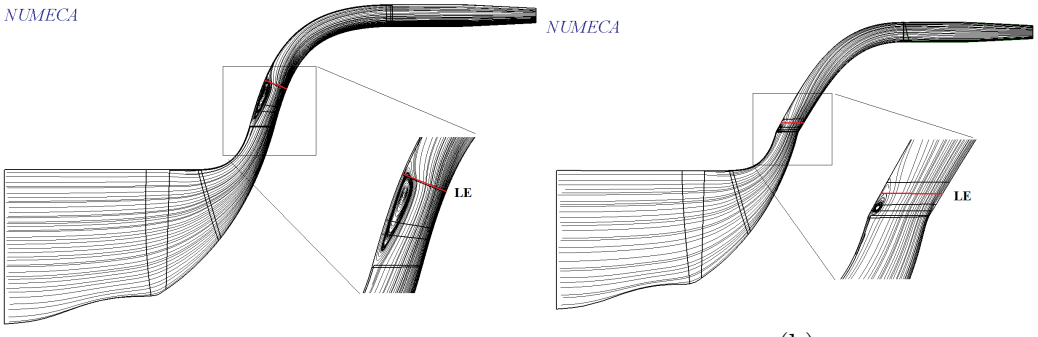

(a) (b)

Figure 5.10: a) Mean line design b) Optimised design

The performance difference between the compressor with ODD and MLDD can be seen from Figures 5.11 and 5.12. A summary of the results at the design point can be seen in Table 5.8. The compressor with the ODD proved to be superior than the MLDD. The $\eta_{t-t(0-4)}$ improved from 73% to 80%. The $PR_{t-t(0-4)}$ has a 7.7% improvement from 4.1 to 4.44. The diffuser C_P

had the biggest improvement, with a 28.33% improvement from 0.43 to 0.6. The $PR_{s-s(2-4)}$ improved by 21.49% from 1.6 to 2.04. The outlet diffuser static pressure was increased from 380 kPa to 419 kPa. There was not much improvement with the diffuser discharge flow angle, α_4, increasing from 60° to 63°, the objective was to get it as close to 90° as possible. The operating range of the compressor remained approximately unchanged. The calculated operating ranges for the compressor with the MLDD and ODD were 14.2% respectively. The operating range however shifted with the ODD having a larger choke limit, but a larger stall point mass flow.

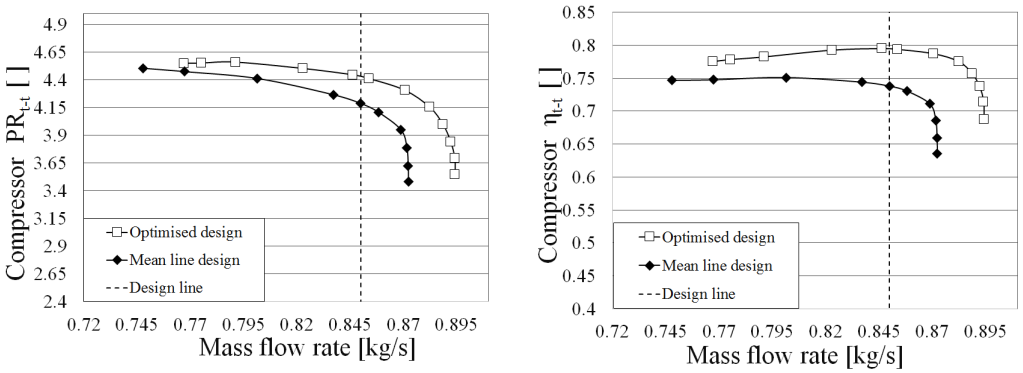

Figure 5.11: a) Compressor total-to-total pressure ratio b) Compressor total-to-total isentropic efficiency

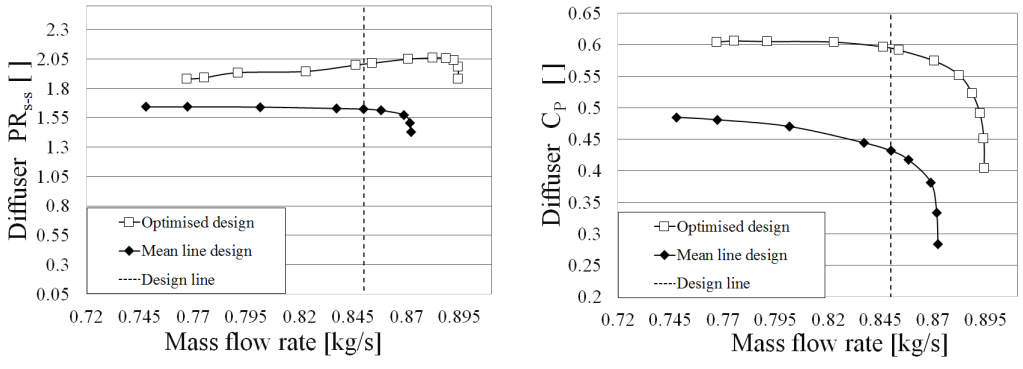

Figure 5.12: a) Diffuser static-to-static pressure ratio b) Diffuser static pressure recovery coefficient

Table 5.8: Design point results

Design	$\eta_{t-t(0-4)}$	$PR_{t-t(0-4)}$	C_P	$PR_{s-s(0-2)}$
Mean line design	73%	4.1	0.43	1.6
Optimized design	80%	4.44	0.6	2.04
Improvement	**8.75%**	**7.70%**	**28.33%**	**21.56%**

5.7 Closing remark

It is clear from the the results obtained that the optimised design has superior performance compared to the mean line design. The optimised design also proved to have removed the recirculation bubble that formed in the vaneless space of the mean line design. This phenomenon was also found in the work done by de Villiers (2014), where decreasing the vaneless gap decreases the size of the recirculation bubble.

Chapter 6

Results discussion

6.1 Introduction

The aim of this chapter is to discuss and summarise the performance results obtained during this research. Firstly the performance results for the mean line diffuser design (MLDD) are discussed. The MLDD's computational fluid dynamics (CFD) performance results are compared to performance results obtained from a mean line analysis performed by the mean line code (MLC). The performance results obtained from the optimised diffuser design (ODD) is discussed, comparing it to the MLDD. A vaneless evaluation is also discussed; this includes the vaneless diffuser (VLD) and vaneless diffuser with de-swirler vanes (VLDD). The eventual manufactured ODD geometry will also be displayed.

6.2 Mean line results

The performance results for the MLDD obtained from the MLC are compared to the CFD results. The design point ($\dot{m} = 0.85kg/s$) performance values are tabulated in Table 6.1. The performance curves for the MLDD are illustrated in Figure 6.1, showing the diffuser static pressure recovery coefficient (C_P) and the diffuser static-to-static pressure ratio ($PR_{s-s(2-4)}$) values throughout the operating mass flow rate range.

Table 6.1: Parameters at design point

	$\eta_{t-t(0-4)}$	$PR_{t-t(0-4)}$	Diffuser C_P	$PR_{s-s(2-4)}$
MLC	81%	4.5	0.565	1.76
CFD	73%	4.18	0.43	1.626
Deviation	**9.8%**	**7.1%**	**23.8%**	**7.6%**

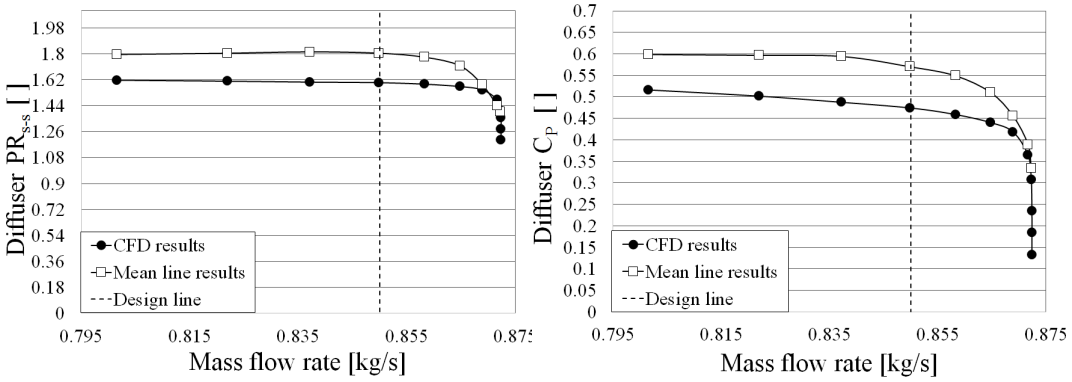

Figure 6.1: a) Diffuser static-to-static pressure ratio b) Diffuser static pressure recovery coefficient

The MLC performance results at design point compared to the CFD performance results show a 9.8% and 7.1% difference for compressor stage $\eta_{t-t(0-4)}$ and $PR_{t-t(0-4)}$ values respectively. The largest difference was for the diffuser C_P values, where a difference of 23.8% was observed at design point. It is assumed that the difference is primarily due to the the MLC not taking 3-D effects into account. This include the highly distorted flow that is observed in the vaneless gap of the MLDD. The performance characteristic curves for the MLC ,as can be seen from Figure 6.1 do trend well with the CFD characteristic curves. The work input of the compressor was calculated to be 170.6 kW (design point) by using Equation 6.1. It was proposed that the compressor will be driven by a 180 kW turbine. This means that the remaining 9.4 kW power will be contributed to the thrust of the MGT.

$$\dot{W}_{comp} = \frac{\dot{m} T_{01} \left(PR_{t-t(0-4)}{}^{\frac{\gamma-1}{\gamma}} - 1 \right)}{\eta_{t-t(0-4)}} \tag{6.1}$$

The MLDD discharge flow angle, relative to the tangential direction was calculated to be 60°. This was the best discharge flow angle that could be achieved without increasing the number of blades and reducing the operating range. The static pressure at the diffuser exit was found to be 380 kPa, where the static pressure propagation through the compressor can be seen from Figure 6.2. The choke and stall mass flow rates were calculated to be 0.872 kg/s and 0.747 kg/s respectively. This yielded an operating range of 14.2%.

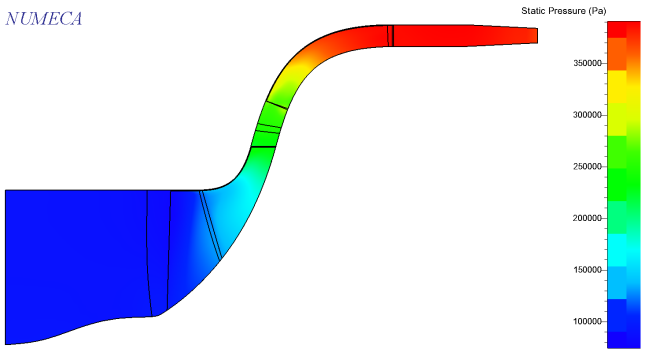

Figure 6.2: Static pressure propagation

6.3 Optimised design

The ODD proved to be superior in performance compared to the MLDD. Table 6.2 shows the summary of the results at design point, as can be seen from the table there is a clear increase in performance from the MLDD to the ODD, where there is a 8.75% and 7.7% increase in compressor $\eta_{t-t(0-4)}$ and $PR_{t-t(0-4)}$ respectively. There is a 28.33% and 21.56% increase in diffuser C_P and $PR_{s-s(0-2)}$ respectively. The ODD did not show a large improvement for the discharge flow angle, α_{4c} with an increase of 3°. The characteristic curves are provided in Figure 6.3 for the diffuser's C_P and $PR_{s-s(0-2)}$. It shows there is a significant increase in choke mass flow from MLDD to ODD however the operating range remained approximately constant with a value of 14.2%.

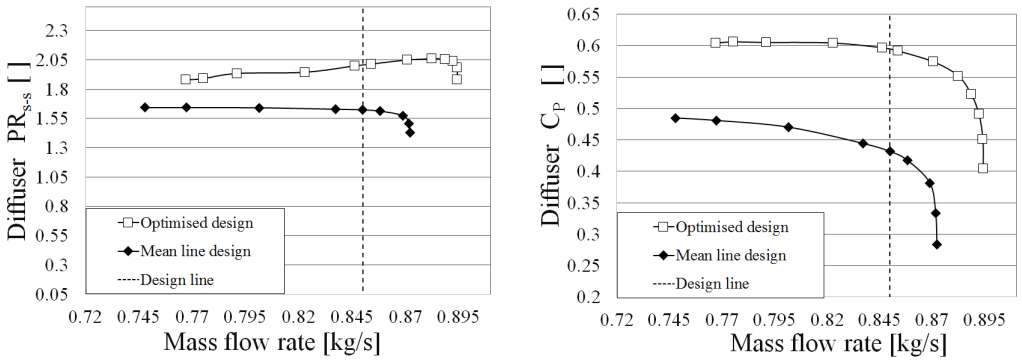

Figure 6.3: a) Diffuser static-to-static pressure ratio b) Diffuser static pressure recovery coefficient

Table 6.2: Design point results

Design	$\eta_{t-t(0-4)}$	$PR_{t-t(0-4)}$	C_P	$PR_{s-s(0-2)}$
Mean line design	73%	4.1	0.43	1.6
Optimized design	80%	4.44	0.6	2.04
Improvement	**8.75%**	**7.70%**	**28.33%**	**21.56%**

Although the compressor stage design point target $\eta_{t-t(0-4)}$ of 85% was not reached a considerable rise in static pressure was achieved. The diffuser outlet static pressure was increased from a value of 380 kPa obtained from the MLDD to a value of 419 kPa obtained from the ODD where Figure 6.4 shows the static pressure propagation through the compressors with the MLDD and the ODD . The compressor with the ODD work requirement was equal to 165.66 kW, this was calculated by using Equation 6.1. This means that the ODD reduced the required compressor power by 3% from the MLDD. This means that the remaining 14 kW of power will be contributed to the thrust of the engine with the proposed 180 kW turbine.

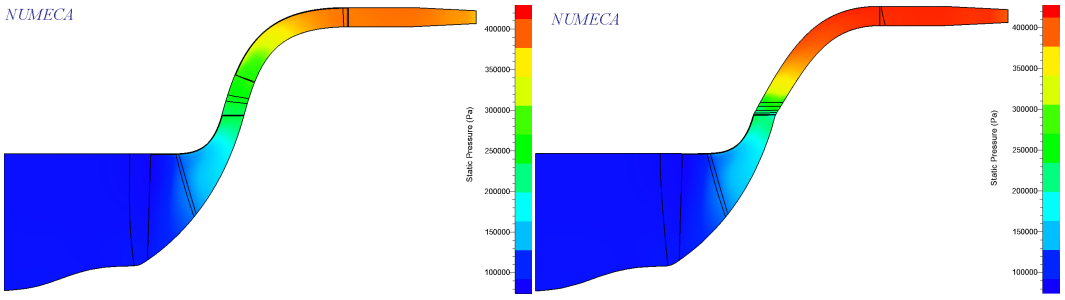

(a) (b)

Figure 6.4: a) Compressor static pressure contour with MLDD b) Compressor static pressure contour with ODD

6.4 Vaneless diffuser performance

Because most mixed flow impellers make use of vaneless diffusers. This section aims to evaluate the performance of a compressor with a vaneless diffuser (VLD) and a compressor with a vaned diffuser (ODD). The meridional channel of the ODD was used for the VLD analysis. De-swirler vanes were also added to the VLD to remove the swirl. However the VLD and the VLDD were evaluated separately.

6.4.1 Vaneless diffuser

The ODD's meridional channel was used as the VLD by removing the diffuser vanes. The VLDD was simulated and the results were compared to the VLD results. The compressor with the ODD proved to have higher, $\eta_{t-t(0-4)}$ and $PR_{t-t(0-4)}$ values compared to the VLD. This can be seen from the compressor characteristic curves shown in Figure 6.5. The ODD also had higher C_P and $PR_{s-s(0-2)}$ values compared to the compressor with the VLD. This is shown from the performance curves in Figure 6.6.

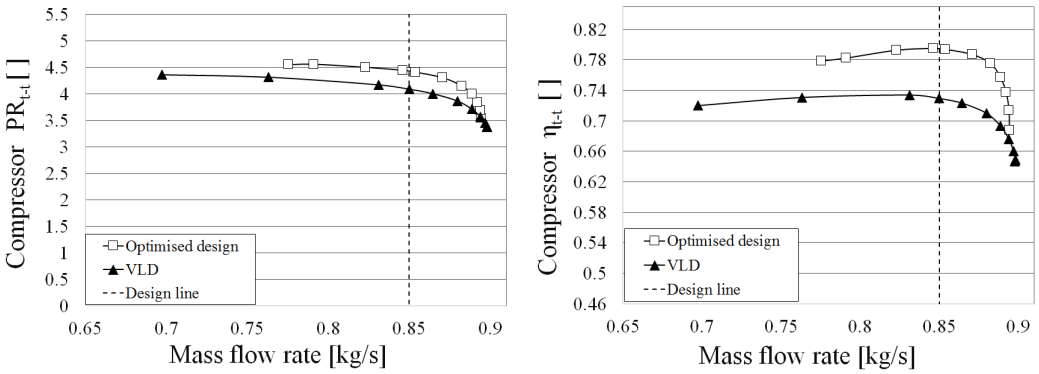

Figure 6.5: a) Compressor total-to-total pressure ratio b) Compressor total-to-total isentropic efficiency

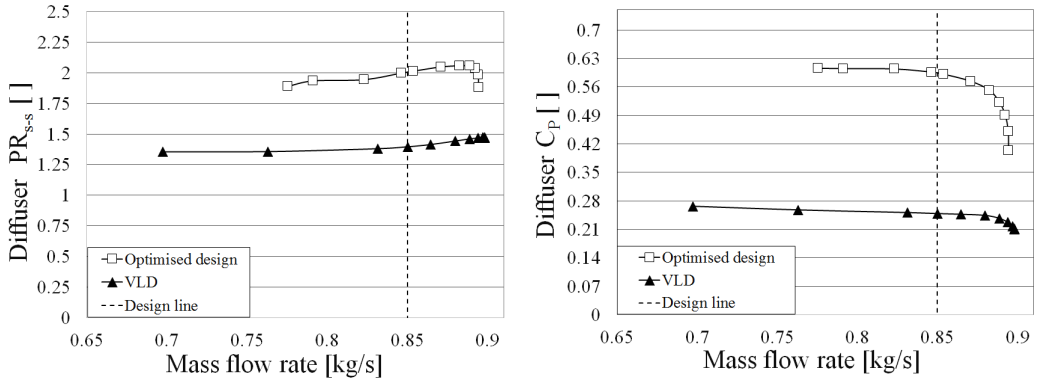

Figure 6.6: a) Diffuser static-to-static pressure ratio b) Diffuser static pressure recovery coefficient

Although the compressor with the ODD proved to have better performance than the compressor with the VLD, the compressor with the VLD had a considerably wider operating range. The compressor with the VLD had a 22.36%

operating range versus the 14.2% operating range of the compressor with the ODD. However the compressor with VLD did not have a significantly larger choke mass flow compare to the ODD, but did have a much smaller stall mass flow rate with a value of 0.697 kg/s versus a value of 0.77 kg/s achieved by the compressor with the ODD. This lower stall mass flow rate value clearly shows a larger operating range for the compressor with the VLD. For the VLD to give the equivalent energy conversion as the ODD the VLD has to have a considerably larger outlet radius, which is not feasible due to the size constraints of MGTs.

6.4.2 Vaneless diffuser with de-swirlers

To remove swirl from the VLD shown in section 6.4.1, de-swirlers vanes were added to the VLD channel. The geometric properties for the de-swirler vanes are discussed in Appendix J. The VLDD were simulated and the results were compared to the VLD. Figures 6.7 and 6.8 show the performance results of the VLD and the VLDD.

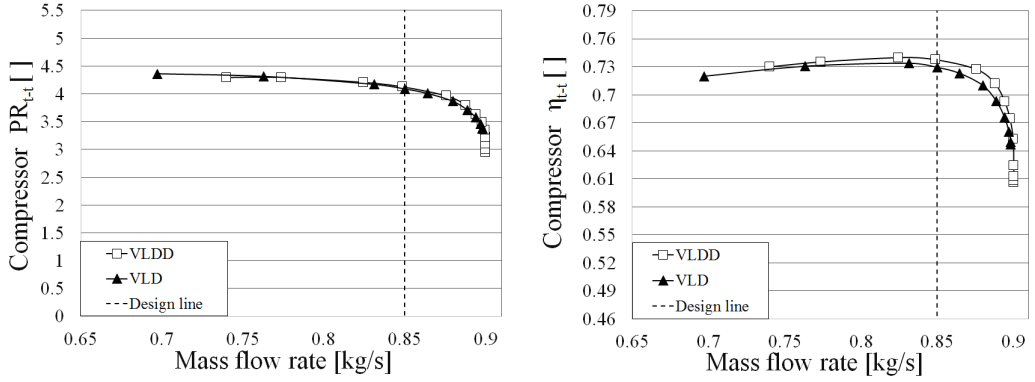

Figure 6.7: a) Compressor total-to-total pressure ratio b) Compressor total-to-total isentropic efficiency

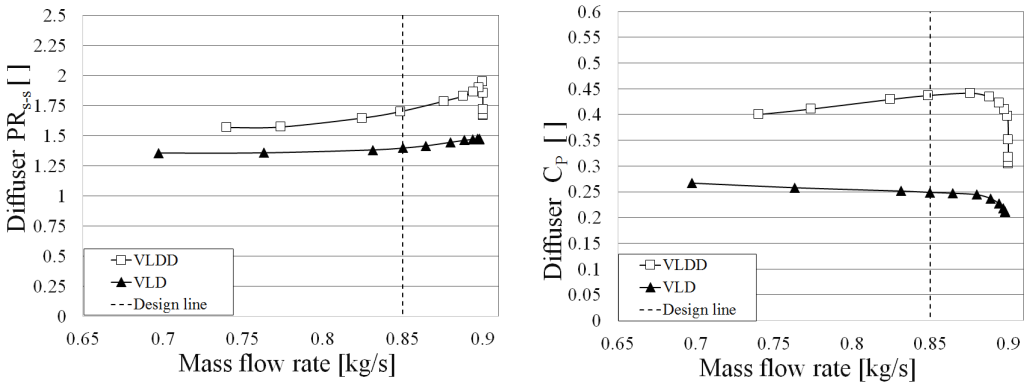

Figure 6.8: a) Diffuser static-to-static pressure ratio b) Diffuser static pressure recovery coefficient

The characteristic curves show that the compressor performance values ($\eta_{t-t(0-4)}$ and $PR_{t-t(0-4)}$) was not significantly affected by adding de-swirlers vanes, however the diffuser performance was improved. At the design point the C_P value increased from 0.248 to 0.4, and the $PR_{s-s(0-2)}$ value increased from 1.3 to 1.7. The reason for the VLDD's improved performance is because the addition of the de-swirler vanes increased the overall diffusion rate of the VLD thus increasing the energy conversion. Adding de-swirler vanes to the VLD show a reduction in operating range as the stall mass flow rate of the VLDD was found to be at a value of 0.74 kg/s compared to the VLD's stall mass flow rate of 0.697 kg/s. The recirculation bubble is also present in both the VLD and VLDD as seen in Figure 6.9. Adding de-swirlers vanes had no significant influence on the size of the bubble because it was outside the recirculation bubble zone. The VLDD had a discharge flow angle, α_{4c} of 68°compared to the 30°that was obtained from the VLD exit.

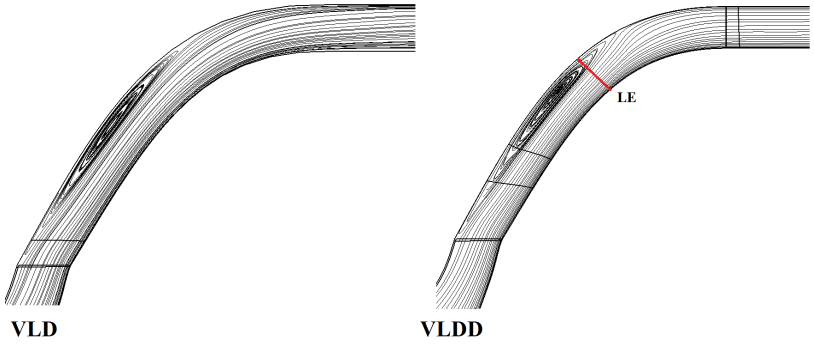

Figure 6.9: Recirculation bubble

6.5 Diffuser results summary

The summary for all the diffuser types are shown in Table 6.3. The performance characteristic curves are shown in Figures 6.10 and 6.10. As can be seen from the results the ODD has the best performance values compared to all the other diffuser types.

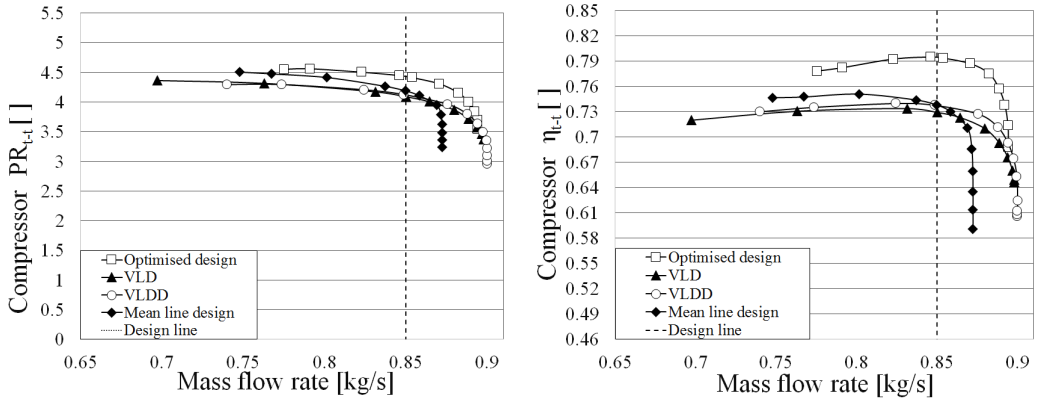

(a) (b)

Figure 6.10: a) Compressor total-to-total pressure ratio b) Compressor total-to-total isentropic efficiency

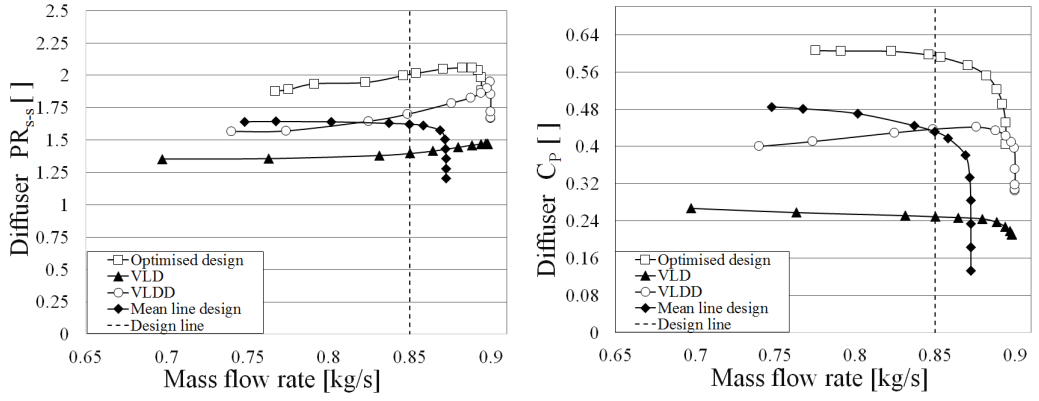

(a) (b)

Figure 6.11: a) Diffuser static-to-static pressure ratio b) Diffuser static pressure recovery coefficient

Table 6.3: Results summary at design point

Design	$\eta_{t-t(0-4)}$	$PR_{t-t(0-4)}$	C_P	$PR_{s-s(2-4)}$
Mean line vaneless	72.0%	4.00	0.23	1.30
Mean line design	73.0%	4.10	0.43	1.63
Optimized design	80.0%	4.44	0.60	2.04
VLD	72.7%	4.08	0.25	1.30
VLDD	72.9%	4.00	0.40	1.70

6.6 Manufacturing

The ODD was manufactured for the purpose of fitting it to a test rig, however tests have not been performed on the model. Figure 6.12 shows the CAD drawing and pictures of the manufactured parts are provided in Appendix K.

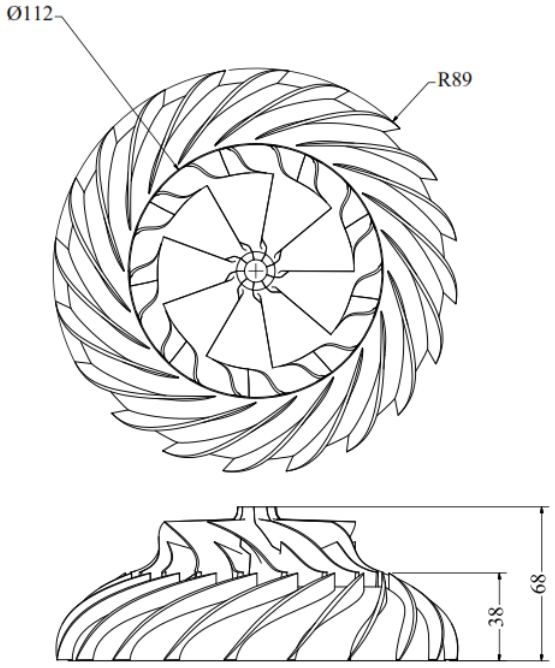

Figure 6.12: 3-D Compressor drawing

6.7 Closing remarks

It is clear from the CFD performance results in Table 6.3 that the use of a vaned diffuser is beneficial if the concern of the designer is to obtain high performance values in a limited space. If the designer is interested in maximising the operating range the use of a vaneless diffuser would be a good choice. Using a vaneless diffuser with de-swirler vanes does improve the C_P

and $PR_{s-s(2-4)}$ values but narrows the operating range. The final cross-over diffuser that is used for this research was the ODD. The compressor with the ODD's performance maps at different speeds have also been plotted and is shown in Appendix I. The plot shows that it is possible for the compressor to operate in a region with operational speeds larger and smaller than the design speed that will produce the design mass flow rate of 0.85 kg/s. However this range has not been determined.

Chapter 7

Conclusion and recommendation

A compact new cross-over diffuser (CD) was designed for a mixed flow compressor employed in a 600 N thrust MGT engine. The CD is a single vane diffuser that has the ability to capture flow from any impeller meridional discharge angle without inducing meridional passage flow separation. This diffuser design is particularly favourable for mixed flow impellers due to their non-radial discharge. The design was done in a three step process; first by performing a 1-D mean line design followed by the computational fluid dynamics evaluation of that particular design and finally optimising the design.

7.1 Design summary

The mean line design was performed with the use of a MLC developed by Burger (2016). The mean line code is based on work presented by Aungier (2000). A vaneless CD channel was designed to form the base of the design process. The geometric parameters of the vaneless passage were varied to find the best possible design. Once the best mean line vaneless channel was found, vanes were added to the passage. The vane's parameters were then varied to find the best MLDD. If the performance could no longer be improved, this was then taken as the final MLDD. The resultant MLDD has 20 vanes with an axial length of 38 mm . The exit blade angle, β_4 and inlet incidence angle, i_3 were selected as 67° and 1.5° respectively. The maximum blade thickness, t_{bmax} and vaneless gap radius ratio, r_3/r_2, were set as 2 mm and 1.18 respectively.

The MLDD was simulated at off design and design conditions (stall to choke) with the use of NUMECA Fine^{TM}/Turbo. The MLDD had a 0.872 kg/s choke mass flow rate and a stall mass flow rate of 0.747 kg/s. The compressor stage $\eta_{t-t(0-4)}$ and $PR_{t-t(0-4)}$ were calculated to be 73% and 4.1 respectively. The

diffuser C_P and $PR_{s-s(2-4)}$ were calculated to be 0.43 and 1.626 respectively. The MLDD showed a large recirculation bubble at the exit of the impeller. Upon initial inspection it was evaluated that a smaller vaneless gap reduces the recirculation bubble. It was then decided that the vaneless gap size was to be used as an optimisation parameter.

A multi-point (stall, design and choke point) optimisation was performed using the MLDD as the base geometry. The optimisation was done with the use of NUMECA Design3D^{TM} software. The first step was to parametrise the MLDD geometry using NUMECA's AutoBlade^{TM} software. The next step was to do database generation with the use of Design3D^{TM}. The final step was to perform the actual optimisation using Design3D^{TM}. The ODD proved to be superior in performance compared to the MLDD. The compressor with the ODD at design point had $\eta_{t-t(0-4)}$ and $PR_{t-t(0-4)}$ values of 80% and 4.4 respectively. The ODD C_P and $PR_{s-s(2-4)}$ values at design point were calculated to be 0.6 and 2.04 respectively. The compressor with the ODD had an operating range of 14.2% and a choke mass flow rate of 0.89 kg/s. The ODD also showed a significant reduction in the recirculation bubble at the impeller's exit.

Although the ODD had a better performance compared to the MLDD. It did not reach the target compressor stage $\eta_{t-t(0-4)}$ of 85%, with a value of 5.8% lower than the target value. However the compressor stage $PR_{t-t(0-4)}$ had a 13% higher value than the target value of 3.83.

Most mixed flow compressor makes use of vaneless diffusers. This research evaluated the feasibility of using a vaneless diffuser over a vaned diffuser design. The meridional channel of the ODD was used as the vaneless diffuser (VLD). To remove the swirl, de-swirler vanes were also added to the VLD and the performance results were compared. The compressors with the VLD and VLDD showed values for the compressor stage $\eta_{t-t(0-4)}$ of 72.7% and 72.9% at design point respectively. The compressor stage $PR_{t-t(0-4)}$ values were calculated to be 4.00 and 4.08 for the VLD and VLDD respectively. The VLD C_P and $PR_{s-s(2-4)}$ design point values were calculated to be 0.248 and 1.3 respectively where the VLDD's C_P and $PR_{s-s(2-4)}$ values were 0.4 and 1.7 respectively. From these results it's clear that the ODD is superior to the VLD and the VLDD. However the VLD and VLDD have wider operating ranges compared to the ODD.

7.2 Conclusion

The CD is a favourable diffuser type for a mixed flow compressor due its ability to capture any impeller meridional discharge passage flow angle, α_{2a}. The discharge flow conditions of the impeller used in this thesis were highly non-uniform, resulting in deviations from the MLC and the CFD performance values. This is due the MLC not taking these 3-D affects into account. These 3-D affects can be seen from a recirculation bubble that formed in the vaneless gap. It was discovered that the size of the recirculation depends on the size of the vaneless gap, whereby a reduction in vaneless gap size reduces the recirculation bubble. This decrease in recirculation bubble size caused an increase performance as seen from the performance results obtained from the ODD.

The results indicate that a vaneless diffuser does not perform as well as a vaned diffuser with the same meridional passage geometry. However a vaneless diffuser does have much wider operating range compared to the vaned diffuser. If a vaneless diffuser had to achieve the same performance results as a vaned diffuser design the size of the vaneless diffuser would have to be considerably larger. Although the operating range for the vaned diffuser is lower than that of the vaneless diffuser the performance is much higher for the same radial and axial length making the use of vaned diffusers a favourable choice for small gas turbine engines.

7.3 Recommendations

A next evolution to this project should be an optimisation process for both CD and mixed flow impeller rows simultaneously. This would be done to minimise the flow distortions at the exit of the impeller thus minimising diffuser inlet losses. The hypothesis is that the compressor stage $\eta_{t-t(0-4)}$ and diffuser C_P would be increased significantly by performing the multi-row optimisation.

Significant focus is placed on the diffuser discharge flow angle, α_{4c} that determines the inlet swirl into the combustion chamber. A study of the effects of pressure losses through the combustion chamber due to swirl is recommended. The study should also investigate the effect of swirl on combustor performance and flame propagation.

Due to the small vaneless gap that exist between the ODD and the impeller, an appropriate study should be done to investigate the affects the proximity of diffuser vanes have on the impeller vibration modes.

Finally experimental test of the diffuser designs should be done to validate the CFD performance.

Appendices

Appendix A

Mean line blade surface construction

The mean line blade surfaces are constructed with the use of the three expressions given by Equation A.1. The three expressions are vectors that help with describing the blade surfaces (Aungier, 2000). The vector $\vec{S}$ is a defined unit vector tangent to the vane mean line stream surface defined by vector $\vec{B}$, and $\vec{T}$ is a vector that are normal to the vane mean surface.

$$\begin{aligned} \vec{S} &= S_x\vec{i} + S_y\vec{j} + S_z\vec{k} \\ \vec{B} &= B_x\vec{i} + B_y\vec{j} + B_z\vec{k} \\ \vec{T} &= \vec{S} \times \vec{B} = T_x\vec{i} + T_y\vec{j} + T_z\vec{k} \end{aligned} \tag{A.1}$$

The vector $\vec{S}$ in its Cartesian coordinates are determined from Equation A.2:

$$\begin{aligned} S_x &= \sin\theta \sin\alpha_C \sin\bar{\beta} + \cos\theta \cos\bar{\beta} \\ S_y &= \cos\theta \sin\alpha_C \sin\bar{\beta} - \sin\theta \cos\bar{\beta} \\ S_z &= \cos\alpha_C \sin\bar{\beta} \end{aligned} \tag{A.2}$$

The blade mean line surface, $\vec{B}$ depends upon the blade style (Aungier, 2000). This research project made use of straight-line element blades the Cartesian coordinates are given by Equation A.3:

$$\begin{aligned} B_x &= \frac{x_{shroud} - x_{hub}}{L} \\ B_y &= \frac{y_{shroud} - y_{hub}}{L} \\ B_z &= \frac{z_{shroud} - z_{hub}}{L} \end{aligned} \tag{A.3}$$

The vector normal to the vane surface, $\vec{T}$, written in its Cartesian coordinates as noted from Equation A.4

$$\begin{aligned} T_x =& S_z B_y - S_y Bz \\ T_y =& S_x B_z - S_z Bx \\ T_z =& S_y B_x - S_x By \end{aligned} \tag{A.4}$$

The Cartesian coordinates for the resultant blade surface are determined from the vector $\vec{T}$ and is described by Equation A.5

$$\begin{aligned} x =& \bar{x} \pm \frac{1}{2} t_b T_x \\ y =& \bar{y} \pm \frac{1}{2} t_b T_y \\ z =& \bar{z} \pm \frac{1}{2} t_b T_z \end{aligned} \tag{A.5}$$

Appendix B

.geomTurbo file format

The *.geomTurbo* geometry file that is required by NUMECA AutoGrid5™ software contains the meridional passage curves and the blade geometry of the cross-over diffuser and the mixed flow impeller. However the cross-over diffuser and impeller can have different *.geomTurbo* files as long as they have the same meridional passage geometry coordinates.

```
GEOMETRY TURBO
VERSION 5.3
TOLERANCE 1E-06
NI_BEGIN CHANNEL
NI_BEGIN basic_curve
NAME hub_curve_1
DISCRETISATION 10
DATA_REDUCTION 0
NI_BEGIN zrcurve
ZR
+168
-39.1999990000 0.8000000300
. . .
68.0000000000 83.2000000000
NI_END zrcurve
NI_END basic_curve
NI_BEGIN basic_curve
NAME hub_curve_2
DISCRETISATION 10
DATA_REDUCTION 0
NI_BEGIN zrcurve
ZR polyline
+3
68 83.200
88 83.2000
```

```
108 84.2
NI_END zrcurve
NI_END basic_curve
NI_BEGIN basic_curve
NAME shroud_curve_1
DISCRETISATION 10
DATA_REDUCTION 0
NI_BEGIN zrcurve
ZR
+128
-39.1999990000 43.4340000000
. . .
68.0000000000 89.0000000000
NI_END zrcurve
NI_END basic_curve
NI_BEGIN basic_curve
NAME shroud_curve_2
DISCRETISATION 10
DATA_REDUCTION 0
NI_BEGIN zrcurve
ZR polyline
3
68 89.00000
88 89.00000
108 88.00000
NI_END zrcurve
NI_END basic_curve
NI_BEGIN channel_curve hub
NAME hub
VERTEX CURVE_P hub_curve_1 0
VERTEX CURVE_P hub_curve_1 1
VERTEX CURVE_P hub_curve_2 0
VERTEX CURVE_P hub_curve_2 1
NI_END channel_curve hub
NI_BEGIN channel_curve shroud
NAME shroud
VERTEX CURVE_P shroud_curve_1 0
VERTEX CURVE_P shroud_curve_1 1
VERTEX CURVE_P shroud_curve_2 0
VERTEX CURVE_P shroud_curve_2 1
NI_END channel_curve shroud
NI_END CHANNEL

NI_BEGIN nirow
```

NAME Crossover_Diffuser
TYPE normal
PERIODICITY 20
NI_BEGIN NIBlade
NAME Main Blade
NI_BEGIN nibladegeometry
TYPE GEOMTURBO
GEOMETRY_MODIFIED 0
GEOMETRY TURBO VERSION 5
blade_expansion_factor_hub 0.1
blade_expansion_factor_shroud 0.15
intersection_npts 10
intersection_control 0
data_reduction 0
data_reduction_spacing_tolerance 1E-06
data_reduction_angle_tolerance 90
units 0.001
number_of_blades 20
suction
SECTIONAL
2
section 1
XYZ
100
0.000000000000000 -64.944924831078637 38.599563921366432
. . .
60.519174083309302 -57.095414912408209 67.817889445511597
section 2
XYZ
100
0.000000000000000 -67.320869628293295 32.538903734920716
. . .
64.715650808336250 -61.099111091728915 67.817889445511597
pressure
SECTIONAL
2
section 1
XYZ
100
0.000000000000000 -64.944924831078637 38.599563921366432
. . .
59.876296096773991 -57.769247887413151 68.182110554488403
section 2
XYZ

```
100
0.000000000000000 -67.320869628293295 32.538903734920716
. . .
64.072772821800953 -61.772944066733857 68.182110554488403
NI_END nibladegeometry
NI_END NIBlade
NI_END GEOMTURBO

NI_BEGIN GEOMETRY
NI_END GEOMETRY
```

Appendix C

1-D performance calculations scheme

Before the calculation can commence its important to identify the Equations that are utilised in the code to determine the fluid properties at certain state, n, in the compressor. These equations are represented by Equations C.1-C.8

$$T_n = T_{0n} - \frac{{C_n}^2}{2cp} \tag{C.1}$$

$$C_n = \sqrt{{C_{\theta n}}^2 + {C_{mn}}^2} \tag{C.2}$$

$$C_{mn} = \frac{\dot{m}}{\rho_n A_n} \tag{C.3}$$

$$\rho_n = \frac{P_n}{R_{air} T_n} \tag{C.4}$$

$$A_n = 2\pi r_n b_n \tag{C.5}$$

$$P_n = \frac{P_{0n}}{\frac{T_{0n}}{T_n}^{\frac{\kappa}{\kappa-1}}} \tag{C.6}$$

$$Ma_n = \frac{C_n}{\sqrt{\kappa R_{air} T_n}} \tag{C.7}$$

$$\alpha_n = \arctan \frac{C_{mn}}{C_n} \tag{C.8}$$

C.1 Vaneless performance

The first step that was used to analyse the mean line performance of the compressor and the diffuser was to identify the input parameters. The input

parameters of the mean line results were obtained from the exit of the impeller, these parameters were obtained from CFD analysis and are listed in Table C.1.

Table C.1: Inlet flow conditions

Quantity	Unit
Absolute velocity (C_2)	m/s
Total temperature (T_{02})	K
Static pressure (P_2)	Pa
Total pressure (P_{02})	Pa
Mass flow rate ($\dot{m}$)	kg/s

Other parameters at the impeller exit that are unknown is calculated from Equations C.1-C.8.

The code then commences by calculating the exit of the vaneless gap parameters. The change in the parameters from impeller exit (state 2) to vaneless gap exit(state 3) is driven by the dynamic loss across the vaneless gap and the increase in flow area. Equation C.9 shows the total pressure change due to the loss across the vaneless gap.

$$P_{03} = P_{02} - (P_{02} - P_2)\omega_{vg} \tag{C.9}$$

where ω_{vg} represent the losses across the vaneless gap. Aungier (2000) suggest that the effect of the losses in the vaneless gap are small and a 0.1% loss of the dynamic pressure is proposed, $\omega_{vg} = 0.001$. The remaining parameters needed for the calculation at this state was done by using Equations C.1-C.8.

C.2 Vaned performance

Similar to the vaneless gap the vaned section follows the same process by using Equations C.1 to C.8 to calculate the parameters needed to evaluate the performance. The Equations to determine the total pressure at the exit of the diffuser is given in Equation C.10.

$$P_{04} = P_{02} - (P_{03} - P_3)\omega_{tot} \tag{C.10}$$

The loss, ω_{tot}, is a summation of all the losses accumulated in the blade section. The losses are divided into two sections namely inlet losses and blade passage losses:

C.2.1 Inlet losses

The inlet losses are quantified here as follows:

Choke losses

The first inlet loss accounted for is the choke loss and is depicted by Equation C.11:

$$\begin{aligned} \omega_{ch} &= 0; & X \leq 0 \\ \omega_{ch} &= 0.5(0.05X + X^7); & X > 0 \end{aligned} \tag{C.11}$$

where the parameter X is determined by Equation C.12 and the parameter $CR = \sqrt{A_3 \sin(\beta_3)/(A_{th})}$ is the contraction correlation.

$$X = 11 - 10\frac{A_{th}CR}{A^*} \tag{C.12}$$

where A^* is the area to which sonic velocity will be reached in the throat.

Incidence losses

The second inlet loss accounted for is the incidence loss represented by Equation C.13

$$\begin{aligned} \omega_i &= 0.8\left(\frac{C_3 - {C_3}^*}{C_3}\right)^2 & C_3 \leq C_3 s \\ \omega_i &= 0.8\left[\left(\left(\frac{C_3}{C_{3s}}\right)^2 - 1\right)\left(\frac{C_{th}}{C_3}\right)^2 + \left(\frac{C_{3s} - {C_3}^*}{C_{3s}}\right)^2\right] & C_3 > C_{3s} \end{aligned} \tag{C.13}$$

where ${C_3}^* = C_{m3}/sin\alpha^*$ is the optimum incidence velocity at optimum incidence angle, ${i_3}^* = \beta_3 - \alpha^*$, and C_{3s} is the stall incidence velocity.

Minimum incidence losses

The third inlet loss that was accounted for was the minimum incedence loss that is depicted by Equation C.14:

$$\omega_{i0} = 0.8\left(\frac{C_3 - C_{th}}{C_3}\right)^2 + \left(\frac{Z_{VD}t_b i_{th}}{2\pi r_3}\right)^2 \tag{C.14}$$

C.2.2 Passage and blade losses

The passage and blade losses accounted for are as follows:

Skin friction losses losses

The first passage and blade loss that is accounted for is the skin friction loss of the vanes passage and is represented by Equation C.15:

$$\omega_{sf} = \frac{4cf\left(\frac{\bar{C}}{C_3}\right)^2 L_B}{\frac{d_H}{{d_{dh}}^{0.25}}} \tag{C.15}$$

where the term, d_{dh}, corrects the skin friction coefficient from the fully turbulent model. The friction factor, cf, is the friction factor and d_H is the hydraulic diameter.

Blade loading losses

The blade loading losses are also accounted for and is depicted by Equation C.16

$$\omega_{bl} = \left(\frac{\triangle C}{6C_3}\right)^2 \tag{C.16}$$

where $\triangle C$ is the average blade-to-blade velocity across the inlet and outlet of the vane section of the diffuser and calculated from Equation C.17:

$$\triangle C = \frac{2\pi(r_3 C_{\theta 3} - r_4 C_{\theta 4})}{Z_{VD} L_B} \tag{C.17}$$

Diffusion losses

The diffusion losses are also accounted for and is depicted by Equation C.18

$$\omega_{diff} = DD \frac{2\sigma}{\cos(\frac{\pi}{2} - \alpha_4)} \left(\frac{\cos(\frac{\pi}{2} - \alpha_3)}{\cos(\frac{\pi}{2} - \alpha_4)}\right)^2 \tag{C.18}$$

and the parameter DD is depicted by Equations C.19

$$DD = (0.003 + 0.02375D - 0.05D^2 + 0.125D^3) \tag{C.19}$$

The parameter D is calculated from Equation C.20

$$D = 1 - \left(\frac{C_4}{C_3}\right) + \left(\frac{2(r_3 C_{\theta 3} - r_4 C_{\theta 4})}{2\sigma C_3 (r_3 + r_4)}\right) \tag{C.20}$$

Curvature losses

The vane curvature losses are Represented by Equation C.21:

$$\omega_{hs} = \left(\frac{\kappa_m b_{avg} C_{avg}}{\sqrt{6} C_3}\right)^2 \tag{C.21}$$

where the κ_m is the blade angle with respect to the meridional direction. The C_{avg} and b_{avg} is the average velocity and blade height across the diffuser vane section.

Mixing losses

The mixing losses are Represented by Equation C.22:

$$\omega_{mix} = \left(\frac{C_{wake} - C_{mix}}{C_3}\right)^2 \tag{C.22}$$

Total losses

The total blade losses is then determined by the Equation C.23

$$\omega_{tot} = \omega_{ch} + \omega_i + \omega_{i0} + \omega_{sf} + \omega_{bl} + \omega_{diff} + \omega_{hs} + \omega_{mix} \tag{C.23}$$

Appendix D

Impeller passage

The geometry that was used by Diener (2016) during his numerical process is shown in Figure D.1.

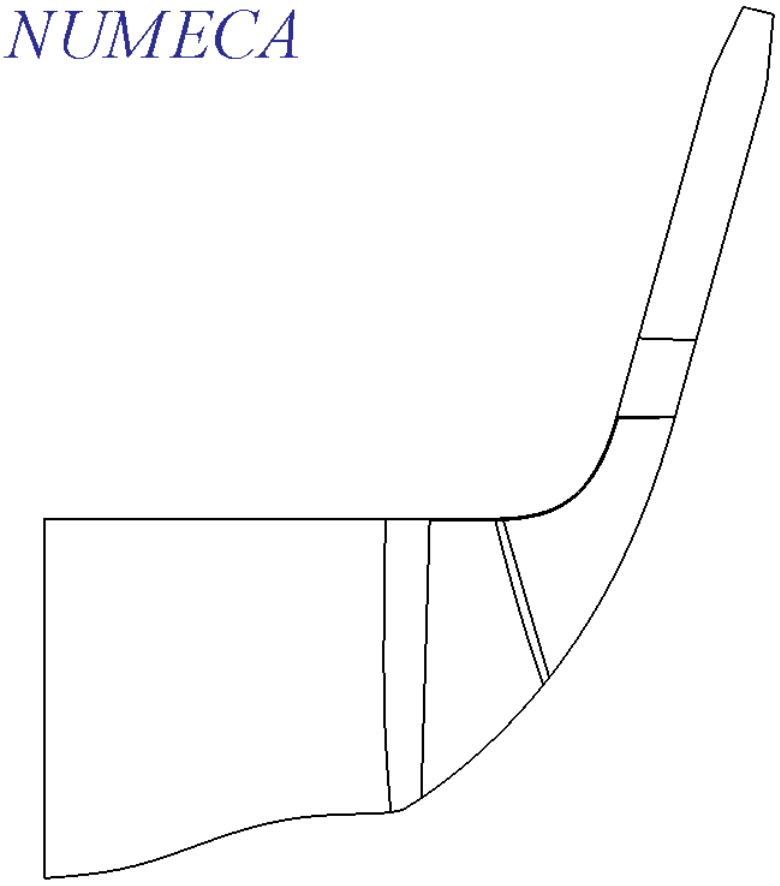

Figure D.1: Meridional flow channel (Diener, 2016)

Appendix E

Additional mesh details

E.1 Mesh independence

E.1.1 Fine mesh

Grid size

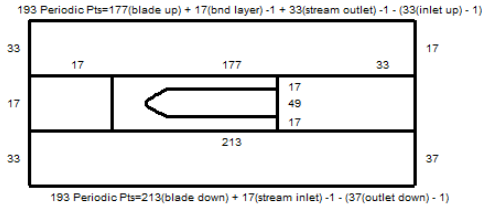

Figure E.1: Diffuser blade-to-blade grid size

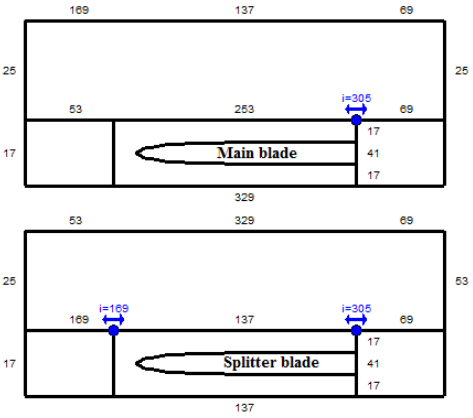

Figure E.2: Impeller blade-to-blade grid size

Mesh quality

Table E.1: Mesh quality final design

Quality	**Impeller**	**Diffuser**	**Mesh requirement**
Minimum orthogonality	20.641°	37.795°	>18°
Maximum expansion ratio	3.1	3.2	<2.5
Maximum aspect ratio	7617	11192	>10000
Maximum angle deviation	35.88°	7.03°	<40°
Bad cell	0.0035%	0.9%	-

E.1.2 Coarse mesh

Grid size

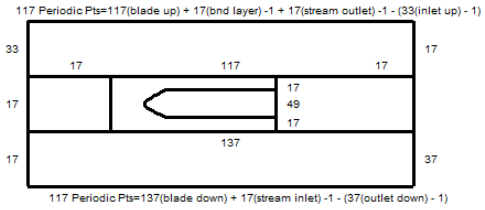

Figure E.3: Diffuser blade-to-blade grid size

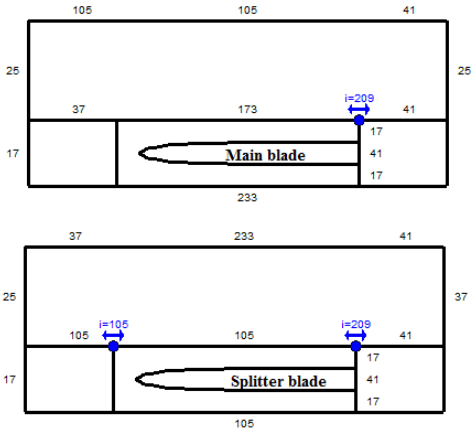

Figure E.4: Impeller blade-to-blade grid size

Mesh quality

Table E.2: Mesh quality final design

Quality	**Impeller**	**Diffuser**	**Mesh requirement**
Minimum orthogonality	18.586°	36.922°	>18°
Maximum expansion ratio	3.391	5.5	<2.5
Maximum aspect ratio	7849	2191.2	>10000
Maximum angle deviation	53.76°	18.92°	<40°
Bad cell	0.0283%	0.01%	-

E.2 Optimised design mesh

Grid size

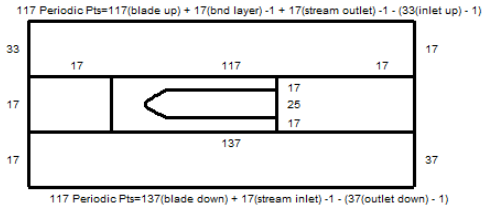

Figure E.5: diffuser blade-to-blade grid size

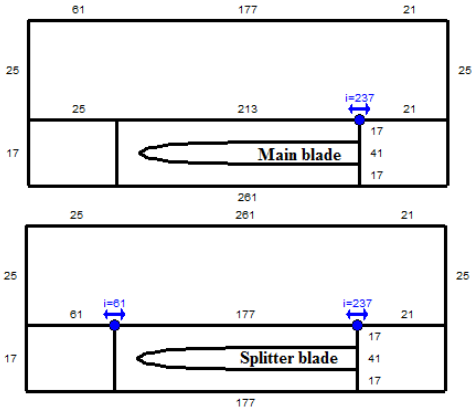

Figure E.6: Impeller blade-to-blade grid size

Mesh quality

Table E.3: Mesh quality optimised design

Quality	**Impeller**	**Diffuser**	**Mesh requirement**
Minimum orthogonality	22.313°	31.076°	>18°
Maximum expansion ratio	2.8	2.7	<2.5
Maximum aspect ratio	3962	2197	>10000
Maximum angle deviation	27.570°	15.590°	<40°
Bad cell	$6.74 \times 10^{-4}\%$	$3.375 \times 10^{-3}\%$	-

E.3 Blade inlet/outlet type topology

The figure below illustrates the angle type that can be present at the blade inlet and outlet

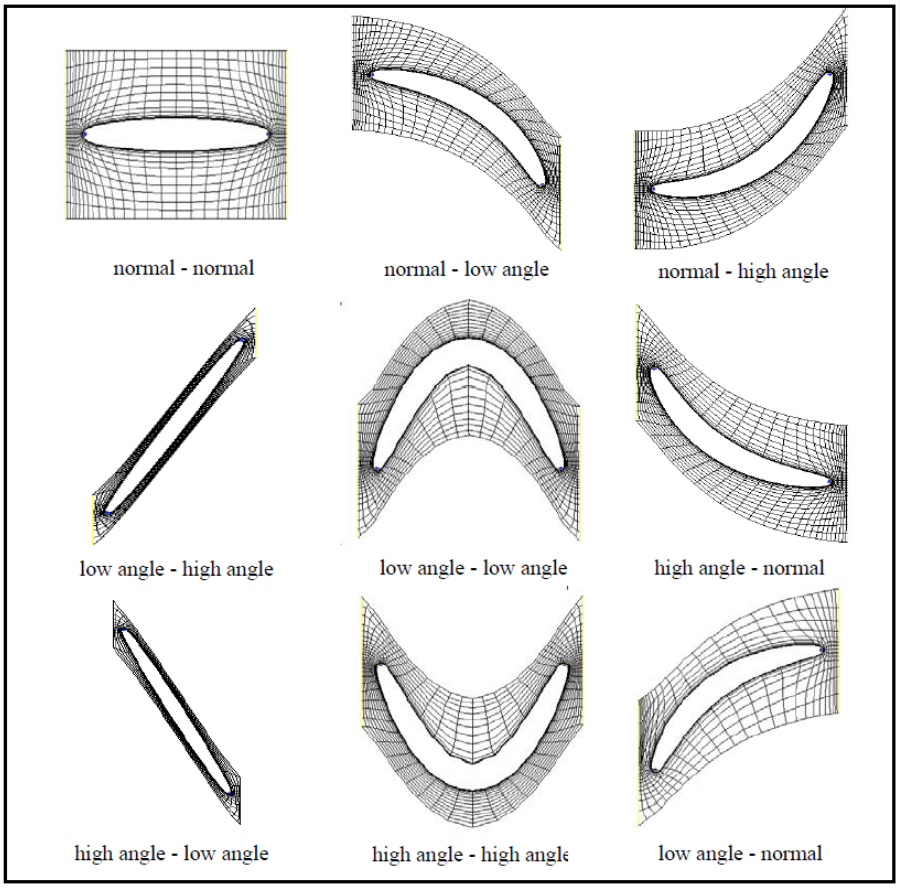

Figure E.7: Blade inlet and outlet topology types NUMECA International (2014a)

Appendix F

Parametrisation

Frozen parameters

Name	Lower bound	Value	Upper bound
HUB_Z1	-39.19981963	-39.19981963	-39.19981963
HUB_R1	0.798001915	0.798001915	0.798001915
HUB_Z2	-29.89762567	-29.89762567	-29.89762567
HUB_R2	1.919803399	1.919803399	1.919803399
HUB_Z3	-21.72734893	-21.72734893	-21.72734893
HUB_R3	4.433385637	4.433385637	4.433385637
HUB_Z4	-16.15613725	-16.15613725	-16.15613725
HUB_R4	6.350668236	6.350668236	6.350668236
HUB_Z5	-8.676336109	-8.676336109	-8.676336109
HUB_R5	7.99060918	7.99060918	7.99060918
HUB_Z6	0.708473804	0.708473804	0.708473804
HUB_R6	8.491735897	8.491735897	8.491735897
HUB_Z7	1.353867681	1.353867681	1.353867681
HUB_R7	8.508592961	8.508592961	8.508592961
HUB_Z8	1.728019998	1.728019998	1.728019998
HUB_R8	8.566316274	8.566316274	8.566316274
HUB_Z9	2.858674769	2.858674769	2.858674769
HUB_R9	8.828498462	8.828498462	8.828498462
HUB_Z10	3.314905874	3.314905874	3.314905874
HUB_R10	8.95142727	8.95142727	8.95142727
HUB_Z11	3.623085554	3.623085554	3.623085554
HUB_R11	9.072114347	9.072114347	9.072114347
HUB_Z12	4.036731663	4.036731663	4.036731663
HUB_R12	9.297220147	9.297220147	9.297220147
HUB_Z13	6.971483703	6.971483703	6.971483703
HUB_R13	11.31401555	11.31401555	11.31401555
HUB_Z14	12.10979739	12.10979739	12.10979739
HUB_R14	15.39302412	15.39302412	15.39302412

HUB_Z15	18.10856686	18.10856686	18.10856686
HUB_R15	21.44260901	21.44260901	21.44260901
HUB_Z16	20.58317571	20.58317571	20.58317571
HUB_R16	24.4096181	24.4096181	24.4096181
HUB_Z17	22.89091962	22.89091962	22.89091962
HUB_R17	27.50728051	27.50728051	27.50728051
HUB_Z18	25.04106307	25.04106307	25.04106307
HUB_R18	30.71591978	30.71591978	30.71591978
HUB_Z19	27.01832171	27.01832171	27.01832171
HUB_R19	34.03369381	34.03369381	34.03369381
HUB_Z20	28.8403912	28.8403912	28.8403912
HUB_R20	37.44066712	37.44066712	37.44066712
HUB_Z21	30.48201211	30.48201211	30.48201211
HUB_R21	40.9363031	40.9363031	40.9363031
HUB_Z22	32.0003618	32.0003618	32.0003618
HUB_R22	44.48954923	44.48954923	44.48954923
HUB_Z23	33.34539822	33.34539822	33.34539822
HUB_R23	48.11054289	48.11054289	48.11054289
HUB_Z24	34.53665624	34.53665624	34.53665624
HUB_R24	51.78397515	51.78397515	51.78397515
SHROUD_Z1	-39.20199762	-39.20199762	-39.20199762
SHROUD_R1	43.432	43.432	43.432
SHROUD_Z2	10.53401041	10.53401041	10.53401041
SHROUD_R2	43.37312296	43.37312296	43.37312296
SHROUD_Z3	17.34270618	17.34270618	17.34270618
SHROUD_R3	43.66214879	43.66214879	43.66214879
SHROUD_Z4	19.37112054	19.37112054	19.37112054
SHROUD_R4	44.01258974	44.01258974	44.01258974
SHROUD_Z5	21.27193489	21.27193489	21.27193489
SHROUD_R5	44.68050147	44.68050147	44.68050147
SHROUD_Z6	22.63190678	22.63190678	22.63190678
SHROUD_R6	45.40878659	45.40878659	45.40878659
SHROUD_Z7	23.76793335	23.76793335	23.76793335
SHROUD_R7	46.27925719	46.27925719	46.27925719
SHROUD_Z8	24.59205798	24.59205798	24.59205798
SHROUD_R8	47.07824465	47.07824465	47.07824465
SHROUD_Z9	25.64874602	25.64874602	25.64874602
SHROUD_R9	48.43374389	48.43374389	48.43374389
SHROUD_Z10	26.70305709	26.70305709	26.70305709
SHROUD_R10	50.164955	50.164955	50.164955

Table F.1: Frozen parameter impeller passage

Table F.2: Frozen parameter list

Name	Lower bound	Value	Upper bound
HUB_Z25	35.64637612	35.64637612	35.64637612
HUB_R25	55.48504536	55.48504536	55.48504536
HUB_R27	82.99846674	82.99846674	82.99846674
HUB_Z28	67.99972297	67.99972297	67.99972297
HUB_R28	82.99926789	82.99926789	82.99926789
HUB_Z29	88	88	88
HUB_R29	83	83	83
HUB_Z30	108	108	108
HUB_R30	83.99955858	83.99955858	83.99955858
SHROUD_Z11	28.70838737	28.70838737	28.70838737
SHROUD_R11	55.49926376	55.49926376	55.49926376
SHROUD_R13	89.17863042	89.17863042	89.17863042
SHROUD_Z14	67.99814478	67.99814478	67.99814478
SHROUD_R14	88.9980009	88.9980009	88.9980009
SHROUD_Z15	88	88	88
SHROUD_R15	89	89	89
SHROUD_Z16	107.9981266	107.9981266	107.9981266
SHROUD_R16	88.00025656	88.00025656	88.00025656
S1_SPAN	-0.015	-0.015	-0.015
S2_SPAN	1.015	1.015	1.015
S1_LE_RADIUS	0.267808866	0.267808866	0.267808866
S1_HALF_THICKNESS_P1	0.971579043	0.971579043	0.971579043
S1_HALF_THICKNESS_P2	0.83363529	0.83363529	0.83363529
S1_HALF_THICKNESS_P3	1.407025825	1.407025825	1.407025825
S1_HALF_THICKNESS_P4	0.950121595	0.950121595	0.950121595
S2_LE_RADIUS	0.27454755	0.27454755	0.27454755
S2_HALF_THICKNESS_P1	0.978241186	0.978241186	0.978241186
S2_HALF_THICKNESS_P2	0.926302954	0.926302954	0.926302954
S2_HALF_THICKNESS_P3	1.281688255	1.281688255	1.281688255
S2_HALF_THICKNESS_P4	0.996241876	0.996241876	0.996241876
R_TE_HUB	82.99926795	82.99926795	82.99926795
R_TE_SHROUD	88.99800109	88.99800109	88.99800109
S1_MERID_LENGTH	0.464511913	0.464511913	0.464511913
S2_MERID_LENGTH	0.531727256	0.531727256	0.531727256
LEAN_BETA	0.046416647	0.046416647	0.046416647
NB	20	20	20
BLADE_ROTATION	-90	-90	-90

Appendix G

Possible database geometries

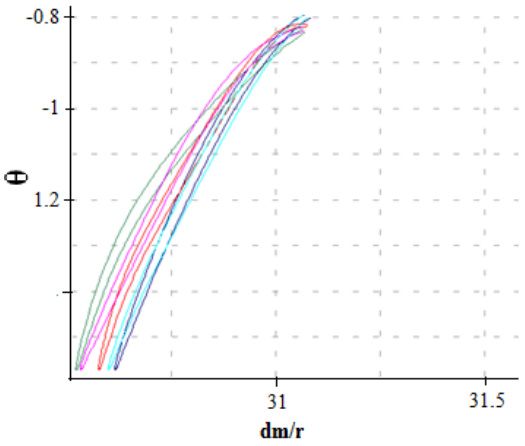

Figure G.1: Sample possible blade geometries

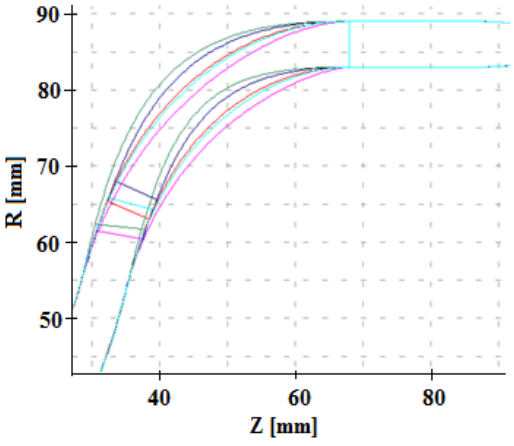

Figure G.2: Sample possible meridional geometries

Appendix H

Performance maps

H.1 Vaneless mean line performance

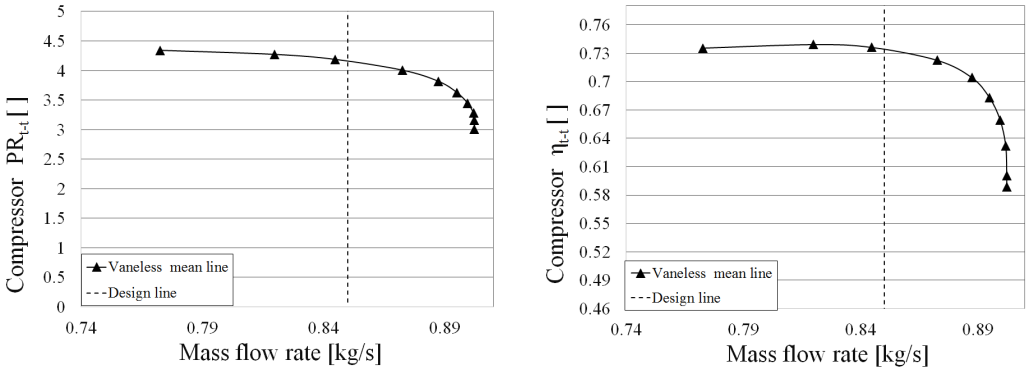

(a) (b)

Figure H.1: a) Compressor total-to-total pressure ratio b) Compressor total-to-total isentropic efficiency

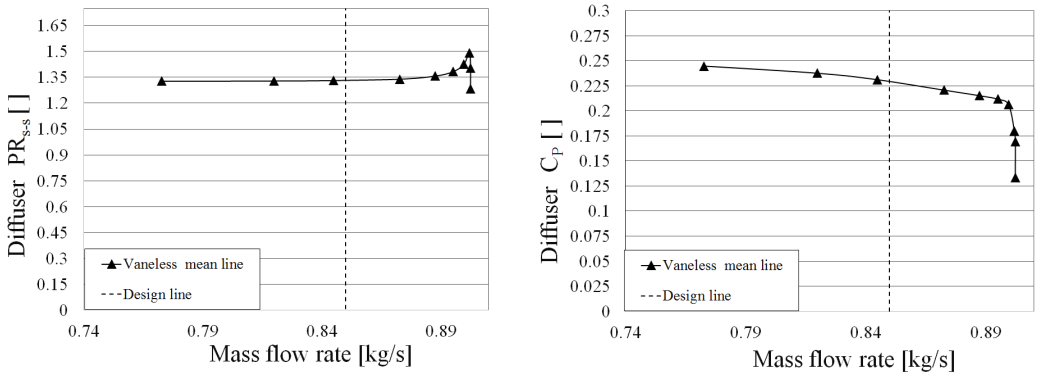

(a) (b)

Figure H.2: a) Diffuser static-to-static pressure ratio b) Diffuser static pressure recovery coefficient

H.2 Optimised design first leading edge

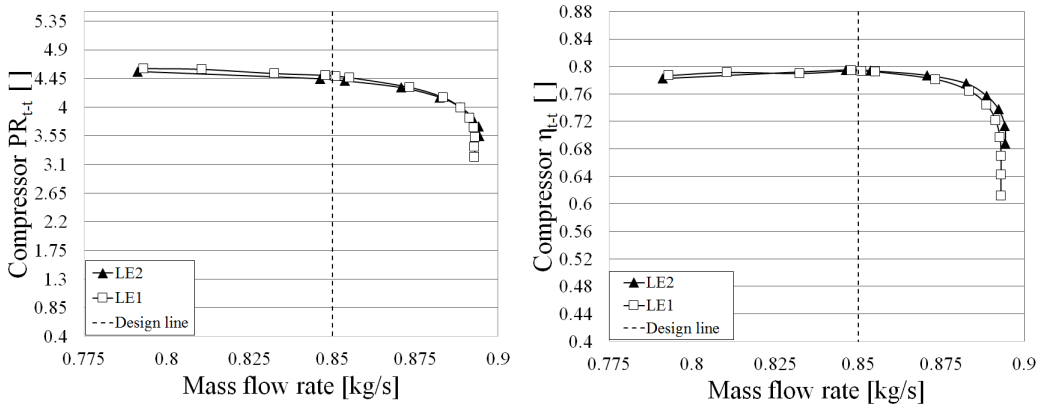

(a) (b)

Figure H.3: a) Compressor total-to-total pressure ratio b) Compressor total-to-total isentropic efficiency

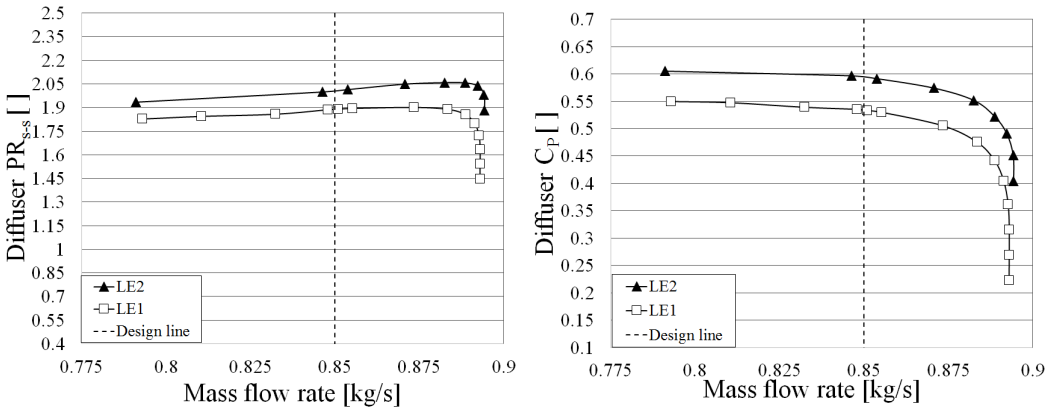

(a) (b)

Figure H.4: a) Diffuser static-to-static pressure ratio b) Diffuser static pressure recovery coefficient

Appendix I

Final compressor performance map

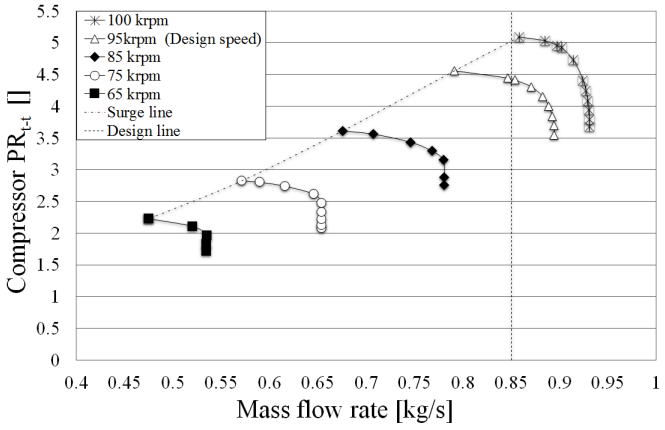

Figure I.1: Compressor map total-to-total pressure ratio

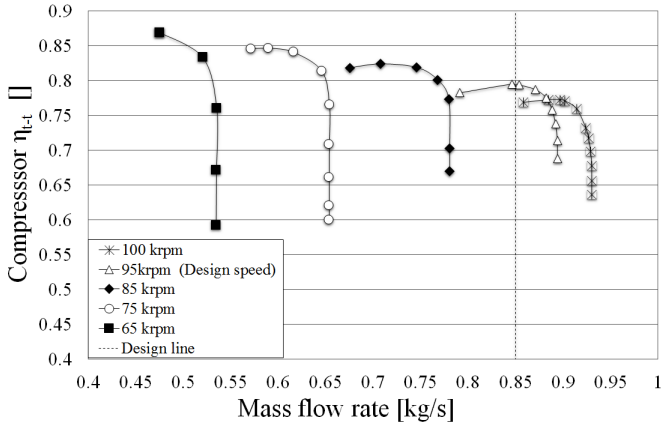

Figure I.2: Compressor map total-total isentropic efficiency

Appendix J

Vaneless diffuser with de-swirler vanes geometry

The de-swirler vanes were developed using the Autoblade™ and Design3D™ database generator. The optimised design was modified in Autoblade™ by increasing the vaneless gap, thus decreasing the vane length with the same meridional passage as the optimised diffuser design. The number of vanes were kept at 20 vanes. The passage was then place in the database generator and the vaneless gap was allowed to vary, the camberline was also allowed to vary. However, the database was run for only the mean line diffuser design point numerical settings. The author evaluated the database and selected the best design, with the best total-to-total isentropic efficiency and total-to-total pressure ratio and with a acceptable discharge flow angle.

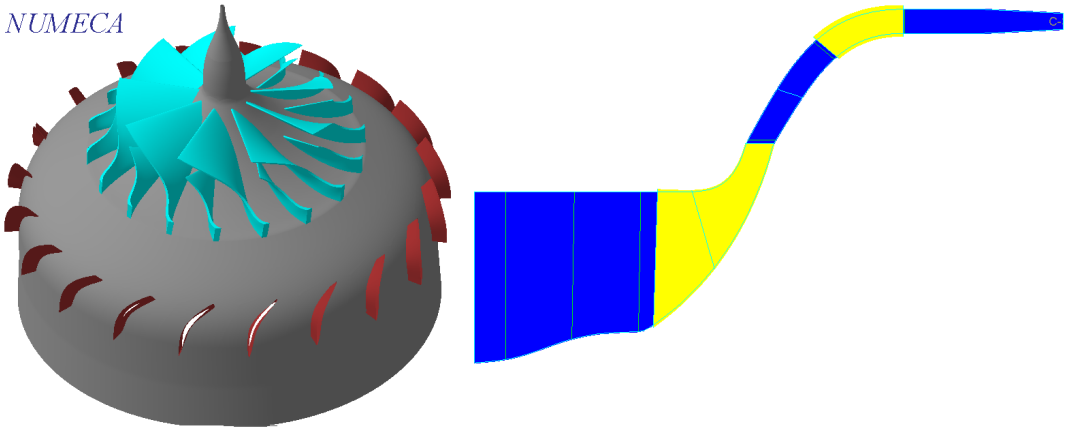

Figure J.1: Compressor with de-swirler geometry

Appendix K

Manufactured parts

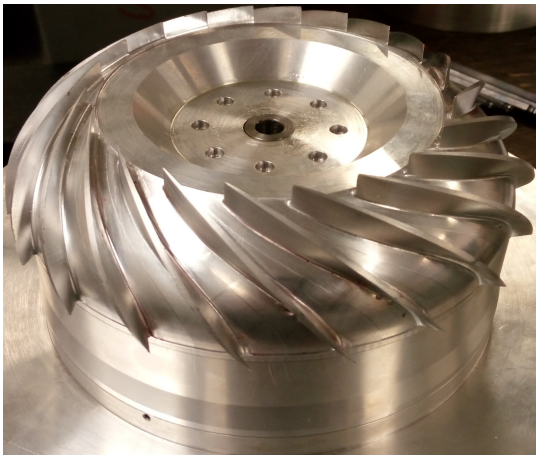

Figure K.1: Diffuser test model

Figure K.2: Diffuser test rig

List of References

Arant, J. (1976). Centrifugal compressor auxilliary instrumentation. In: *Centrifugal compressor operation and control*, pp. 1–11. ISA.

Ashjaee, J. and Johnston, J. (1979). Transitory stall in diffusers. In: *Symposium on Flow in Primary, Non rotating Passages in Turbomachines. ASME.*

Aungier, R. (1988). A systematic procedure for the aerodynamic design of vaned diffusers. *Flows in Non-Rotating Turbomachinery Components, ASME FED*, vol. 69, pp. 27–34.

Aungier, R.H. (2000). *Centrifugal compressors: a strategy for aerodynamic design and analysis*. American Society of Mechanical Engineers.

Basson, C. (2016). *An Investigation of the Effect of Inlet Swirl on the Flow through a Micro-Gas Turbine Combustion Chamber*. Master's thesis, Stellenbosch University.

Beér, J.M. and Chigier, N.A. (1972). Combustion aerodynamics. *New York*.

Burger, C. (2016). Design procedure of a compact aerodynamic crossover diffuser for micro gas turbine application. *University of Stellenbosch*.

Casey, M. and Rusch, D. (2014). The matching of a vaned diffuser with a radial compressor impeller and its effect on the stage performance. *Journal of Turbomachinery*, vol. 136, no. 12, p. 121004.

Cevik, M. (2009). *Design and Optimization of a Mixed Flow Compressor Impeller using Robust Design Methods*. Ph.D. thesis, Citeseer.

Dallenbach, F. and Van Le, N. (1960). Supersonic diffuser for radial and mixed flow compressors. *Journal of Basic Engineering*.

de Villiers, L.C.B. (2014). *Design of a Centrifugal Compressor for Application in Micro Gas Turbines*. Master's thesis, Stellenbosch University.

de Wet, A.L. (2012). Performance investigation of a turbocharger compressor.

Deniz, S., Greitzer, E.M. and Cumpsty, N.A. (2000). Effects of inlet flow field conditions on the performance of centrifugal compressor diffusers: part 2-straight-channel diffuser. *Journal of Turbomachinery*, vol. 122, no. 1, pp. 11–21.

Diener, O.H.F. (2016). Development of a mixed-flow compressor impeller for micro gas turbine application.

Dixon, S. (1978). *Fluid mechanics, thermodynamics of turbomachinery. in si/metric units.* Pergamon Press.

Eckardt, D.t. (1975). Instantaneous measurements in the jet-wake discharge flow of a centrifugal compressor impeller. *Journal of Engineering for Power*, vol. 97, no. 3, pp. 337–345.

Ferguson, T. (1963). *The Centrifugal Compressor Stage.* Butterworths &CO.

Filipenco, V.G., Deniz, S., Johnston, J.M., Greitzer, E.M. and Cumpsty, N.A. (1998). Effects of inlet flow field conditions on the performance of centrifugal compressor diffusers: Part 1-discrete-passage diffuser. In: *ASME 1998 International Gas Turbine and Aeroengine Congress and Exhibition*, pp. V001T01A111–V001T01A111. American Society of Mechanical Engineers.

Gaetani, P., Persico, G., Mora, A., Dossena, V. and Osnaghi, C. (2012). Impeller-vaned diffuser interaction in a centrifugal compressor at off design conditions. *Journal of Turbomachinery*, vol. 134, no. 6, p. 061034.

Goldstein, A.W. (1948). Design and performance of experimental axial-discharge mixed flow compressors impeller design theory. *National Advisory for Aeronautics.*

Japikse, D. (1996). *Centrifugal compressor design and performance.* Concepts Eti.

Japikse, D. and Baines, N. (1997). *Introduction to turbomachinery.* Concepts Eti.

Japikse, D. and Baines, N.C. (1998). *Turbomachinery diffuser design technology.* Concepts Eti.

Jie, C. and Guoping, H. (2010). Redesign of an 11 cm-diameter micro diffuser. *Chinese Journal of aeronautics*, vol. 23, no. 3, pp. 298–305.

Kano, F., Fukao, Y. and Shirakami, T. (1984). Development of high specific speed mixed flow compressors. In: *Proceedings of the Thirteenth Turbomachinery Symposium, Texas Agricultural and Mechanical University, Texas, USA*, pp. 139–147.

Kirtley, K. and Beach, T. (1992). Deterministic blade row interactions in a centrifugal compressor stage. *Journal of turbomachinery*, vol. 114, no. 2, pp. 304–311.

Krain, H. (1981). A study on centrifugal impeller and diffuser flow. *Journal of Engineering for Power*, vol. 103, no. 4, pp. 688–697.

Krige, D. (2012). *Performance evaluation of a micro gas turbine centrifugal compressor diffuser.* Master's thesis, University of Stellenbosch.

Lefebvre, A.H. (1983). *Gas turbine combustion.* Hemisphere publishing corporation, Washington.

Ling, J., Wong, K. and Armfield, S. (2007). Numerical investigation of a small gas turbine compressor. In: *16th Australasian Fluid Mechanics Conference (AFMC)*, pp. 961–966. School of Engineering, The University of Queensland.

Martinjako, J. (2014). *Low Cost Gas Turbine Off-Design Prediction Technique*. Master's thesis, Arizona State University.

Menter, F.R. (1992). Performance of popular turbulence model for attached and separated adverse pressure gradient flows. *AIAA journal*, vol. 30, no. 8, pp. 2066–2072.

NUMECA International (2014a). *Autogrid5 ™ v10.1 User Manual*. NUMECA International.

NUMECA International (2014b). *Numeca Fine/Turbo™ v10.1 User Manual*.

NUMECA International (2014c). *FINE ™/Design3D v10.1 User Manual*. NUMECA International.

Orth, U., Ebbing, H., Krain, H., Weber, A. and Hoffmann, B. (2001). Improved compressor exit diffuser for an industrial gas turbine. In: *ASME Turbo Expo 2001: Power for Land, Sea, and Air*, pp. V001T03A025–V001T03A025. American Society of Mechanical Engineers.

Reneau, L.R., Johnston, J. and Kline, S.J. (1967). Performance and design of straight, two-dimensional diffusers. *Journal of Basic Engineering*, vol. 89, no. 1, pp. 141–150.

Runstadler, P.W. (1969). Pressure recovery performance of straight-channel, single-plane divergence diffusers at high mach numbers. rep. n-88, creare. *Inc.(USAAVLABS-TR-69-56, AD-865300)*.

Saravanamuttoo, H.I.H., Rogers, G.F.C. and Cohen, H. (2001). *Gas turbine theory*. Pearson Education.

Sayers, A.T. (1990). *Hydraulic and compressible flow turbomachines*. McGraw-Hill.

Shum, Y.K.P., Tan, C. and Cumpsty, N. (2000). Impeller-diffuser interaction in centrifugal compressor. In: *ASME Turbo Expo 2000: Power for Land, Sea, and Air*, pp. V001T03A004–V001T03A004. American Society of Mechanical Engineers.

van der Merwe, B.B. (2012). Design of a centrifugal compressor impeller for micro gas turbine application. *MSc Engineering Thesis, Stellenbosch University*.

Versteeg, H.K. and Malalasekera, W. (2007). *An introduction to computational fluid dynamics: the finite volume method*. Pearson Education.

Wilkosz, B., Schmidt, J., Guenther, C., Schwarz, P., Jeschke, P. and Smythe, C. (2014). Numerical and experimental comparison of a tandem and single vane deswirler used in an aero engine centrifugal compressor. *Journal of Turbomachinery*, vol. 136, no. 4, p. 041005.

Ziegler, K.U., Gallus, H.E. and Niehuis, R. (2002). A study on impeller-diffuser interaction: part i-influence on the performance. In: *ASME Turbo Expo 2002: Power for Land, Sea, and Air*, pp. 545–556. American Society of Mechanical Engineers.